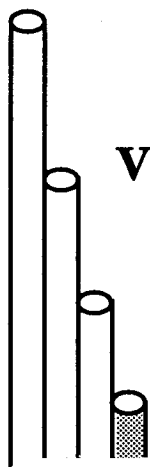NASA-CR-199792

NAG1-343

CCMS-95-10
VPI E-95-04

6462

# CENTER FOR COMPOSITE MATERIALS AND STRUCTURES

## Verification of a Three-Dimensional Resin Transfer Molding Process Simulation Model
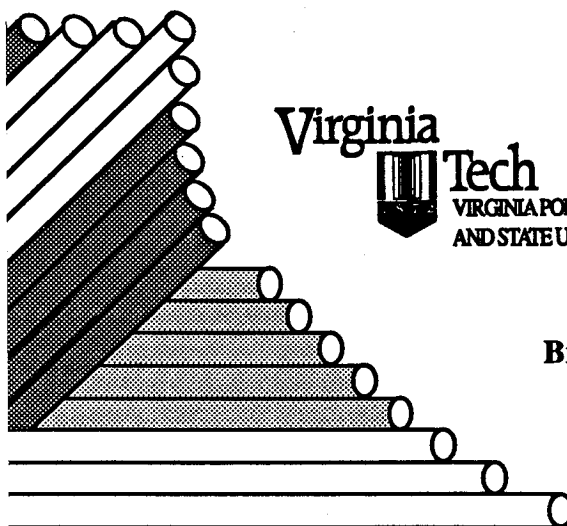
John C. Fingerson
Alfred C. Loos
H. Benson Dexter

Virginia Tech
VIRGINIA POLYTECHNIC INSTITUTE
AND STATE UNIVERSITY

BLACKSBURG , VIRGINIA
24061

September 1995

College of Engineering
Virginia Polytechnic Institute and State University
Blacksburg, Virginia 24061

September 1995

CCMS-95-10
VPI-E-95-04

# Verification of a Three-Dimensional Resin Transfer Molding Process Simulation Model

John C. Fingerson[1]
Alfred C. Loos[2]
H. Benson Dexter[3]

Department of Engineering Science and Mechanics

Interim Report 101

The NASA-Virginia Tech Composites Program

Prepared for:     Mechanics of Materials Branch
                  National Aeronautics and Space Administration
                  Langley Research Center
                  Hampton, VA  23681-0001

---

[1]Graduate Research Assistant, Department of Engineering Science and Mechanics, Virginia Polytechnic Institute and State University
[2]Professor, Department of Engineering Science and Mechanics, Virginia Polytechnic Institute and State University
[3]Sr. Materials Research Engineer, Mechanics of Materials Branch, NASA Langley Research Center, Hampton, VA

# VERIFICATION OF A THREE-DIMENSIONAL RESIN TRANSFER MOLDING PROCESS SIMULATION MODEL

## ABSTRACT

Experimental evidence was obtained to complete the verification of the parameters needed for input to a three-dimensional finite element model simulating the resin flow and cure through an orthotropic fabric preform. The material characterizations completed include resin kinetics and viscosity models, as well as preform permeability and compaction models.

The steady-state and advancing front permeability measurement methods are compared. The results indicate that both methods yield similar permeabilities for a plain weave, bi-axial fiberglass fabric. Also, a method to determine principal directions and permeabilities is discussed and results are shown for a multi-axial warp knit preform.

The flow of resin through a blade-stiffened preform was modeled and experiments were completed to verify the results. The predicted inlet pressure was approximately 65% of the measured value. A parametric study was performed to explain differences in measured and predicted flow front advancement and inlet pressures.

Furthermore, PR-500 epoxy resin/IM7 8HS carbon fabric flat panels were fabricated by the Resin Transfer Molding process. Tests were completed utilizing both perimeter injection and center-port injection as resin inlet boundary conditions. The mold was instrumented with FDEMS sensors, pressure transducers, and thermocouples to monitor the process conditions. Results include a comparison of predicted and measured inlet

pressures and flow front position. For the perimeter injection case, the measured inlet pressure and flow front results compared well to the predicted results. The results of the center-port injection case showed that the predicted inlet pressure was approximately 50% of the measured inlet pressure. Also, measured flow front position data did not agree well with the predicted results. Possible reasons for error include fiber deformation at the resin inlet and a lag in FDEMS sensor wet-out due to low mold pressures.

# ACKNOWLEDGEMENTS

# TABLE OF CONTENTS

# CHAPTER 3

# CHAPTER 4

# CHAPTER 5

# CHAPTER 6

# LIST OF FIGURES

# LIST OF TABLES

# 1. Introduction

Fabrication of composite materials by processes such as Resin Transfer Molding (RTM), Structural Reaction Injection Molding (SRIM), and Resin Film Infusion (RFI) involve the infiltration of fiberglass or carbon fiber preforms with resins such as epoxies, vinylesters, and polyesters. Resin Transfer Molding is the process of injecting a dry fiber preform in a closed mold with resin and is typically done at low molding pressures. Normally, a vacuum is used to remove entrapped air from the mold. Some of the advantages of RTM include elimination of prepreg manufacture and improved dimensional control of the finished product.

In comparison to the unidirectional prepreg tape layup manufacturing technique, RTM offers the advantages of integration of structural components such as foam cores, and the ability to manufacture more complex shapes.

Recently, the development of automated textile technologies have allowed for three-dimensional preforms to be manufactured from both woven and stitched materials. The ability to produce a near-net preform reduces the mold layup time and can increase the product quality by reducing the variability in fiber orientation. Through-the-thickness reinforcements may be added to increase the damage tolerance of the finished part by strengthening the part in the transverse direction.

An application of RTM is aircraft structures [1]. Typically, it has been used to fabricate secondary structures, not flight critical structures such as the wing box or fuselage beam. Design and manufacturing process optimization are necessary in order for manufacture of flight critical components to become cost effective.

Modeling of the RTM process can be a critical step in the optimization of both tooling design and processing cycle. One of the major considerations in tooling design is the location of injection ports. The characteristics of the resin flow are defined by the following material properties - the preform permeability tensor, preform compaction behavior, and the viscosity of the resin. Past research has been completed to verify flow

1

characteristics in two dimensions [1]. However, with the advent of more complicated three-dimensional woven and stitched preforms, the ability to verify the three-dimensional material properties is essential.

A Finite Element/Control Volume technique was developed at Virginia Tech [1] and has been utilized to calculate flow front locations and mold pressures for a blade-stiffened carbon fiber preform. The major objective of this investigation was to verify the three-dimensional model by measurement of the flow front locations and resin inlet pressure during mold filling of a single blade-stiffened panel. In addition, a complete system has been designed for accurate automated real-time measurement of fabric permeability.

A three-dimensional mesh of the preform was created utilizing PATRAN software. The measured permeability values for the components of the blade-stiffened preform are applied to their corresponding elements. Also, the boundary conditions which include the injection port location and inlet flow rate were applied. Visualization of results was completed using PATRAN as a post-processor.

Finally, RTM fabrication of flat rectangular panels with a high temperature reactive resin system was completed. A predetermined cure cycle was applied and the resin injection rate was held constant. Finite Element/Control Volume simulation results including pressure distribution and flow front locations were compared to the in-situ measurements obtained from FDEMS sensors, pressure transducers, and thermocouples.

# 2. Permeability and Compaction: Measurement of Material Properties

## 2.1 Introduction

A permeability measurement system to determine permeability as a function of fiber volume fraction of high fiber volume fraction textile preforms has been developed. A method of determining the in-plane principal axes and principal permeabilities as a function of fiber volume fraction is presented. The permeability and compaction behavior of the materials used to fabricate a blade-stiffened preform are characterized.

## 2.2 Literature Review

### 2.2.1 Permeability

Permeability is defined as the resistance to flow through porous media. The complex geometries of most textile preforms for structural composites have made it difficult to accurately predict the permeability by analytical methods. The effects that must be accounted for in the permeability predictions include through-the-thickness stitching, interply interfaces, capillary and wetting characteristics of the fiber and resin.

Darcy's law [2], an empirical model for flow through porous media, is written as follows:

$$q = \frac{S\Delta P}{\eta L} \qquad (2\text{-}1)$$

It relates the superficial or filter velocity ($q$) to the pressure difference developed ($\Delta P$) across the length ($L$) of the fabric, the viscosity ($\eta$) of the fluid, and an experimentally derived permeability constant ($S$). For Darcy's Law to be valid, the following must hold:

- process is quasi-static and the material system behaves as a continuum

- fluid is Newtonian
- viscous forces dominate over inertial forces, and flow is in the laminar regime

Darcy's Law replaces the momentum equation as a relationship between the velocity vector and the stress gradient vector. If the material is considered anisotropic the relation between the superficial velocities and the pressure gradients is written as follows:

$$\begin{bmatrix} \overline{q}_x \\ \overline{q}_y \\ \overline{q}_z \end{bmatrix} = \frac{1}{\eta} \begin{bmatrix} S_{xx} & S_{xy} & S_{xz} \\ S_{xy} & S_{yy} & S_{yz} \\ S_{xz} & S_{yz} & S_{zz} \end{bmatrix} \begin{bmatrix} \partial P / \partial x \\ \partial P / \partial y \\ \partial P / \partial z \end{bmatrix} \tag{2-2}$$

where $\overline{\overline{S}}$ is the symmetric permeability tensor. If the transverse axis (z) is considered parallel to the principal transverse axis, the off-axis components $S_{xz}$ and $S_{yz}$ are zero. For preforms composed of fibers lying primarily in the x-y plane, the off-axis components $S_{xz}$ and $S_{yz}$ are zero.

A homogeneous preform is defined [3] as a multi-layer assembly that consists of two or more layers of the same fabric oriented in the same direction. A heterogeneous preform consists of plies which differ in directional permeabilities, degree of anisotropy, and/or orientation.

The in-plane permeability of a heterogeneous preform is affected by the transverse permeability of the individual layers. Adams [3] conducted experiments and noted that much of the liquid flow in a heterogeneous preform takes place in the high permeability layers and that transverse flow is responsible for wetting out the low permeability layers.

The permeability is often related to the porosity ($\phi$) of the preform, defined as the ratio of total volume of open pores to the total volume of the fabric preform. The porosity is also known as the resin volume fraction of the composite. The relationship between fiber volume fraction ($v_f$) and porosity is:

$$\phi = 1 - v_f \tag{2-3}$$

## 2.2.2 Analytic Methods to Determine Permeability

The Kozeny-Carmen relationship [4] is an attempt to derive the Darcy permeability constant analytically and is expressed as:

$$S = \frac{r^2}{\left[9K_0K_1^2\right]}\frac{\left[1-v_f\right]^3}{\left[v_f^2\right]} \tag{2-4}$$

where $v_f$ is the fiber volume fraction, $r$ is the fiber radius, and $K_0K_1^2$ is the Kozeny-Carmen constant. $K_0$ is a geometric shape factor of the fiber, and $K_1$ is the tortuosity of the fabric, defined as the additional length that the fluid must travel in a capillary to traverse across the porous media. Because of the difficulty in determining these constants analytically, $K_0$ and $K_1$ are lumped together and determined experimentally.

Analytical models have been derived to calculate permeability of some simple fiber architectures. Gebart [5] calculated permeabilities for idealized unidirectional reinforcements. Berdichevsky and Cai [6] used the self-consistent method to calculate permeability for an aligned fiber bundle in both the transverse and longitudinal direction and concluded that flow within the fiber tows makes a limited contribution to the overall permeability since the flow around the tows is the main flow path.

Analytical models have been derived for heterogeneous unidirectional fiber beds. The permeability of the fiber bed can be divided into two separate models - a model to determine the permeability of the region around the fiber tows, and a model to determine the permeability within the fiber tows. Sadiq et al. [4] found that predictions based on homogeneous beds composed of cylinders with a radius equal to the fiber radius underpredicted the permeability of the heterogeneous media by as much as three orders of magnitude. It was proposed to predict the permeability of the heterogeneous media as follows:

$$S = S_{Nvf} \frac{V_{f\max}}{T_{vf}} \qquad\qquad (2\text{-}5)$$

where $V_{f\max}$ is the maximum possible fiber volume fraction, and $T_{vf}$ is the tow fiber volume fraction. $S_{Nvf}$ is the permeability predicted from an asymptotic model which assumes that the fibers are solid. An asymptotic matching function is used to match the solutions from a lubrication approximation valid at high volume fractions and a unit cell model valid at low volume fractions.

Parnas and Phelan [7] considered the effects of two types of heterogeneities on the fluid flow. These include both boundary inhomogeneities between the preform and mold wall and heterogeneities existing in the structure of the preform itself. The heterogeneities in the structure of the preform exist due to the localized impregnation of individual fiber bundles. The effect was modeled by considering each fiber bundle as a flow sink removing fluid from the advancing flow front and assigning a different permeability to the fiber bundle as compared to the permeability of the preform. The boundary inhomogeneities were considered by simultaneously applying the Brinkman equation [7]:

$$\frac{\partial P}{\partial x} - \eta \frac{\partial^2 u}{\partial y^2} + \frac{\eta u}{S} = 0 \qquad\qquad (2\text{-}6)$$

where $u$ is the velocity in the x-direction. The Brinkman equation accounts for the no-slip boundary condition at the mold wall by including the shear stress term and the Navier-Stokes equation to describe flow in an open channel between the mold wall and the edge of the preform. Parnas and Phelan [7] proposed the following equations to predict the effects of channeling or resin flow around the edge of the preform:

6

$$\frac{F}{F_0} = 1 + \frac{\Delta^3}{12YS} \qquad (2\text{-}7)$$

$$\frac{v_m}{v_d} = \frac{\left(\Delta^2/S\right)-1}{8} + \frac{\left(\Delta/\sqrt{S}\right)-1}{4} \qquad (2\text{-}8)$$

$F$ : flow rate with channeling

$F_0$ : flow rate withough channeling

$v_m$ : maximum velocity in the open channel

$v_d$ : Darcy velocity

$\Delta$ : width of open channel

$Y$ : distance from center to edge of mold cavity

$S$ : preform permeability

It was noted that $\dfrac{v_m}{v_d} >> \dfrac{F}{F_0}$ for similar permeabilities and channel widths. Therefore, the results indicate that changes in the velocity profile caused by channeling may be much greater than the effects of the channeling on the total flow rate through the mold.

## 2.2.3 Factors Which Influence Permeability

Factors noted to possibly influence permeability are as follows [8] :

- degree of preform saturation
- wetting characteristics of preform
- capillary pressure

The degree of saturation has been stated to influence permeability by decreasing the effective permeability as saturation increases [8]. Capillary pressure, which occurs at the

fluid/air interface, acts to increase the pressure gradient forcing the fluid through the medium. The pressure term when including capillary pressure is denoted as

$$\Delta P + \frac{\sigma \cos \theta}{m} \qquad (2\text{-}9)$$

where $\sigma$ is the surface energy of the liquid, $\theta$ is the wetting angle, and $m$ is the mean hydraulic radius. The wetting characteristics of the preform are characterized by the surface tension between the liquid and the fiber. A high surface tension can also increase the likelihood of voids.

## 2.2.4 Experimental Trends in Permeability

Adams and Rebenfield [3] studied effects of multiple layers on in-plane permeability. It was found that fabrics with minimal surface undulations showed no dependence on the number of layers since the pore sizes between plies and those within the plies are similar in size. Woven fabrics with surface undulations showed an increase in permeability with an increase in the number of layers. The magnitude of the increase decreased fractionally as the ratio of plies and interply regions approached unity. This was attributed to the large interlaminar pores created by the surface undulations.

A comparison of the permeabilities of E-glass plain weave and IM7 eight-harness satin weave was made by Hammond [8]. The E-glass permeability was an order of magnitude higher than that of the weave. It was suggested that the more complex weave pattern of IM7 created a more convoluted flow path resulting in the lower permeability.

Kim et al. [9] also studied the effects of multiple layers on in-plane permeability. They proposed the permeability of a multi-layer preform ($S_{avg}$) could be calculated from the permeability of individual layers as follows:

$$S_{avg} = \frac{\sum_{i=1}^{n} s_i A_i}{\sum_{i=1}^{n} A_i} \qquad (2\text{-}10)$$

where $A_i$ is the cross-sectional flow area and $s_i$ is the permeability of the individual layer. The assumption is made that there is no transverse flow between layers. Experimental results show that permeability of combined layers is strongly dependent on the permeability of individual layers.

Weideman [10] characterized unstitched, lightly stitched, and knitted/stitched fabrics in the transverse direction to determine the effects of stitching. It was found that the degree of stitching directly influenced the permeability. As the stitch density increased, the transverse permeability increased. Also, the knitted/stitched fabrics had a higher permeability than the lightly stitched fabrics. Hammond [8] also noted that stitching caused approximately a 5-fold increase in transverse permeability.

Hammond [8] also experimentally verified that the fluid type used for testing is not critical to the permeability results.

Chan, Larive, and Morgan [11] noted a small increase in measured permeability as the flow rate was increased.

## 2.2.5 Permeability Measurement Techniques

Five permeability fixture types are currently being employed to measure permeability of textile reinforcements. These are listed below with the permeability direction noted in parentheses.

1. Advancing front, radial visualization fixture, constant mold height (planar) [12]
2. Advancing front, one-dimensional fixture, constant mold height (planar) [13]
3. Steady-state, one-dimensional fixture, constant mold height (planar/transverse) [8,12,14]
4. Steady-state, one-dimensional fixture, adjustable mold height (planar/transverse) [8,10]

5. Fiber optic flow front measurement (planar/transverse) [15]

These fixture types are capable of measuring permeability using either constant pressure or constant flow rate inlet conditions.

The radial technique has an advantage over one-dimensional permeability measurements of no boundary heterogeneities, or edge flow effects. Edge flow effects can be caused by a dissimilarity in the width of the fabric when compared to the fixture and deformation of the fibers at the edge of the preform caused by cutting the fabric. Wang, Wu, and Lee [12] proposed a method of determining edge permeability by using two Type 3 fixtures of different widths and assuming that the width of the fabric where the edge effect takes place ($w_e$) is known. The method assumes one-dimensional flow and that the edge flow is still governed by Darcy's law. The set of equations for determining the fabric permeability ($S_c$) and the edge permeability ($S_e$) are as follows:

$$\frac{Q_1 \eta L}{h P_1} = w_1 S_1 = 2 w_e \left( S_e - S_c \right) + w_1 S_c \qquad (2\text{-}11)$$

$$\frac{Q_2 \eta L}{h P_2} = w_2 S_2 = 2 w_e \left( S_e - S_c \right) + w_2 S_c \qquad (2\text{-}12)$$

where $w_1$ and $w_2$ are the widths of the separate fixtures, $Q_1$ and $Q_2$ are the inlet flow rates, $S_1$ and $S_2$ are the calculated average permeabilities, $P_1$ and $P_2$ are the respective inlet pressures, and $h$ is the mold height.

A method of determining in-plane permeabilities using Fixture Type 1 was also developed by Wang, Wu, and Lee [12]. Initially, an advancing front radial visualization test is completed to determine principal axes. The principal axes are located along the major and minor elliptic axes of the flow front. The ratio of the permeabilities along the principal axes is determined by

$$\frac{\text{length of minor elliptic axis}}{\text{length of major elliptic axis}} = \left(\frac{S_y}{S_x}\right)^{\frac{1}{2}} \tag{2-13}$$

where $S_x$ and $S_y$ are the permeabilities along the principal directions. It was proposed that the magnitude of the permeabilities could also be determined from the advancing front radial test by simultaneously measuring the radius ($R$) of the major axis, flow rate ($Q$), and inlet pressure ($P$) and solving the following set of equations [12]:

$$\left(S_x S_y\right)^{\frac{1}{2}} = \frac{Q}{P}\frac{\eta}{h}\frac{\ln\left(R/R_{inlet}\right)+\ln(f)}{2\pi} \tag{2-14}$$

$$f = \left[\frac{1}{\left(\frac{S_x}{S_y}\right)^{\frac{1}{2}}+1}\right] \times \left[1+\left[1+\frac{R_{inlet}^2}{R^2}\left(\frac{S_x}{S_y}-1\right)\right]\right]^{\frac{3}{2}} \tag{2-15}$$

where $R_{inlet}$ is the radius of the resin inlet. This method has the disadvantages of only being able to measure permeability at a single fiber volume fraction and continuously determining the flow front position. The advantages are that the principal axes and permeabilities are calculated with one set of measurements.

Wu, Wang, and Lee [14] completed transverse permeability measurements with a Type 3 fixture. The fixture was devised by placing a Mylar sheet with a 2.54 cm hole punched in the sheet between fabric layers to keep the flow transplanar. Silicone glue was used to seal the edges of the fabric. The entire graphite/Mylar assembly was sandwiched between two disks with 2.54 cm center holes. It was noted that difficulties arose due to edge leakage around the silicone seal.

Another method devised by Wu, Wang, and Lee [14] to measure transverse permeability was to complete a three-dimensional flow test using assumed in-plane permeabilities and back-calculate the transverse permeability from the measured inlet pressure.

A method for detecting the flow front at discrete locations using embedded fiber optic sensors was developed by Ahn et al. [15]. A 0.508 mm diameter multimode optical fiber was embedded in the preform. At selected intervals, the cladding was removed from the fiber for short lengths (< 2 mm). As the flow front passes the sensor where the cladding is removed, there is a sudden drop in the transmitted light intensity. Results were obtained for high porosity samples (0.50-0.90) of chopped glass strand mat and glass fiber woven fabric. The method used for determining principal permeabilities in 3-D relies on prior knowledge of the principal directions and also an approximation of the inlet port geometry.

Chan et al. [11] developed a method of determining the 2-D anisotropic permeabilities of a fabric. A constant flow pump was connected to a mold constructed of clear polycarbonate sheets. The flow front is measured with respect to a arbitrarily chosen Cartesian coordinate system. The angle between the chosen x-axis and the visually recorded principal axis is measured. The permeabilities in the principal directions are computed by determining the permeabilities in the chosen axes direction and completing a tensor transformation by the measured angle.

## 2.2.6 Preform Compaction

The compaction behavior of the preform/fabric is necessary to predict the maximum allowable resin pressures that can be utilized for mold filling, especially when center port injection is used. Compaction pressure is related to fiber volume fraction. If the resin pressures used are greater than the pressure caused by the initial compaction of the preform, the resin pressure will cause the preform to consolidate to a lower level of porosity. This decreases the transverse permeability and increases the resistance to flow

in the transverse direction. Also, it creates additional flow paths around the preform. This can result in non-uniform resin/fabric distribution in the finished product.

Wu, Wang, and Lee [14] completed transverse permeability experiments using fluid pressures greater than the compaction pressure of the dry preform and were able to match the compaction/permeability data to predict the pressure vs. flow rate curves for the preform.

Trevino et al. [13] found experimentally that the fabric compression force decays with time, and considered it a visco-elastic response. Also, he noted that most of the decay occurs within ten seconds.

Hammond [8] experimentally determined that the pressures needed to compact IM7 eight-harness satin weave fabric to a specific fiber volume fraction was greater than that of E-glass plain weave fabric. It was theorized to be in part a result of the greater degree of waviness in the weave pattern of the IM7. Secondly, the stiffness of the individual fibers was noted as a possible factor. Also, stitched preforms manufactured from plies consisting of unidirectional graphite fibers were tested. High compaction pressures were needed for the stitched preforms to reach a specific volume fraction. This was stated to be due to the restrictive nature of the stitching which does not allow for relaxation of the fibers during the compression process.

## 2.3 Equipment

### 2.3.1 Virginia Tech Fixture C

A dedicated in-plane permeability fixture Virginia Tech Fixture C was designed and built (see Figure 2-1 and Figure 2-2). The design drawings are included in Appendix A. The objectives were to:

- eliminate additional flow paths around the fabric caused by O-ring grooves
- ensure parallelism of the mold faces to prevent changes in fiber volume fraction across the fabric
- increase precision of measurement

- allow for advancing front permeability as well as steady-state permeability to be measured in a single fixture
- generate real-time permeability results
- ensure that the fluid inlet conditions are truly one-dimensional
- reduce time needed to evaluate samples

The fixture was designed utilizing a pre-manufactured Danly die set, with 3.18 cm diameter guide posts and brass die bushings. The manufacturer tolerance on parallelism of the two die set faces is .0025 cm. All of the components which make up the fixture have been ground, minimizing potential errors in volume fraction from non-parallel mold faces.

The fixture has been equipped with five pressure transducer locations (see Figure 2-3) - one at the inlet, three located beneath the preform, and one at the outlet. The combined non-linearity and hysterisis of the pressure transducers (Entran EPX series) is ±1% to 340 kPa and ±3/4% to 680 kPa. Also, the Entran EPX series transducers have an extremely small diameter tip (3.6 mm) for a minimal disruption of the flow pattern in the mold. The addition of the pressure transducers under the fabric allow for advancing front tests as well as steady-state permeability tests to be completed.

An LVDT has been incorporated to measure the mold height. The LVDT is accurate over its range of 1.27 cm to within 0.013 mm. The range of the LVDT is increased by the addition of high precision Grade 5 gage blocks. Preforms up to 3.81 cm thick can be tested.

The mold cavity is 17.78 cm long by 15.32 cm wide. The test fluid flows through a narrow groove oriented parallel to the preform face. This ensures that the flow is nearly one-dimensional when it reaches the leading edge of the preform.

A square O-ring and a unique O-ring seat design have been implemented to eliminate the possibility of an additional flow path around the O-ring groove (see Figure 2-4). The square O-ring is set into a recess machined around the edge of the piston. The square O-ring protrudes below the face of the piston, and is compressed against the preform. This eliminates the potential flow path located between the O-ring and the preform created by a standard O-ring groove.
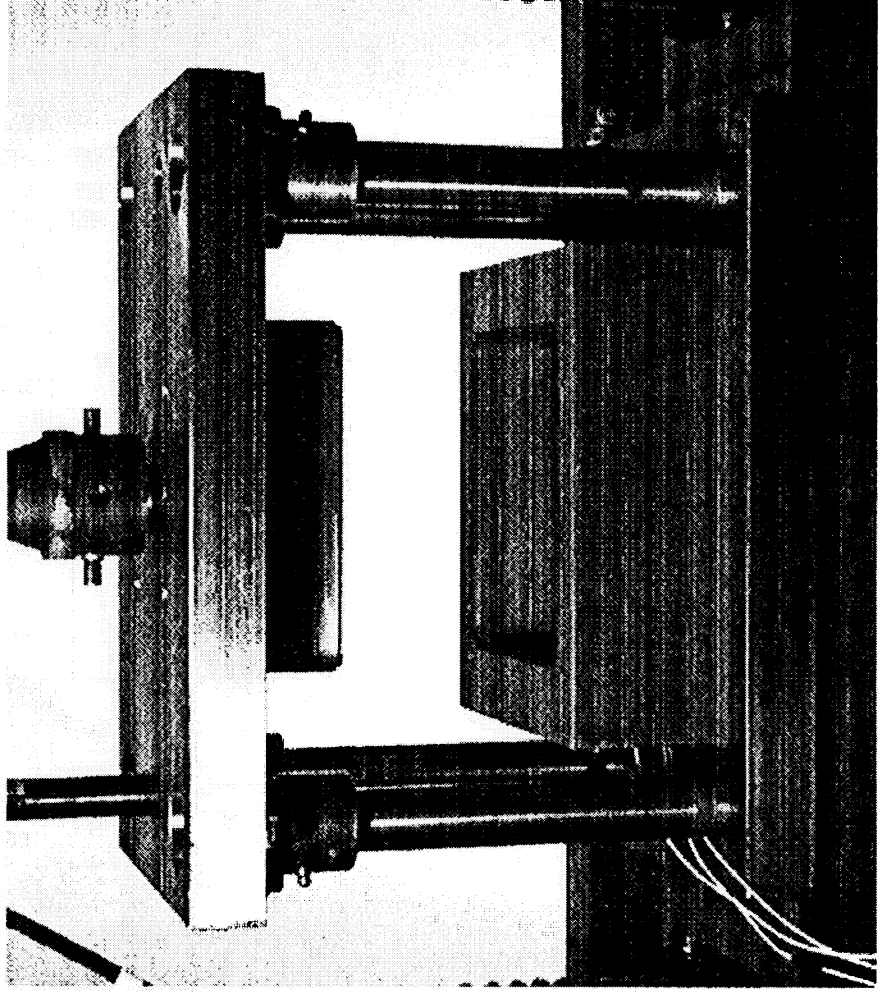
Figure 2-1    Virginia Tech Fixture C.
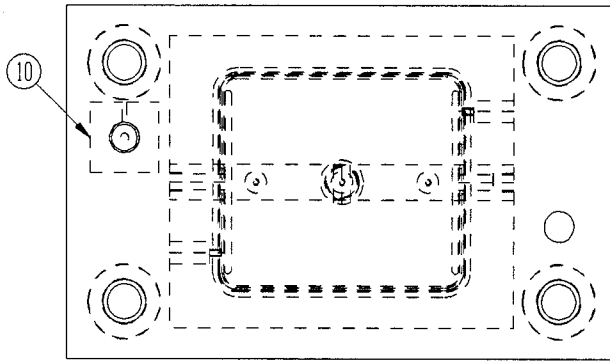
| NO. | QTY | DESCRIPTION | MAT'L |
|---|---|---|---|
| 1 | 1 | DANLY DIE SET, TOP | 1610-4C-1 |
| 2 | 1 | DANLY DIE SET, BTM | 1610-4C-1 |
| 3 | 4 | DANLY DIE SET, POST | 1610-4C-1 |
| 4 | 1 | PISTON | 6.00 X 7.00 X 1.00 CRS |
| 5 | 1 | PISTON TIP | 6.00 X 7.00 X 0.75 SS |
| 6 | 1 | CYLINDER | 8.25 X 10.00 X 1.50 CRS |
| 7 | 1 | BASE | 8.25 X 10.00 X 2.00 CRS |
| 8 | 1 | LOAD FRAME MOUNT | 1.0 DIA X 2.0 CRS |
| 9 | 2 | LVD TRANSDUCER | TRANSTEK 0352-0000 |
| 10 | 2 | LVDT CLAMP | 0.50 X 2.00 X 2.00 ALUM |
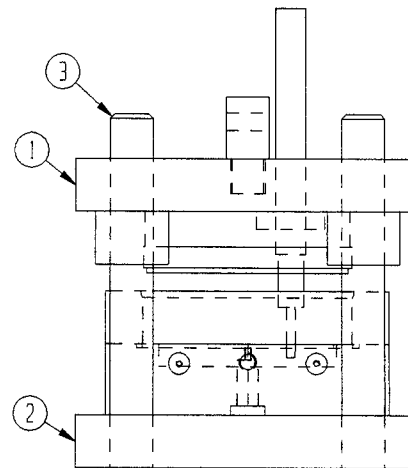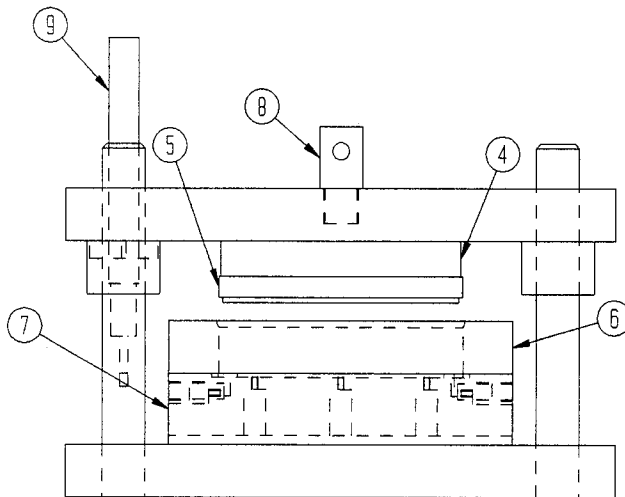
Figure 2-2     Virginia Tech Fixture C - schematic drawing.

16

OUTLET
PRESSURE
TAP

TAP
A

TAP
B

TAP
C

FLUID
INLET

FLUID
OUTLET

INLET
PRESSURE
TAP
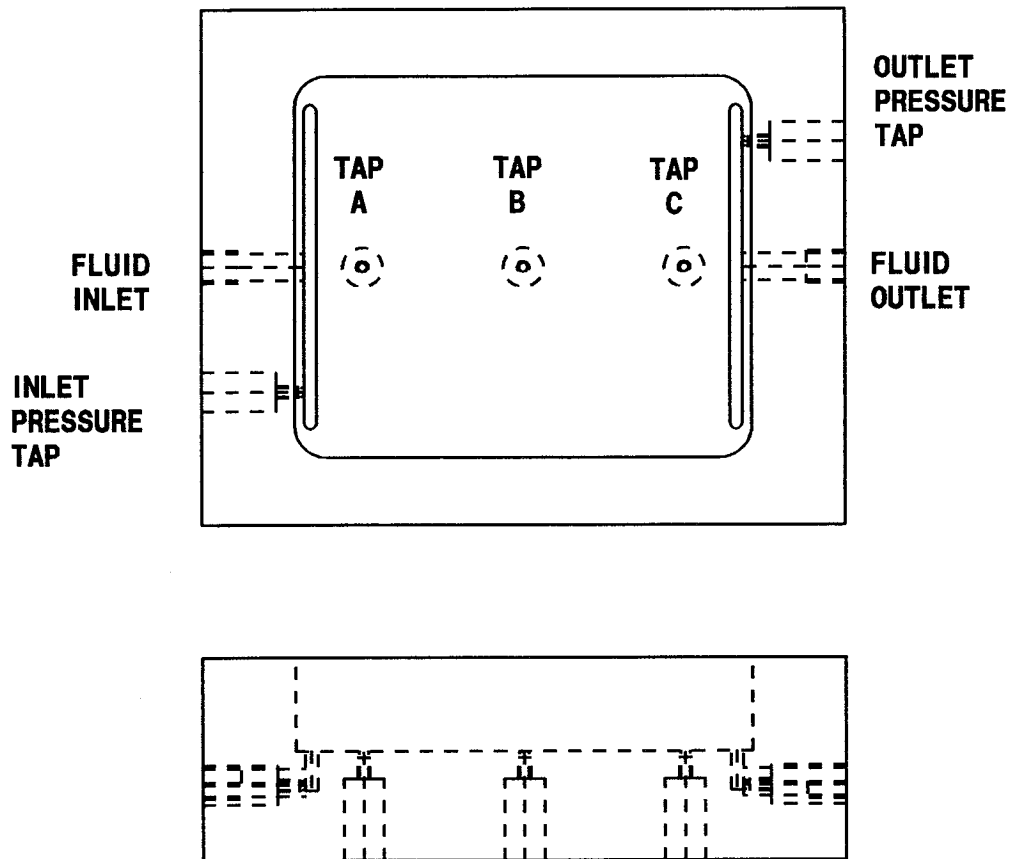
Figure 2-3    Virginia Tech Fixture C mold cavity.
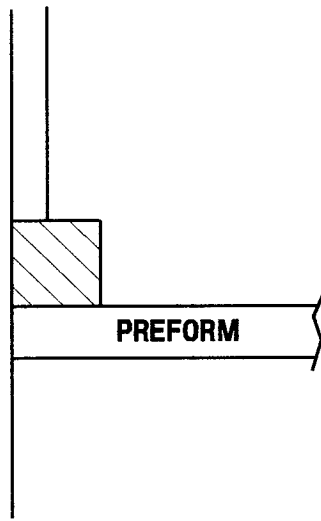
**SQUARE O-RING GROOVE**
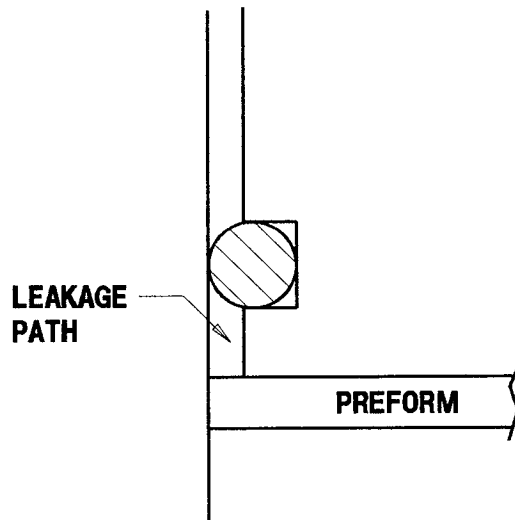
**CONVENTIONAL O-RING GROOVE**

Figure 2-4     O-ring groove design - square versus conventional.

## 2.3.2 Data acquisition

A National Instruments data acquisition system has been incorporated to allow for real-time reduction of permeability data. The system is comprised of the following:

- AT-MIO-16DE-10 multi-function I/O board for the IBM PC AT. Capable of 16 single-ended or 8 differential 12-bit analog inputs with a sampling rate of 100 kS/sec. Also, capable of 32 digital inputs/outputs.

- SCXI signal conditioning and multiplexing system. This system consists of multi-channel signal conditioning I/O modules which are installed in a modular chassis. An SCXI-1120 8-Channel Isolation Amplifier module has been incorporated, allowing for amplification and isolation of eight millivolt sources, volt sources, and thermocouples.

- LabVIEW data acquisition software. The software allows the user to program virtual instruments through the use of a graphical programming approach. It also has the capability of I/O via RS-232 ports.

The inputs measured were inlet pressure, three (3) intermediate pressures along the direction of the flow front, mold displacement, and load measurement. These inputs along with the known flow rate allowed for the direct computation of permeability, fiber volume fraction, and compaction pressure (see Figure 2-5).

The pressure transducers were calibrated across the entire range of the transducer with a dead-weight tester capable of 680 kPa. Five to ten voltage output/pressure readings were taken, and a linear least-squares fit was completed to calculate the transducer gain (volts/kPa). Prior to each test, the pressure transducer offset was set to zero the pressure readings.

The LVDT used to measure mold displacement was calibrated by closing the mold completely, ensuring that the mold was closed by displacing the piston until 4450 N was measured by the load cell. A 0.635 cm gage block was set under the LVDT tip and the LVDT was manually positioned to bring the output voltage to null. The LVDT was then bolted in place. The calibration was completed with 0.635 cm and 1.270 cm gage blocks.
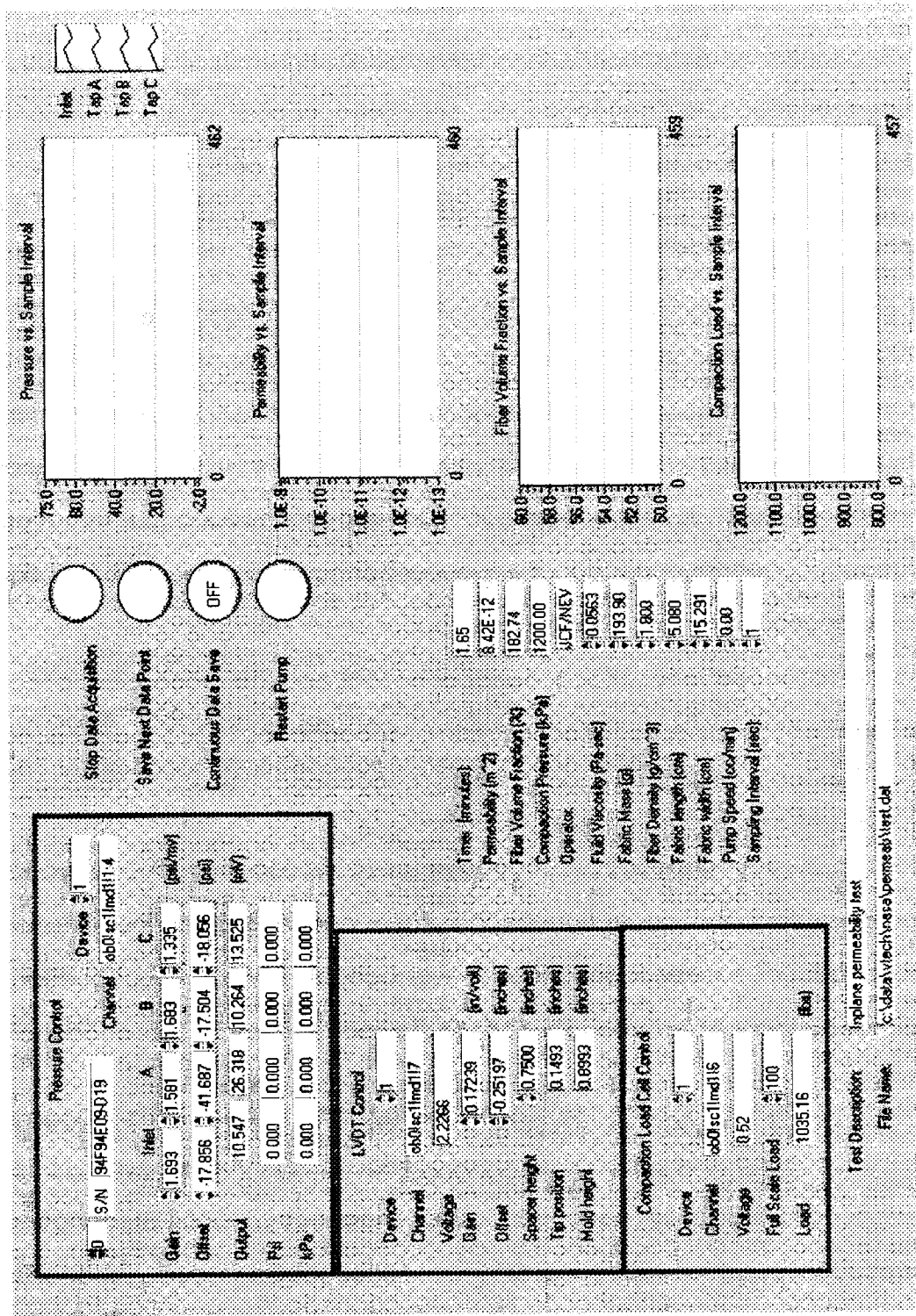
Figure 2-5    In-plane permeability measurement - LabVIEW front panel.

Three voltage readings were taken at displacements of 0.000 cm, 0.635 cm, and 1.270 cm. A linear least-squares fit was then completed to calculate both the gain and the offset for the LVDT.

The load cell was calibrated prior to each test. With the upper mold attached to the load cell, the offset and gain were set so that the output voltage was null.

### 2.3.3 Constant flow pump

A Parker Zenith® Precision Gear Metering Pump was implemented as an alternative to the use of a pressure pot for fluid delivery. The advantages of controlling the fluid flow rate are as follows:

- ease of pressure measurement as opposed to flow rate measurement
- the ability to automate the fluid delivery
- ability to dispense a given volume of fluid

The Series BPB-.297 pump is capable of the following:

- flow rates from 1.00 to 50.00 cc/min.
- inlet pressures from 50 mm Hg vacuum to 2070 kPa
- discharge pressures of 5171 kPa
- viscosities from .01 to 1,000 Pa-s
- All seals are metal or Teflon (with Viton backup rings)

The high turn-down ratio was achieved by the addition of a PowerTek brushless D.C. servomotor used to drive the pump. The entire pump system communicates via a RS-422 serial port, directly controlled by the LabVIEW data acquisition system.

## 2.4 Materials

Four types of textile reinforcements were characterized during the course of this investigation. They include:

- Style 162 E-glass. A plain weave, bi-axial fiberglass fabric. The areal weight per ply is 392 g/m$^2$.

- IM7/8 HS. An eight harness satin carbon fabric with 6K tows of IM7 carbon fiber in a 0°/90° orientation. The fabric has the same number of tows in the warp and fill direction and the areal weight per ply is 440 g/m$^2$.

- Multiaxial warp knit carbon preform [16]: Composed of a 9-ply subgroup with a [±45,0$_2$,90]$_s$ layup. The fiber material was AS4 or IM7. Subgroups are knitted together with a polyester alternating tricot/chain knit. The subgroups are stitched in the 0° direction, 0.476 cm apart with 20.32 stitches per centimeter. The areal weight of the 9-ply subgroup is 1425 g/m$^2$.

- Braided/woven stiffener. The braided/woven configuration [16] consists of triaxially braided tubes and woven fabric that are stitched together in the blade area of the T-stiffener. The triaxially braided tubes were fabricated from AS4 6K graphite fiber in the ±45° direction and either AS4 12K or IM7 12K/2E graphite fiber in the 0° direction. The plain weave fabric was woven with AS4 6K graphite fiber and had the same yarn count in the warp and fill directions.

## 2.5 Measurement Techniques

### 2.5.1 Advancing Front and Steady-State Permeability

There are two common methods for measuring the permeability of the fabrics and preforms. These are known as the steady-state permeability and the advancing front permeability test methods.

The advancing front test is carried out with a dry preform, and a fluid is pumped through the preform either at a constant velocity or constant pressure. The flow front position is measured either visually or from pressure transducer feedback. The permeability can then be calculated from Darcy's law.

Steady-state permeability is measured after the preform has been saturated, and is carried out under constant flow rate injection. The pressure differential is measured across the length of the preform, and the permeability can then be determined from Darcy's law.

The advancing front test has the advantage of measuring the permeability under conditions more closely resembling those seen in the resin transfer molding process and can account for the wetting characteristics and capillary effects of the dry preform. The drawback is that full characterization for a fabric is time-consuming and costly since a new preform must be used to measure permeability at each volume fraction. The steady-state test allows for one preform to be used to fully characterize the material at all volume fractions. Experimental work by Hammond [8] has shown that for materials such as IM7/8HS carbon fiber and 162 E-glass preforms, the permeability values for advancing front and steady-state tests are similar at high fiber volume fractions and low flow rates.

## 2.5.2 Verification of Flow Front Measurement Technique

Tests have been completed to verify the use of a pressure transducer signal as an indication of the flow front position. An advancing front permeability test was completed in a one-dimensional flow fixture with a Plexiglas window [8] to visually observe flow front position and pressure transducers to sense the flow front position (see Figure 2-6). A line source flow front was introduced to the edge of the fabric. Two transducers were located beneath the preform. As the flow front passed 1.27 cm intervals marked on the surface of the Plexiglas, a push-button was depressed to digitally record the time on the data acquisition system. The pressure transducer signals were then compared with the visually recorded flow front positions. The results showed (Figure 2-7) that the flow front passes over the transducer at the inflection point on the pressure versus time curves. Taking the derivative of pressure with respect to time and plotting the results versus time (Figure 2-8) shows that the minima of the derivative can be used as an indication of flow front position.
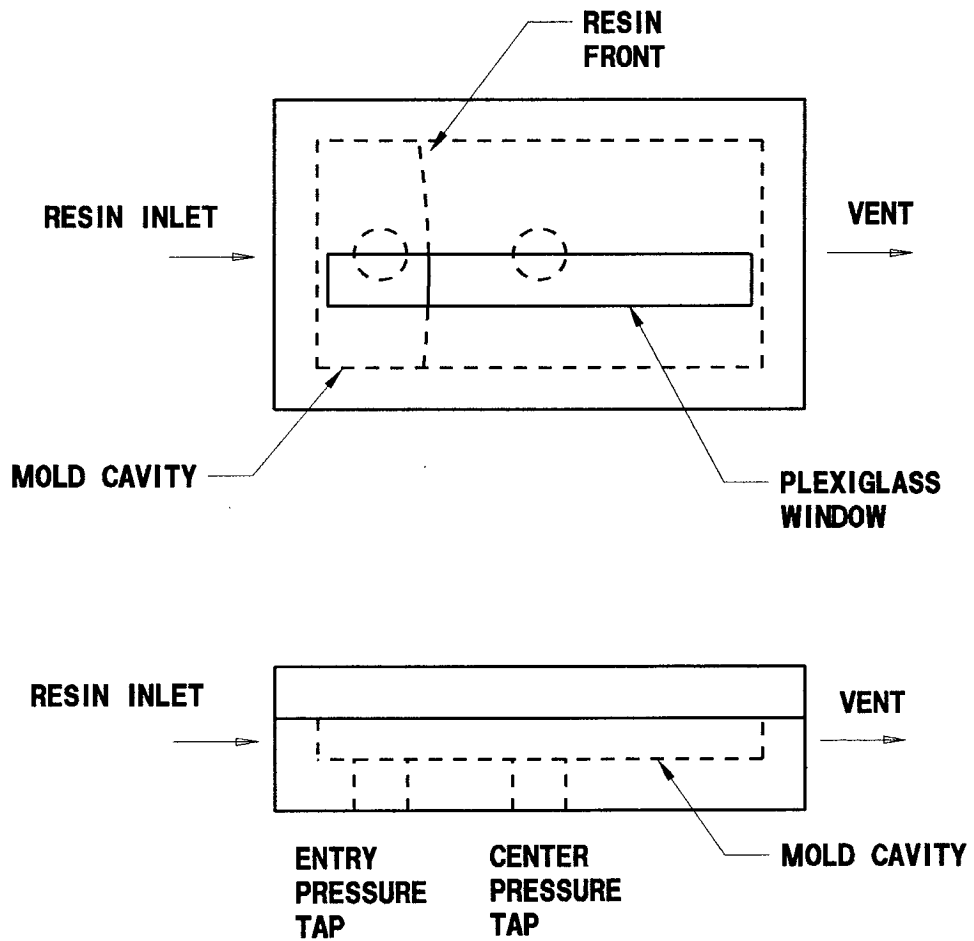
Figure 2-6     Schematic diagram of advancing front permeability experimental setup.
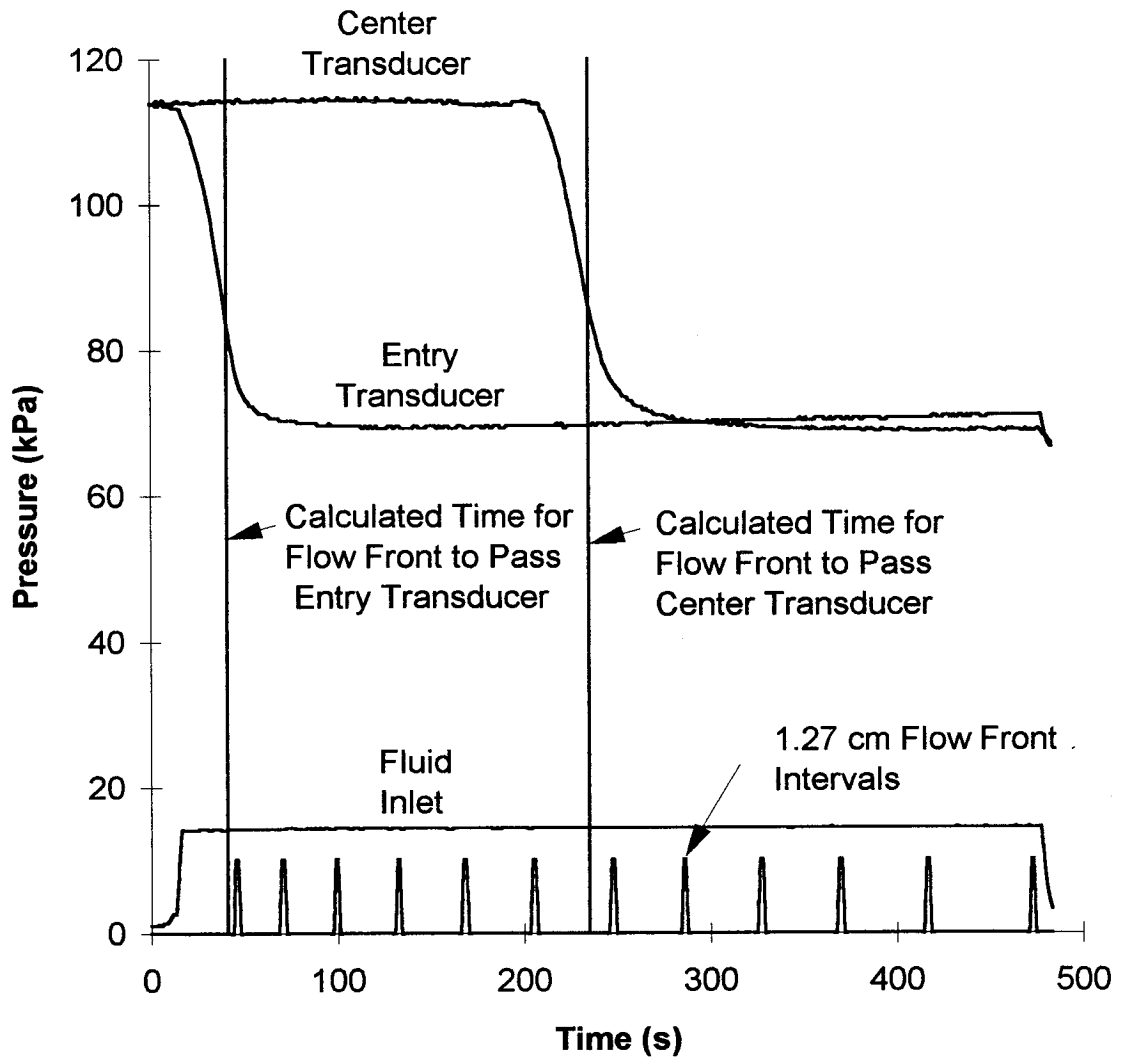
Figure 2-7    Advancing front test - pressure versus time.
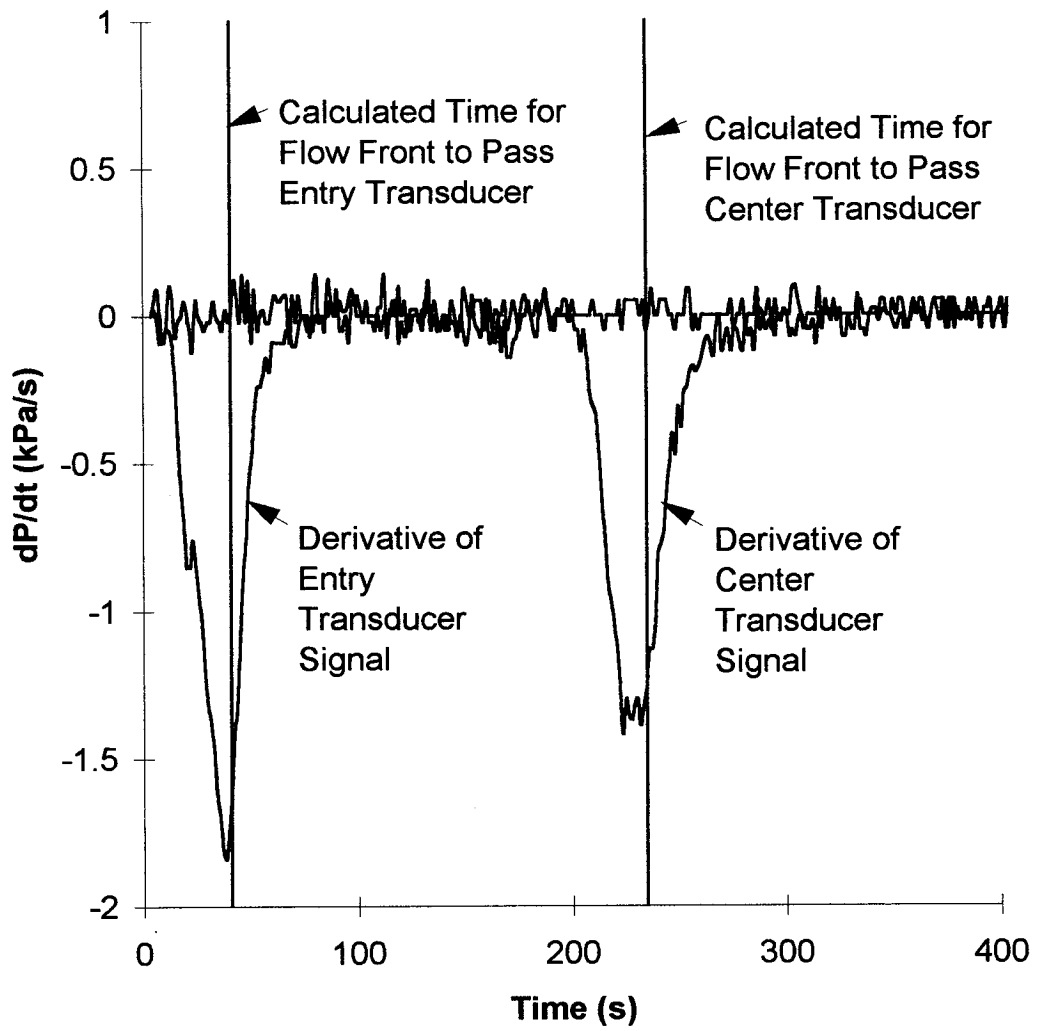
Figure 2-8      Advancing front test - pressure derivative versus time.

## 2.6 Experimental Results

### 2.6.1 Comparison of Permeability Measured with Two Fixtures:

The permeability of E-glass fabric was measured in the warp direction with the fixture described in Section 2.3 (Fixture C) and compared with data obtained [8] with an older fixture (Fixture B). Fixture B was a Type 4 fixture, designed for 15.24 x 15.24 cm thin preforms. The O-ring groove design of Fixture B was of the conventional type (see Figure 2-4). The intent was to verify the repeatability and accuracy of Fixture C and to explain any differences that might occur.

The results of the warp direction permeability measurements obtained with Fixture B and Fixture C are shown in Figure 2-9. The preforms tested were 15.24 cm long and 15.24 cm wide and 18 plies thick. The results from the two fixtures agree well. The inlet pressure versus flow rate curves measured with Fixture C (see Figure 2-10) are linear and the intercepts pass through the origin. Hence, the one-dimensional form of Darcy's law can be used to determine permeability.

To obtain a measure of experimental error for permeability measurements the same test was replicated five (5) times with E-glass as a test material on Fixture C. The results are shown in Figure 2-11. The permeability data for Fixture C was then fit to a power-law regression model:

$$S = a\left(v_f\right)^b \tag{2-16}$$

$S$: Permeability $(m^2)$

$v_f$: fiber volume fraction

$a, b$: fitted constants

27
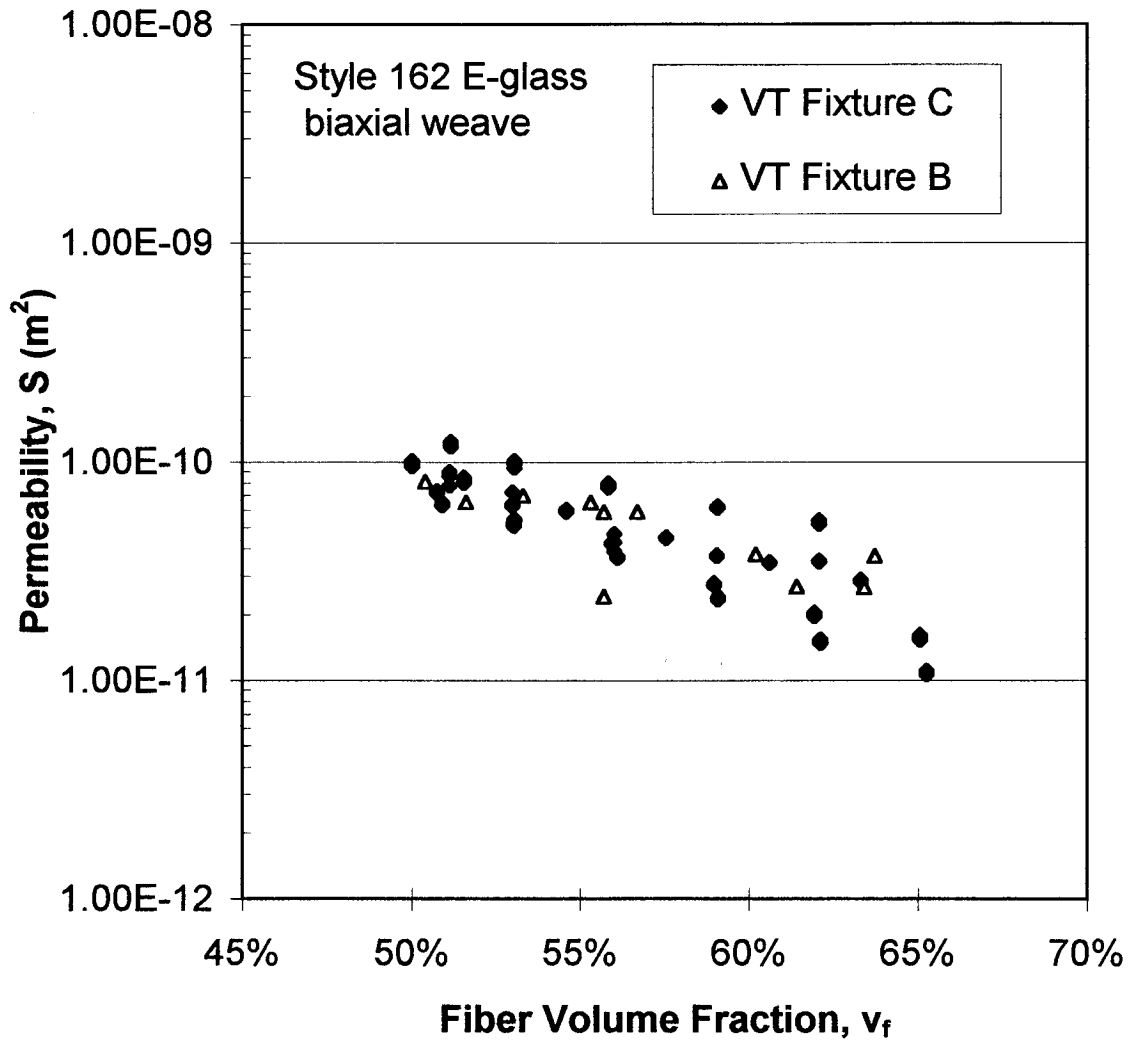
Figure 2-9    Fixture to fixture permeability comparison, E-glass.
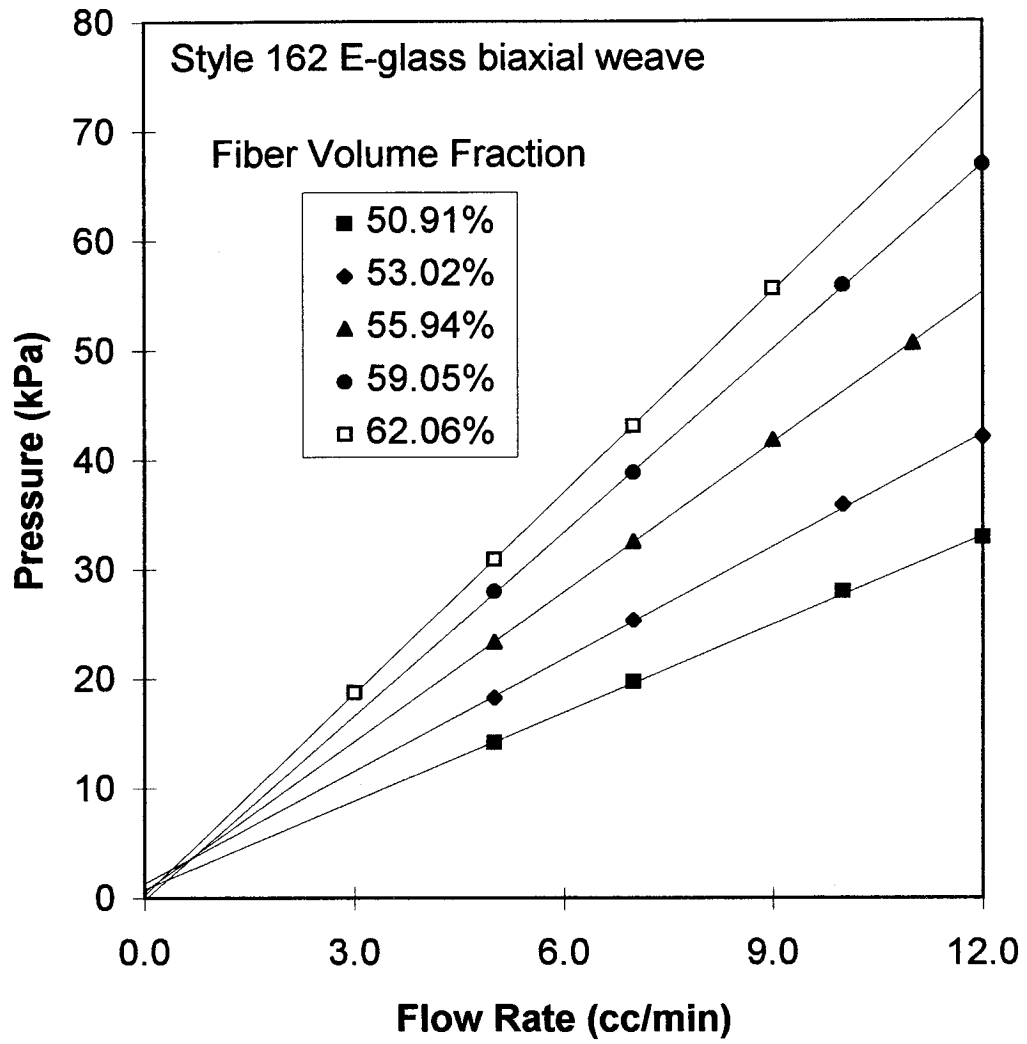
Figure 2-10    Pressure versus flow rate - E-glass.
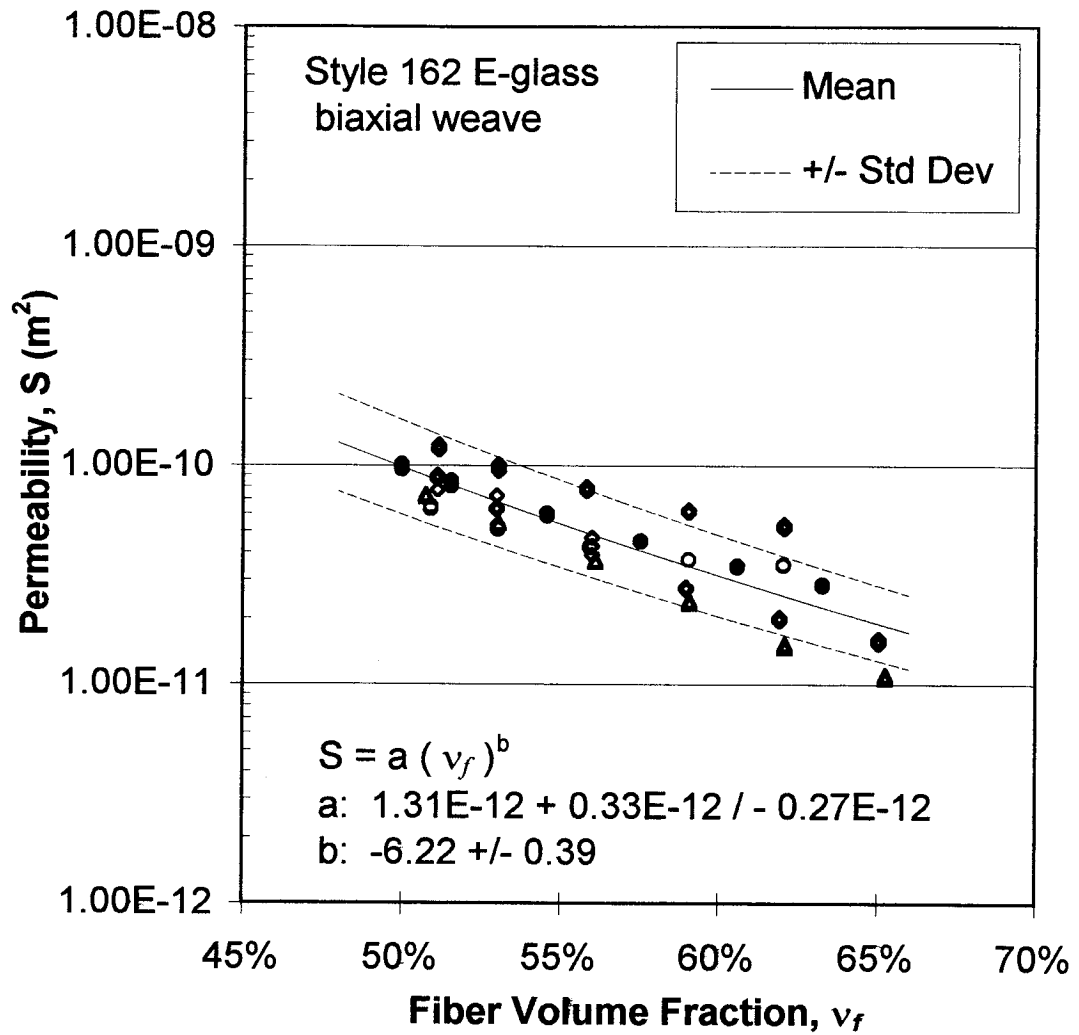
Figure 2-11    Repeatability of warp direction E-glass permeability measured with Fixture
C.

The error in the permeability power-law regression model is the sum of experimental error and error due to lack of fit. Experimental error is comprised of error due to nonhomogeneity of material and error of measurement. A measure of experimental error can only be obtained by fixing all of the independent variables and replicating the experiment [17].

The variance of parameters $a$ and $b$ from the power-law regression model was calculated and the limits of one standard deviation of both parameters was plotted. The definition of one standard deviation is that 68% of the measurements will fall within that interval, assuming a normal distribution of the data.

## 2.6.2 IM7/8HS Fabric Permeability Measurements:

The in-plane permeabilities of IM7/8HS were measured with Fixture C and compared to permeability measurements obtained with Fixture B, along with earlier data obtained by Hammond [8] with Fixture B. Measurements were made in both the warp and fill directions (see Figure 2-12 and Figure 2-13).

Hammond's power law fits are slightly higher for both the warp and fill direction as compared to the measurements made during this investigation on Fixture B and C. These differences could be accounted for by nonhomogeneity of material or slightly different measurement techniques.
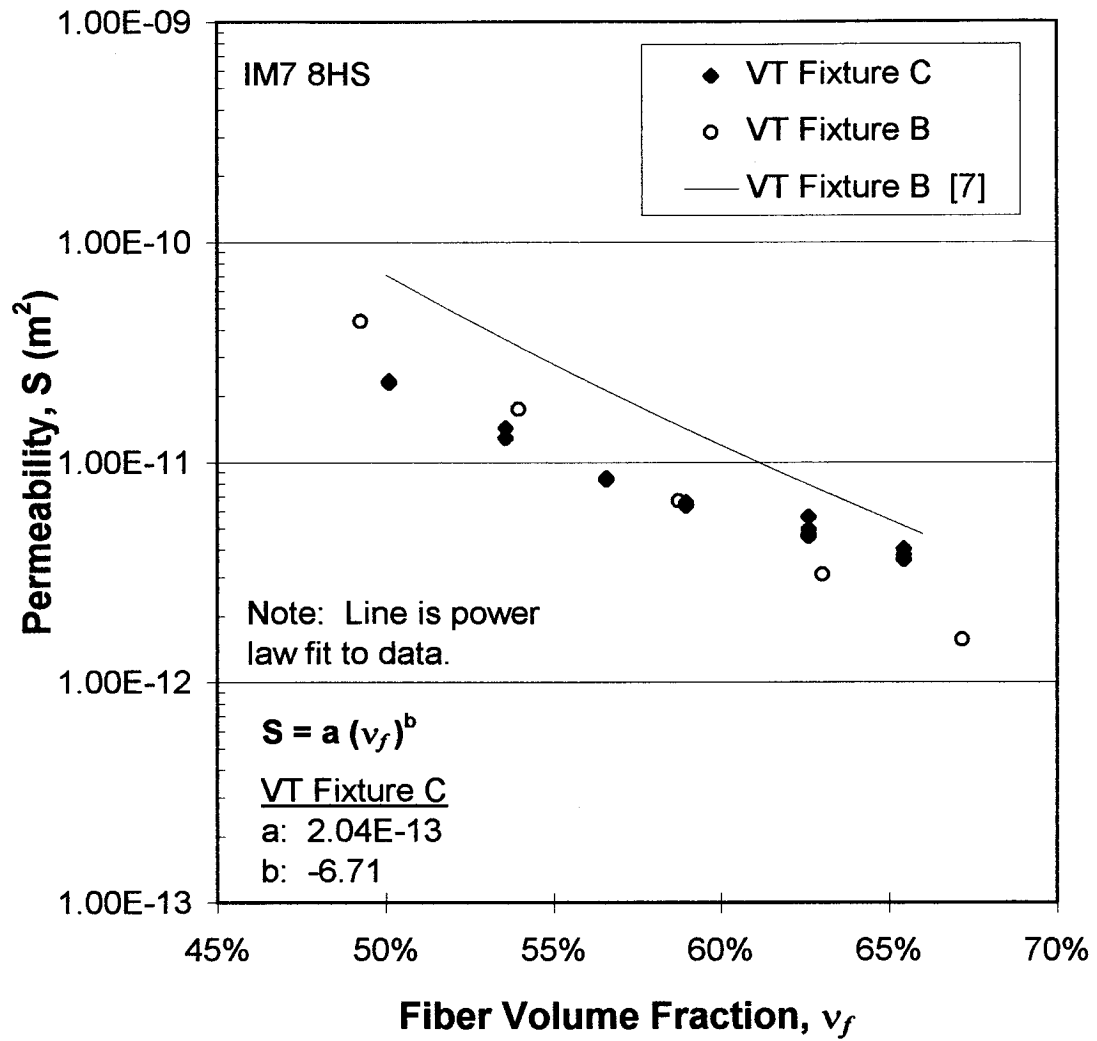
Figure 2-12    IM7 permeability versus volume fraction - warp direction.
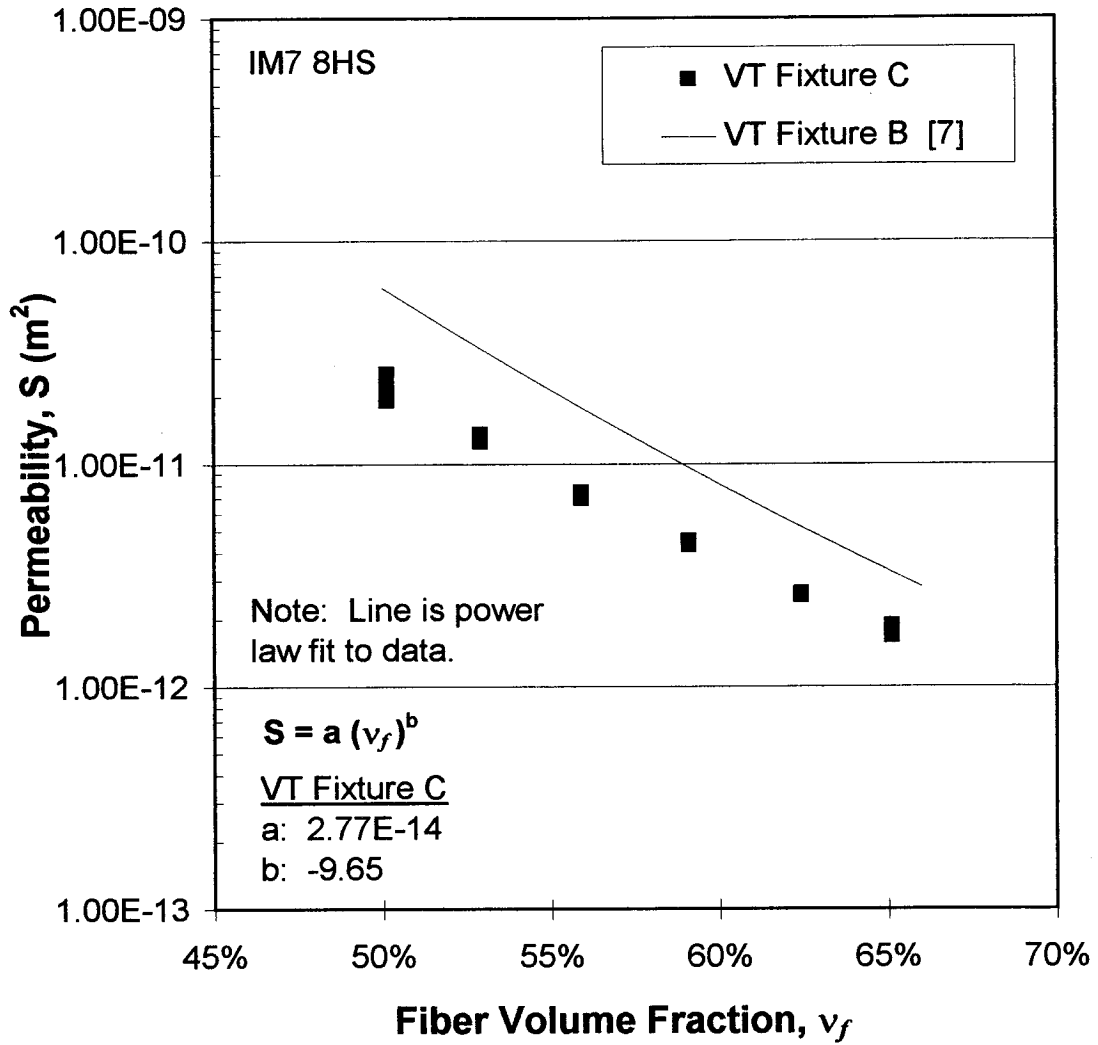
Figure 2-13    IM7 permeability versus volume fraction - fill direction.

## 2.6.3 Advancing front versus steady state permeability

The advancing front and steady-state permeabilities of 18-ply plain weave E-glass in the warp direction were measured at a fiber volume fraction of 55.4%. The permeabilities were measured from a single test with Fixture C. The pressure data are presented in Figure 2-14. The transducer readings at Tap A and Tap C were used to calculate advancing front permeability (see Figure 2-15) . The advancing front permeability was calculated as follows:

$$S(x) = \frac{Q \eta x}{h w P(x)} \tag{2-17}$$

$$x = v_x(t - t_o) \tag{2-18}$$

$x$: distance measured from 1st transducer

$P(x)$: pressure measured at 1st transducer

$t_o$: time when flow front passes 1st transducer

$h$: mold cavity height

$w$: mold cavity width

$v_x$: interstitial fluid velocity

The steady-state permeability and advancing front permeability data compare well. It was noted from the advancing front experiment that the fluid velocity at the center of the mold is lower than the fluid velocity at the edges of the mold. The average interstitial velocities calculated from flow front data measured at the pressure taps and the average interstitial velocity calculated from the inlet volumetric flow rate are presented in Table 2-1.
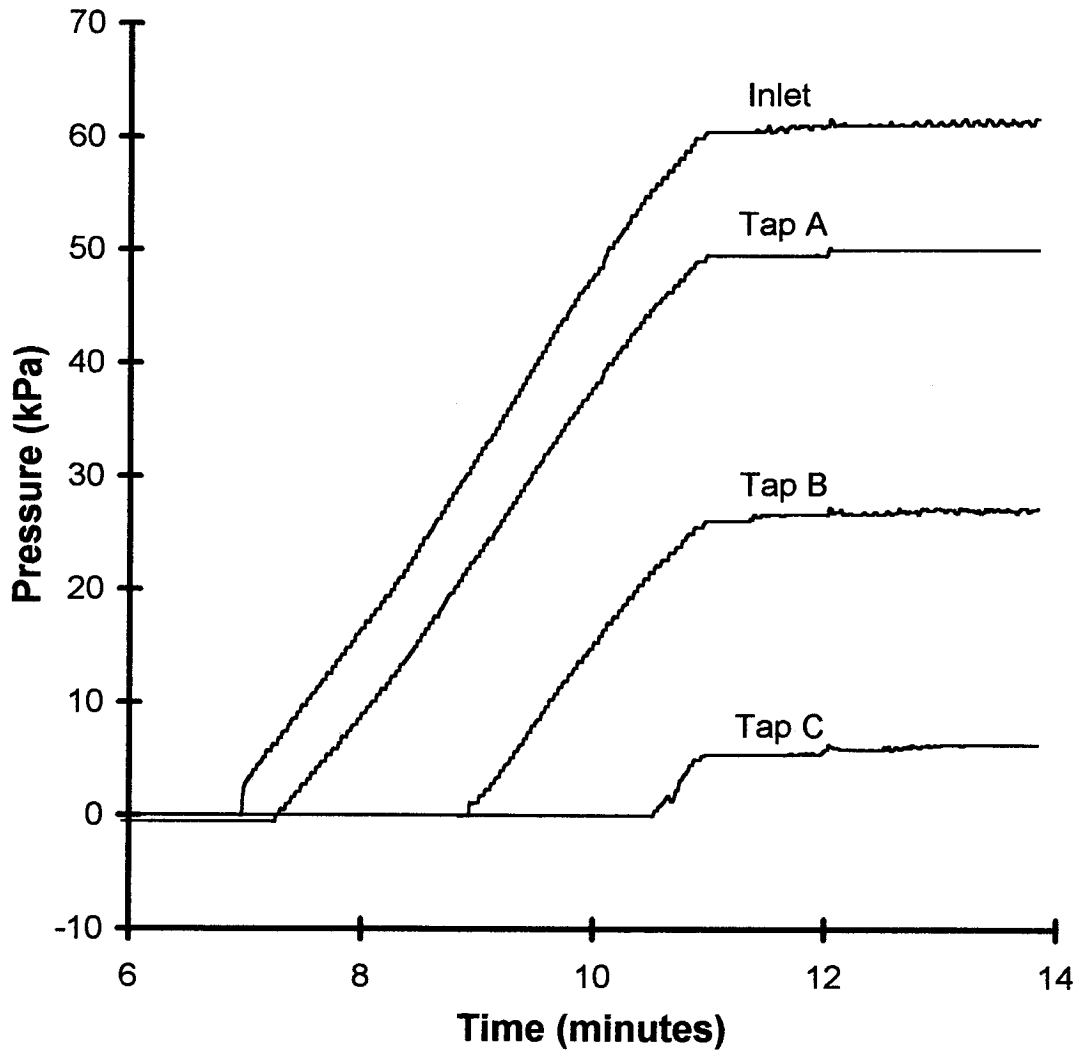
Figure 2-14    Pressure data for steady-state/advancing front test of E-glass at 55.4%
fiber volume fraction.
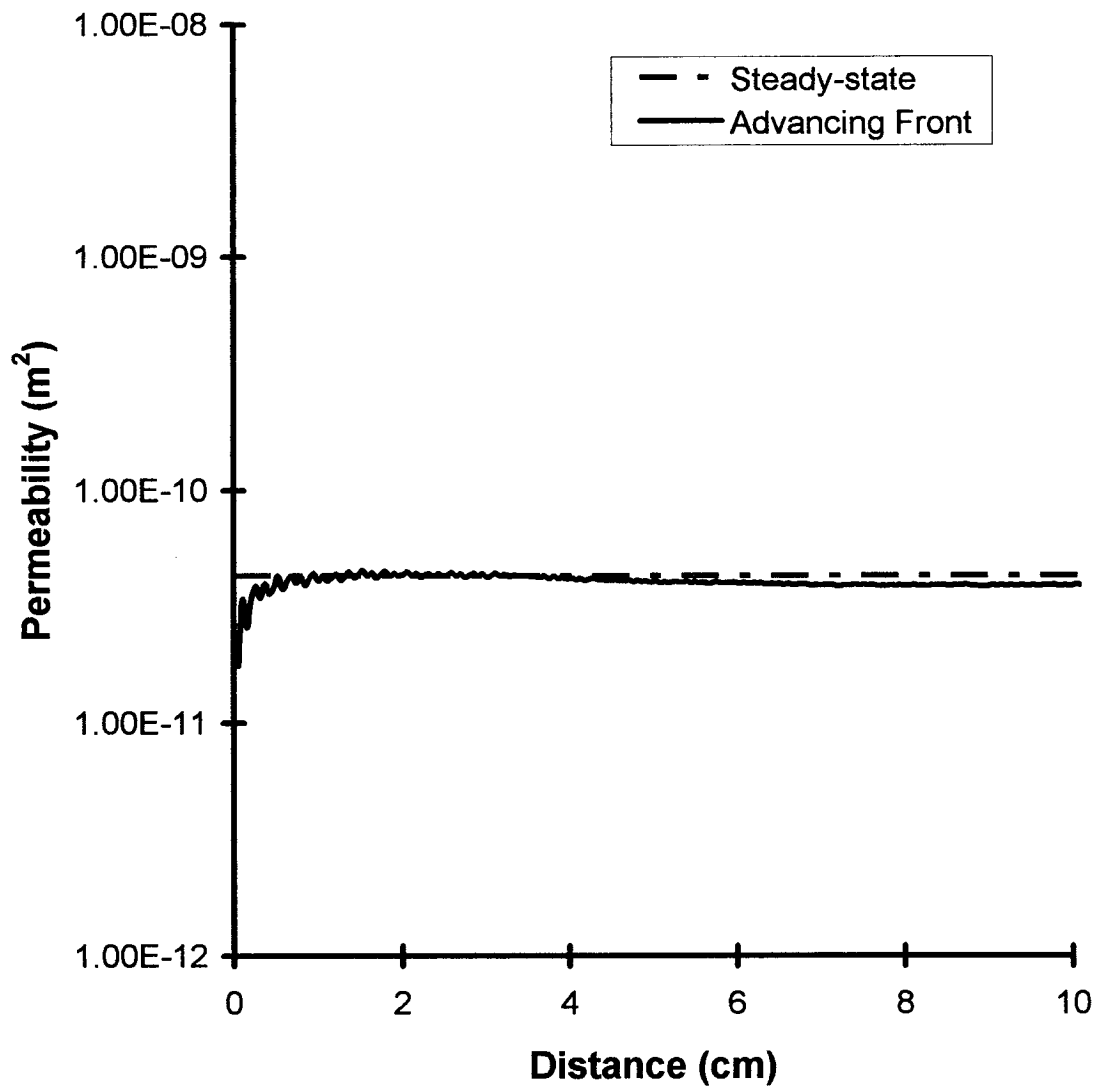
Figure 2-15    Advancing front and steady-state permeability of E-glass at 55.4% fiber

volume fraction.

Table 2-1    Interstitial fluid velocities for E-glass permeability test.

| | Interstitial Velocity (cm/min.) |
|---|---|
| Tap A - Tap B | 3.18 |
| Tap A - Tap C | 3.14 |
| Tap B - Tap C | 3.08 |
| Average based on inlet volumetric flow rate | 4.12 |

The average interstitial velocity between transducer location was calculated as follows:

$$v_x = \frac{t_2 - t_1}{\Delta x} \qquad (2\text{-}19)$$

$t_2$:  time at which flow front passes 2nd transducer

$t_1$:  time at which flow front passes 1st transducer

$\Delta x$:  distance between two transducers

The average interstitial velocity based on inlet volumetric flow rate was calculated as follows:

$$v_x = \frac{Q}{w\,h\,\phi} \qquad (2\text{-}20)$$

Therefore, there are some edge effects which take place in the permeability measurement. Assuming that the flow front is fully developed by the time it reaches Tap B, the measured interstitial fluid velocity of the flow front at the center of the mold is 75% that of the average fluid interstitial velocity. The effect that this might have on overall permeability measurement is difficult to quantify since the interstitial velocity distribution at the flow

front is not uniform. The factors which can influence the magnitude of the edge effect on permeability are:

- permeability in the fill direction
- width of the edge effect region
- permeabilities of the edge effect region in warp and fill direction

## 2.6.4 Off-axis permeability measurement:

Measurements of the off-axis permeabilities (see Figure 2-16) in the plane of the preform were completed to verify the orientation of the principal axes. The samples measured were 81 ply preforms, fabricated from nine multi-axial warp knit subgroups. The subgroups were stitched through-the-thickness with Kevlar stitching, with a stitch spacing of 1.27 cm and a pitch of 0.318 cm. The steady-state permeabilities were measured for three samples in the following directions:

- Parallel to the stitching
- Perpendicular to the stitching
- 45° to the stitching

The experimental permeability results were then fit to a power-law regression model (see Table 2-2).

Table 2-2     Power-law regression constants for permeability model - 81 ply multi-axial warp-knit preform.

| Direction | a (m$^2$) | b (unitless) |
|-----------|-----------|--------------|
| Parallel | 9.93E-15 | -1.31E+01 |
| Perpendicular | 1.50E-14 | -1.03E+01 |
| 45° | 9.46E-15 | -1.19E+01 |
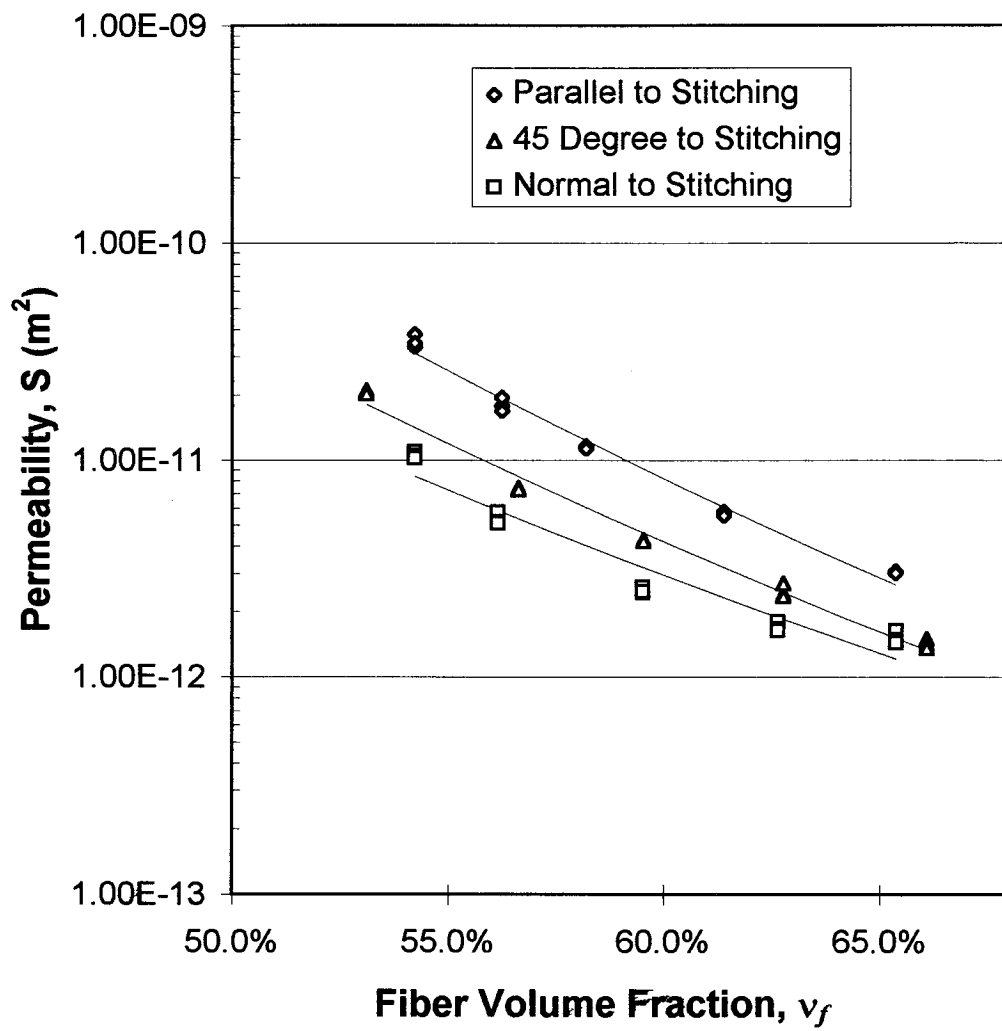
Figure 2-16    Permeability data and power-law regression fits, 81 ply multi-axial warp
knit preform.

The permeability ($S'_{ij}$) is a second order tensor and transforms according to:

$$S'_{ij} = a_{ik} \, a_{jl} S_{kl} \qquad i,j,k,l \rightarrow 1,2 \qquad\qquad (2\text{-}21)$$

where $S'_{ij}$ is the transformed permeability, $S_{ij}$ is the original permeability and $a_{ik}$ , $a_{jl}$ are the direction cosines. When rotation is about the z-axis the direction cosines, permeability tensor, and the transformed permeability can be written respectively as

$$\overline{\overline{a}} = \begin{bmatrix} \cos\theta & \sin\theta \\ -\sin\theta & \cos\theta \end{bmatrix} \qquad\qquad (2\text{-}22)$$

$$\overline{\overline{S'}} = \begin{bmatrix} S'_{xx} & S'_{xy} \\ S'_{xy} & S'_{yy} \end{bmatrix} \qquad\qquad (2\text{-}23)$$

$$\overline{\overline{S}} = \begin{bmatrix} S_{xx} & S_{xy} \\ S_{xy} & S_{yy} \end{bmatrix} \qquad\qquad (2\text{-}24)$$

For the permeability measurements taken, the original x-axis (see Figure 2-17) corresponds to the direction in which the parallel to stitching permeability ($S_{xx}$) was measured and the y-axis corresponds to the direction in which the perpendicular to stitching permeability ($S_{yy}$) was measured. When $\theta = 45°$, the x'-axis corresponds to the direction in which the 45° to the stitching permeability ($S'_{xx}$) was measured. The equation for $S'_{xx}$ then simplifies to

$$S'_{xx} = S_{xy} + S_{xx} + S_{yy} \qquad\qquad (2\text{-}25)$$
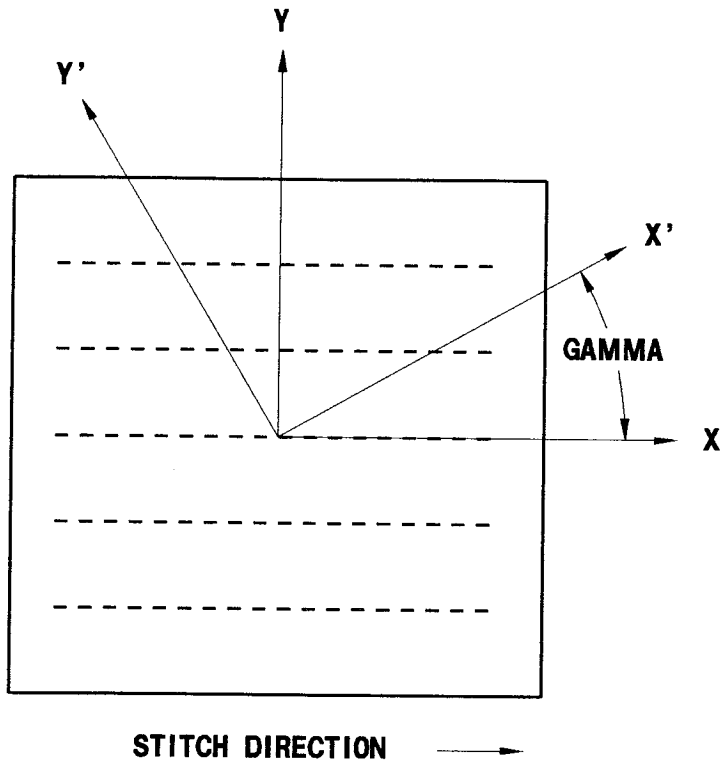
Figure 2-17    Coordinate system - off-axis permeability component measurement.

and the off-axis permeability tensor component $S_{xy}$ is computed. The permeability tensor $\overline{\overline{S}}$ was then rotated to find the direction of the principal axes (see Figure 2-18) and principal permeability values (Figure 2-19) as a function of fiber volume fraction by solving the following system of equations for the eigenvalue and eigenvector:

$$\left(S_{ij} - S\delta_{ij}\right)n_j = 0 \qquad i, j \to 1,2 \tag{2-26}$$

$$n_i n_i = 1 \tag{2-27}$$

where $S$ is the principal permeability and $n_i$ is the principal direction vector. The angle of rotation ($\gamma$) can be computed from the eigenvector as follows:

$$\gamma = \tan^{-1}\left(n_2/n_1\right) \tag{2-28}$$

When the principal permeability values are plotted as a function of fiber volume fraction, they are found to be nearly equal to the permeability values measured parallel and perpendicular to the stitching (see Figure 2-19). Although the principal axes was calculated to be 13° from the stitching axes, it is possible that this variation is due to experimental error since the principal permeabilities lie within one standard deviation of the power law regression model fit for the permeabilities calculated parallel and perpendicular to the stitching.

This method of computing the principal permeabilities and principal directions has the advantage of allowing the direction to be measured as a function of fiber volume fraction, and all results are obtained from three tests in a single fixture.
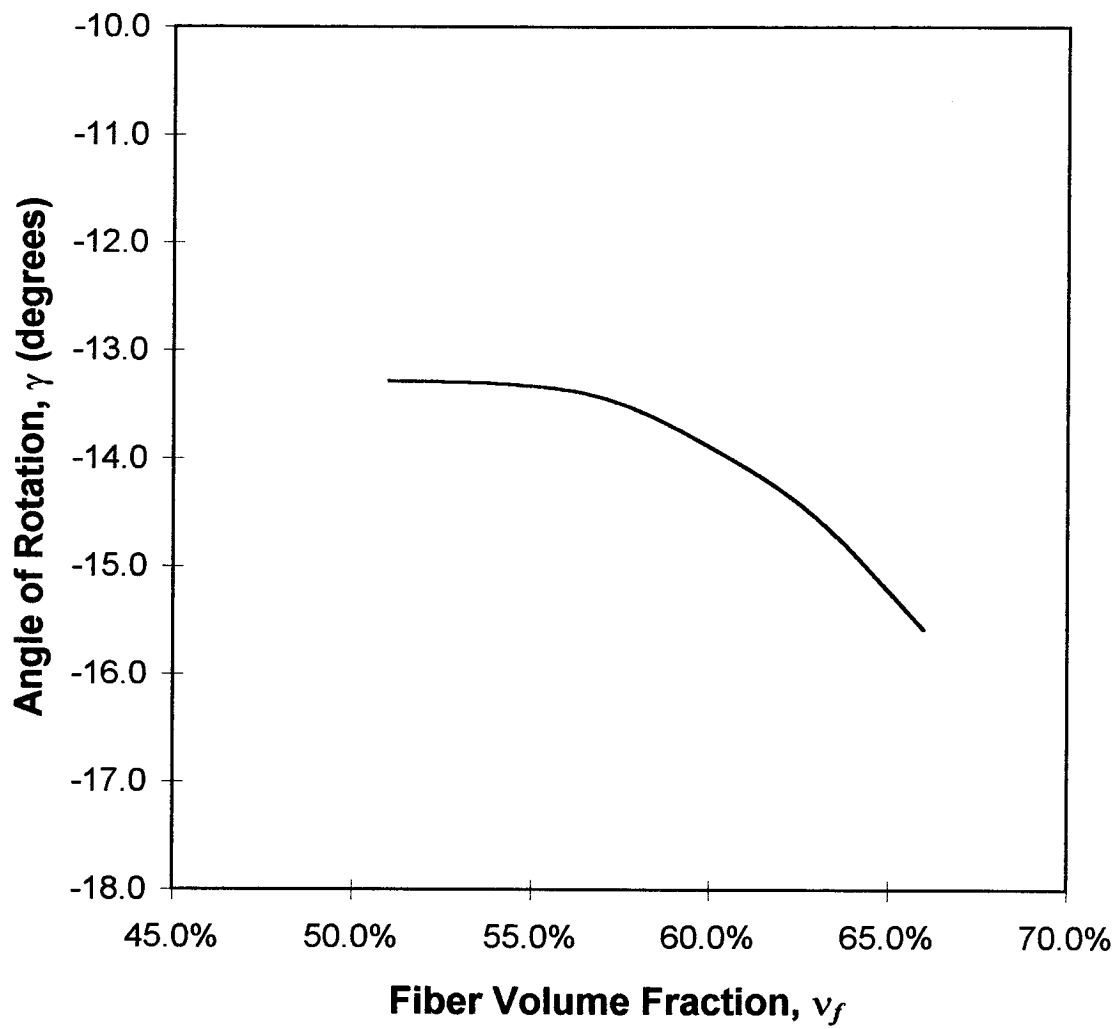
Figure 2-18    Angle of rotation from original coordinate axes aligned with preform
stitching to principal permeability axes.
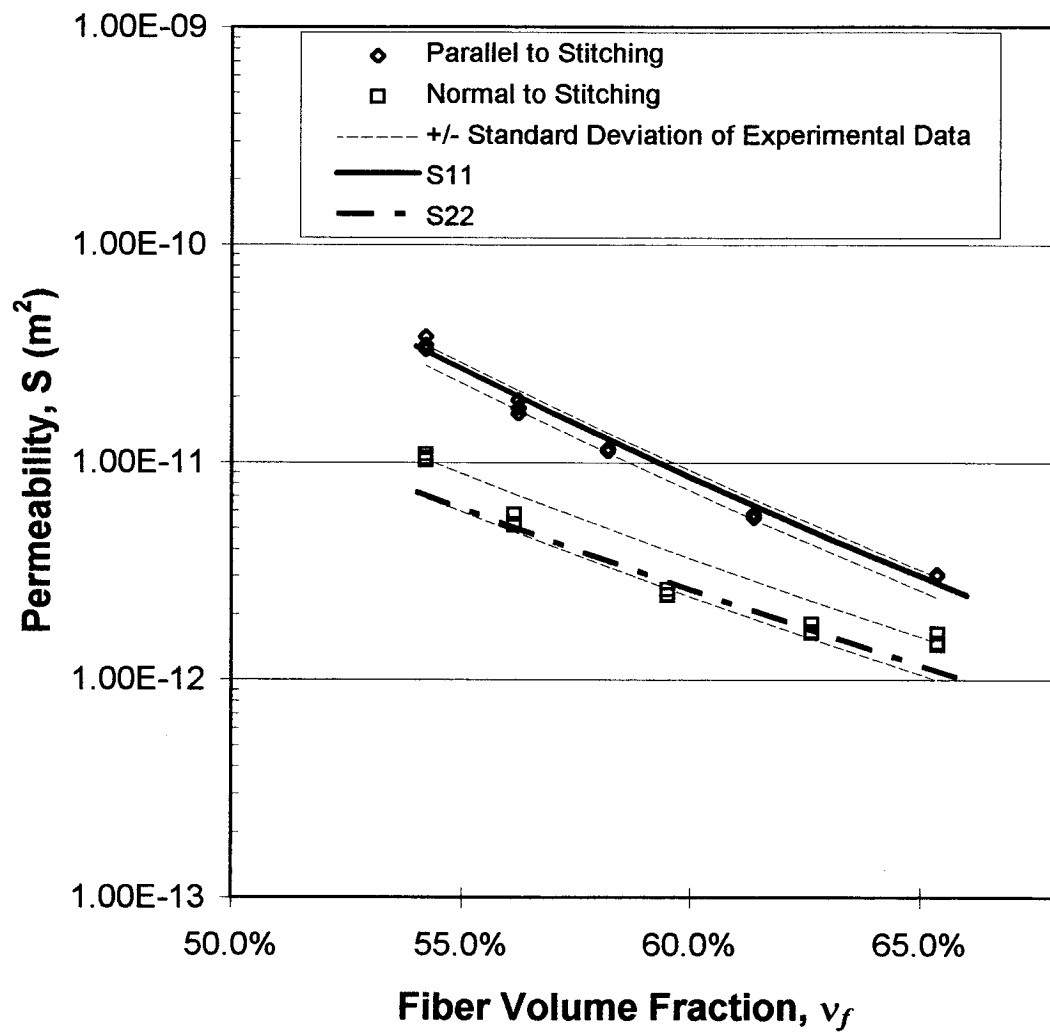
Figure 2-19    Principal permeabilities and +/- standard deviations of permeability data measured parallel and normal to the stitching direction.

## 2.6.5 Blade-stiffened panel component compaction

A blade-stiffened preform (see Figure 2-20) was fabricated from a 54 ply multi-axial warp knit preform and a braided/woven stiffener. The areal weights were 8800 g/m$^2$ and 10900 g/m$^2$, respectively. The 54 ply preform was assembled with six 9-ply subgroups, stitched through-the-thickness with Kevlar stitching in the 0° direction with a stitch spacing of 1.27 cm and a pitch of 0.32 cm. The braided/woven stiffener flanges were then stitched through-the-thickness to the 54 ply preform with Kevlar stitching, aligning the stiffener with the 0° direction of the 54 ply preform. The flanges were stitched in the 0° direction with a stitch spacing of 0.63 cm and a pitch of 0.32 cm. Measurement of the 54 ply preform and the braided/woven stiffener compaction characteristics in the through-the-thickness direction was completed utilizing Fixture C. The results of the compaction characterizations (see Figure 2-21 and Figure 2-22) were fit to a power-law regression model:

$$v_f = a(P)^b \tag{2-29}$$

$v_f$: fiber volume fraction

$P$: compaction load

$a, b$: constants

The power-law regression parameters are presented in Table 2-3.

Table 2-3    Power law regression parameters for volume fraction versus compaction pressure model.

| Component | a (1/kPa) | b (unitless) | Compaction pressure at 55% volume fraction (kPa) |
|---|---|---|---|
| Skin | 3.49E-01 | 8.65E-02 | 192.0 |
| Blade | 3.92E-01 | 5.94E-02 | 300.0 |
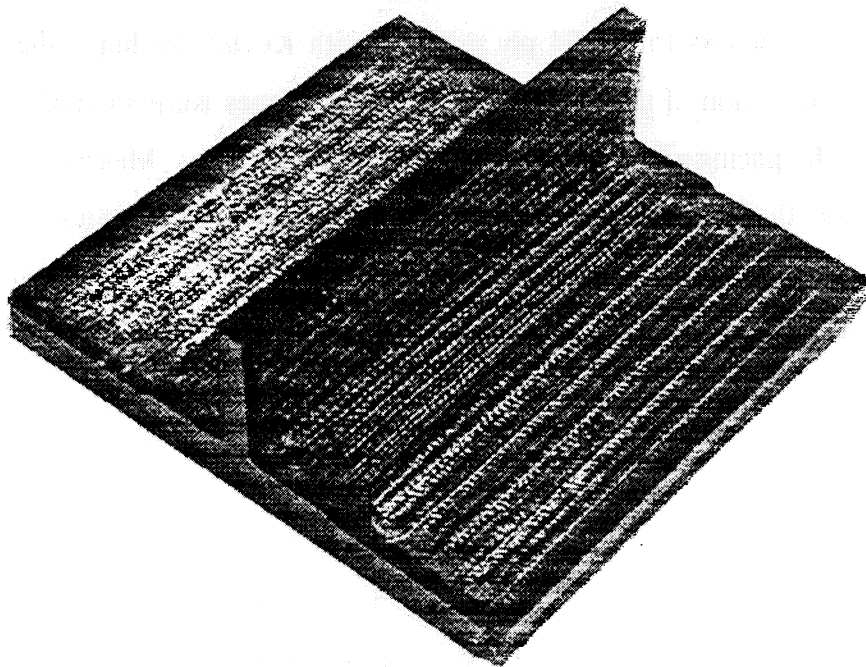
Figure 2-20    Blade-stiffened preform.
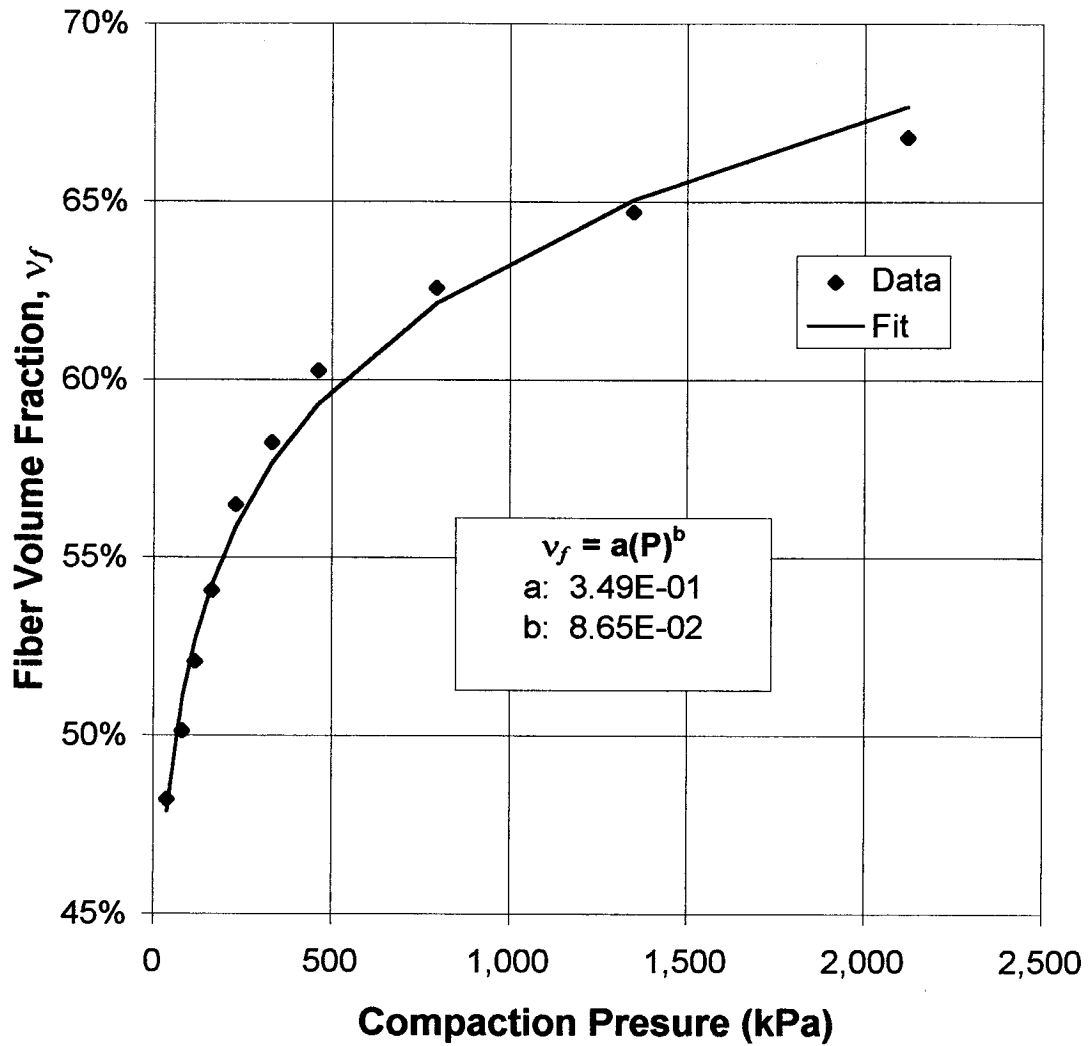
Figure 2-21    Fiber volume fraction versus compaction pressure for 54 ply multi-axial

warp knit preform.
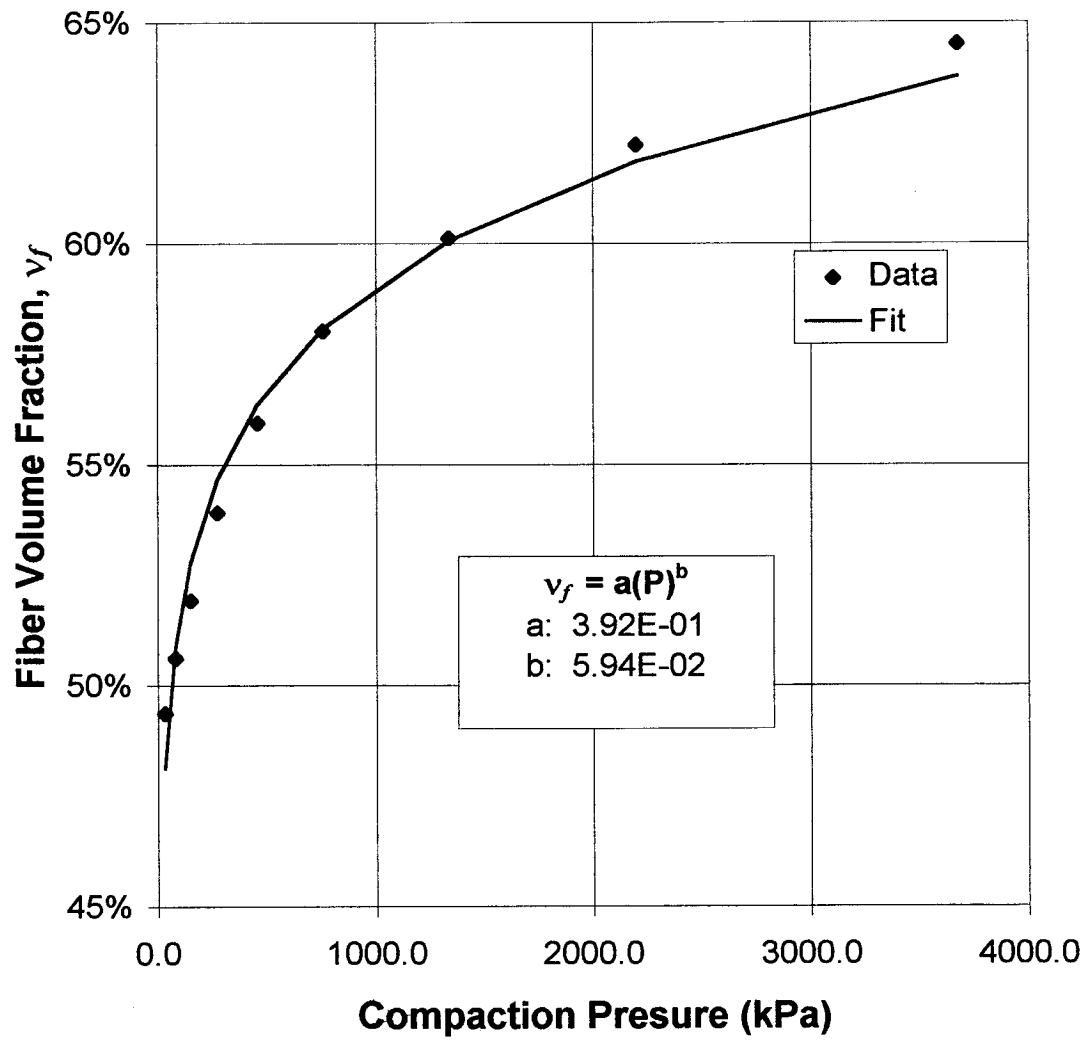
Figure 2-22    Fiber volume fraction versus compaction pressure for braided/woven
               stiffener.

## 2.6.6 Blade-stiffened preform permeability study

The permeabilities of three different regions (see Figure 2-23) of the blade-stiffened preform discussed in Section 2.6.5 were measured (see Figure 2-24 to Figure 2-26). Also, the 9-ply multi-axial warp knit subgroup permeabilities were measured to understand the effects of stitching (see Figure 2-27). The parameters for the permeability as a function of fiber volume fraction power-law regression model are presented in Table 2-4. Based on the results of the off-axis permeability tests discussed in Section 2.6.4, the assumption was made that the principal axes were parallel and normal to the stitching direction. The principal axes of the blade were not determined due to lack of material. Fixture C was used to measure in-plane permeabilities with the exception of the 9-ply multi-axial warp knit subgroup in-plane permeabilities, which were measured with Fixture B. Fixture A [9], a Type 4 (see section 2.2.5) fixture designed for 5.08 cm long and 5.08 cm wide samples, was used to measure transverse permeabilities.

Due to the limited availability of material, two concessions had to be made. First, 15.24 cm long and 15.24 cm wide samples were not available and second, samples were not tested across the entire fiber volume fraction range to allow reuse of sample material for tests spanning the fiber volume fraction range of interest (54-56%). Also, only a limited number of tests were possible, which did not allow for the standard deviation of the permeabilities to be calculated.

The assumption made when measuring the skin/flange section (see Figure 2-23) is that the material is comprised of homogeneous fabrics. Since the majority of the material in the skin/flange region is the warp-knit preform and due to the fact that the permeability of a heterogeneous material is driven by that of the higher permeability fabric, the assumption is valid. The warp-knit preform permeability is approximately an order of magnitude higher than that of the braided/woven material. The combined skin/flange material had an areal weight of 11,500 g/m$^2$.
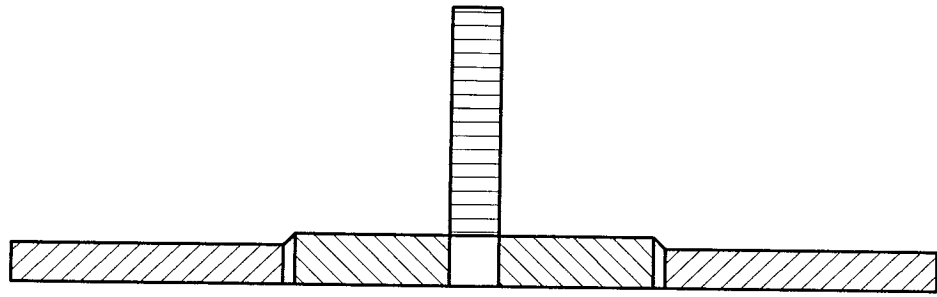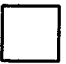
SKIN

SKIN/FLANGE

BLADE

NOT TESTED - PERMEABILITY
ASSUMED TO BE SIMILAR TO
SKIN REGION

Figure 2-23    Blade-stiffened preform.
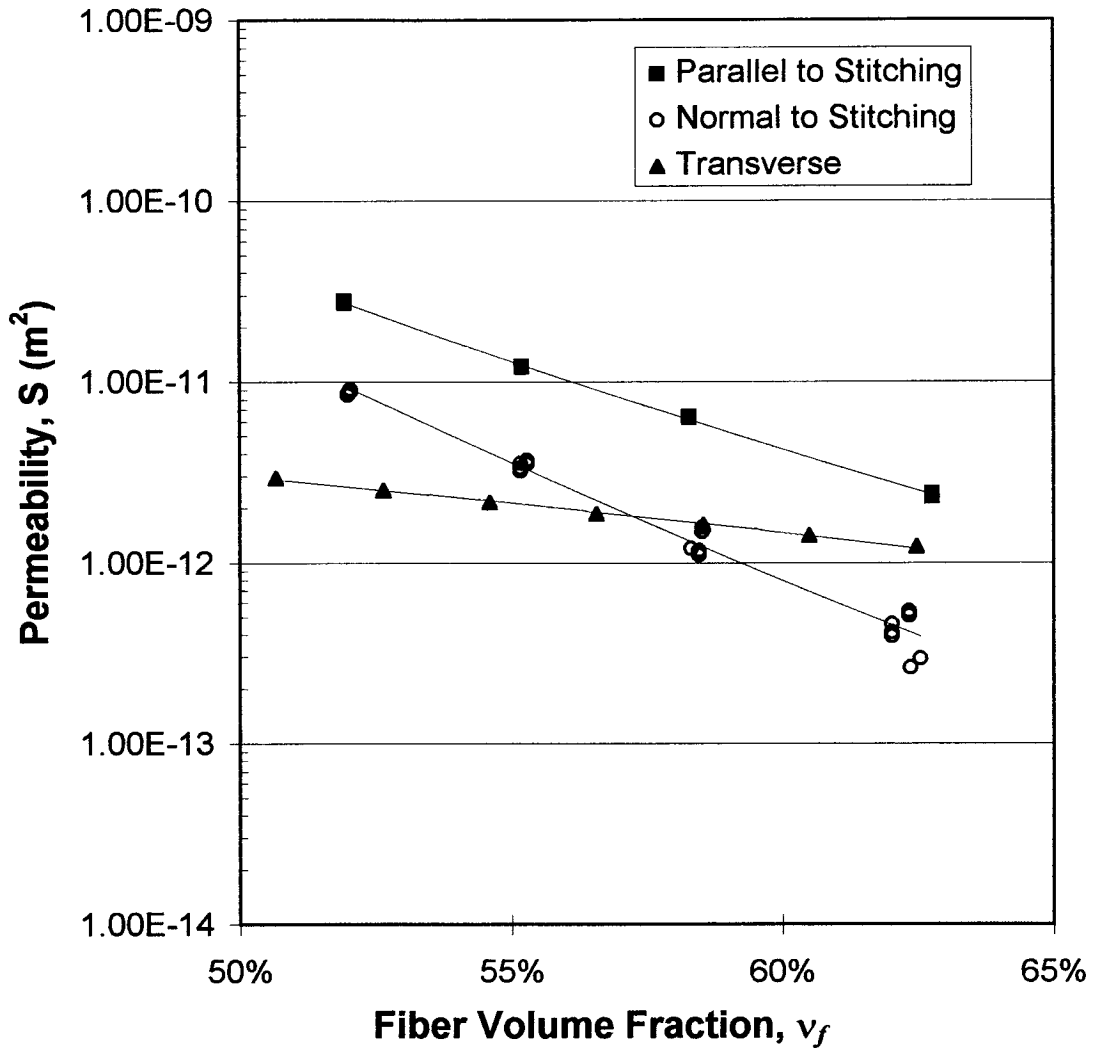
Figure 2-24    Permeability versus fiber volume fraction for 54 ply multi-axial warp knit
preform.
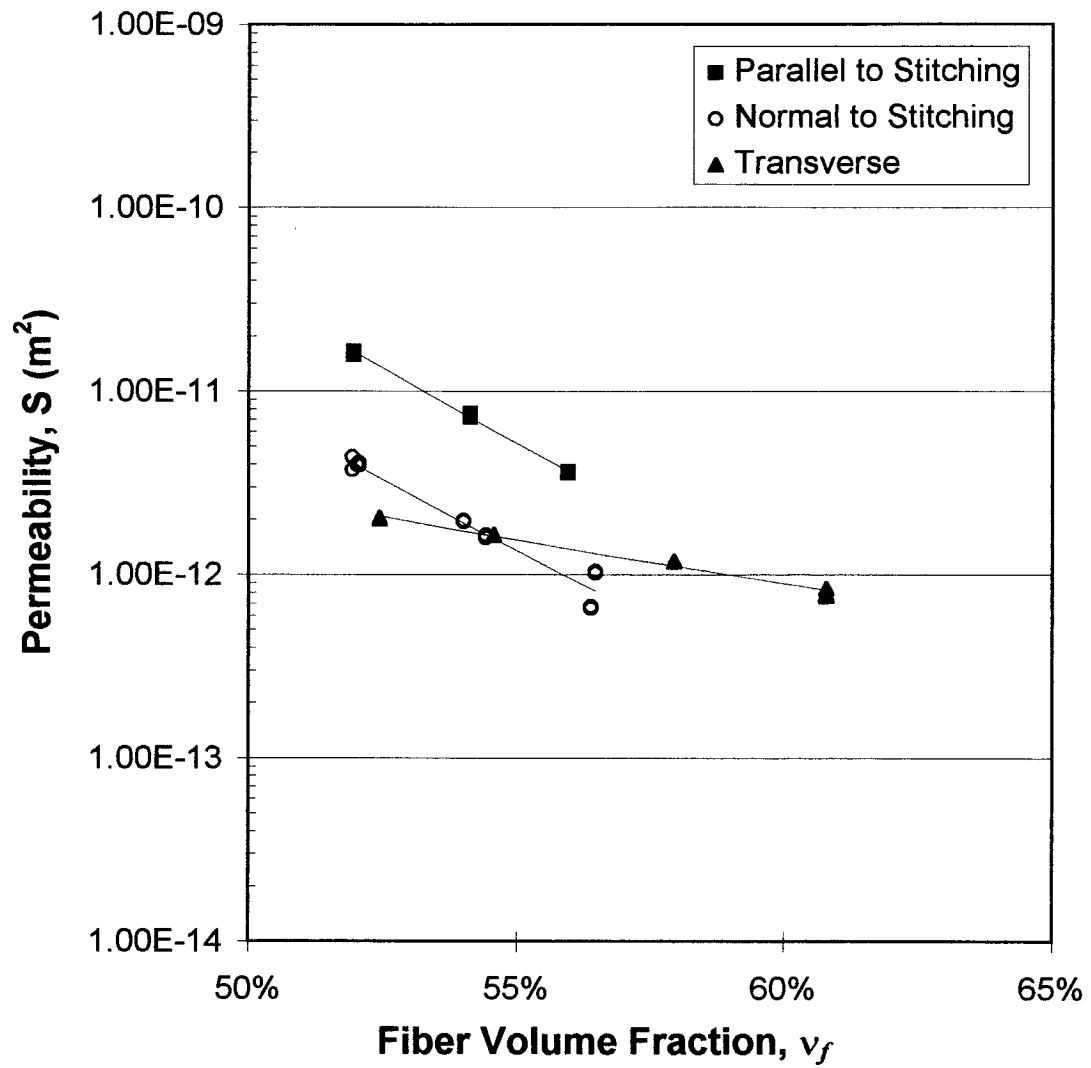
Figure 2-25    Permeability versus fiber volume fraction for 54 ply multi-axial warp knit
preform and braided/woven flange section.
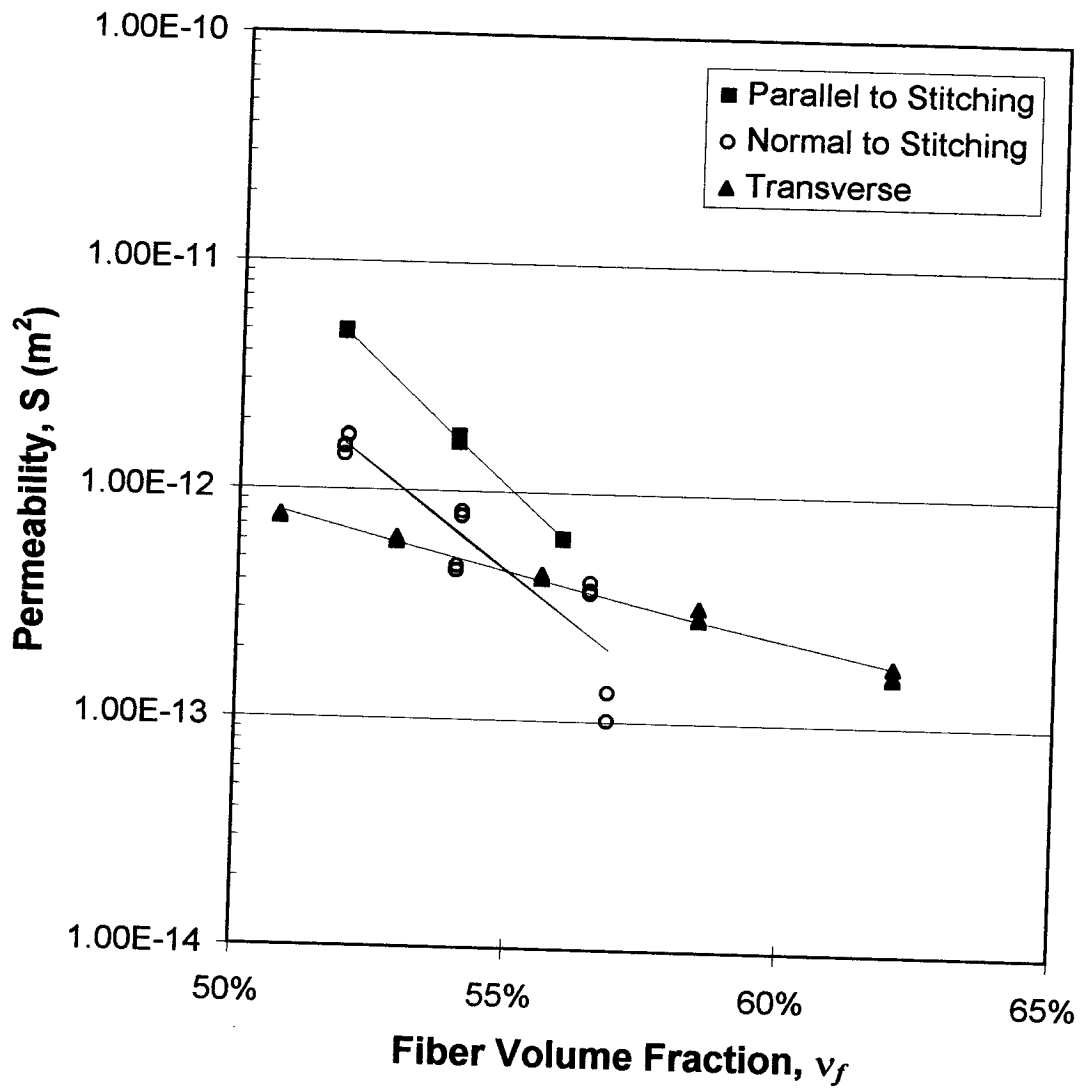
Figure 2-26    Permeability versus fiber volume fraction for braided/woven stiffener.
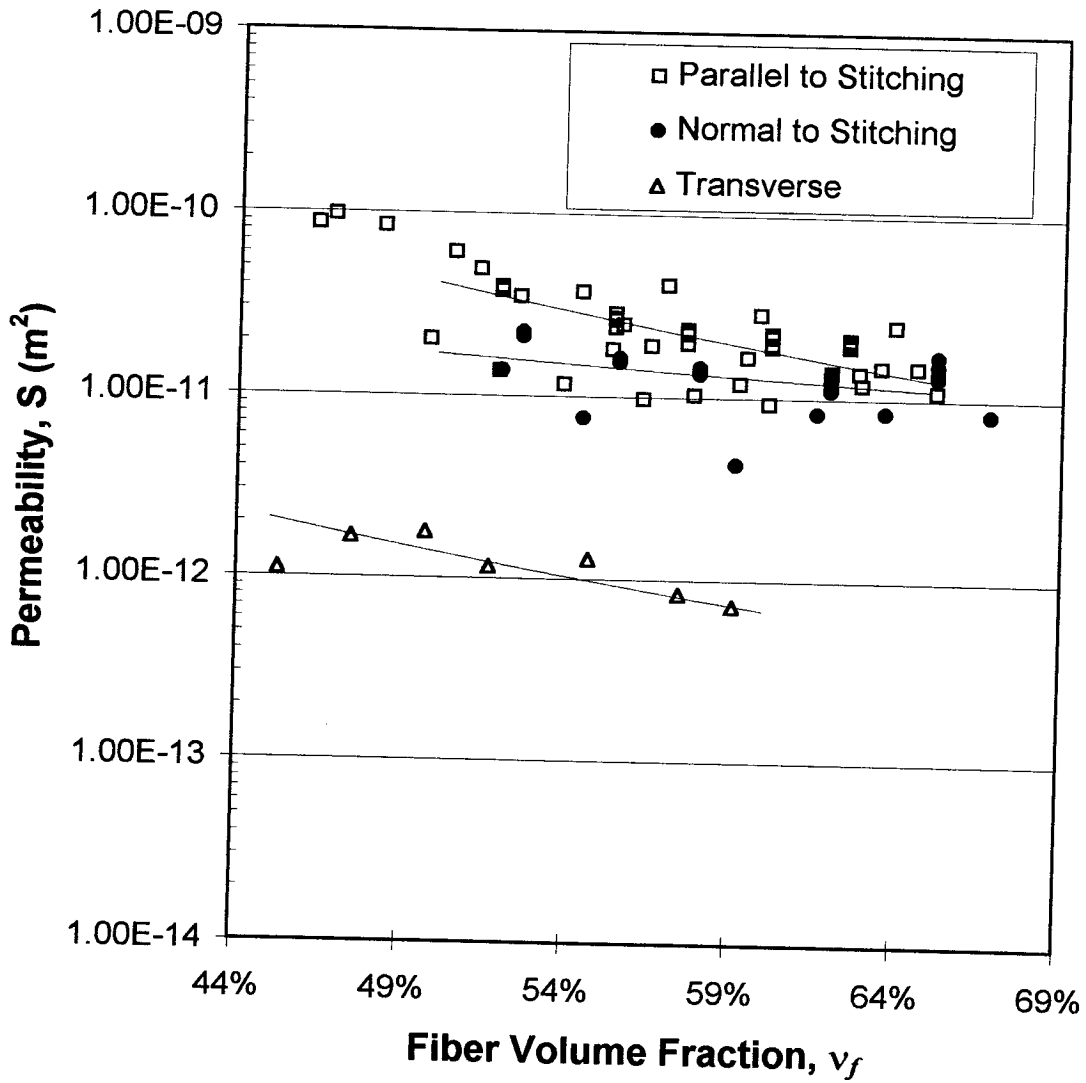
Figure 2-27    Permeability versus fiber volume fraction for 9-ply multi-axial warp knit subgroup.

Table 2-4    Parameters for permeability versus volume fraction power-law regression model, blade-stiffened preform sections and 9-ply multi-axial warp knit subgroup.

| Component | Direction | a (m^2) | b (unitless) | S at 55% volume fraction (m^2) |
|---|---|---|---|---|
| Skin | Parallel to stitching | 5.78E-15 | -1.29E+01 | 1.30E-11 |
| Skin | Normal to stitching | 1.25E-16 | -1.71E+01 | 3.50E-12 |
| Skin | Transverse | 1.72E-13 | -4.17E+00 | 2.08E-12 |
| Skin / flange | Parallel to stitching | 2.99E-17 | -2.02E+01 | 5.19E-12 |
| Skin / flange | Normal to stitching | 1.55E-17 | -1.90E+01 | 1.35E-12 |
| Skin / flange | Transverse | 3.76E-14 | -6.21E+00 | 1.54E-12 |
| Blade | Parallel to stitching | 8.21E-20 | -2.73E+01 | 1.00E-12 |
| Blade | Normal to stitching | 6.19E-19 | -2.25E+01 | 4.32E-13 |
| Blade | Transverse | 5.34E-15 | -7.39E+00 | 4.44E-13 |
| 9-ply subgroup | Parallel to stitching | 1.88E-12 | -4.46E+00 | 1.31E-13 |
| 9-ply subgroup | Normal to stitching | 5.79E-12 | -1.55E+00 | 1.46E-11 |
| 9-ply subgroup | Transverse | 9.71E-14 | -3.83E+00 | 9.59E-13 |

The results indicate that the permeability parallel to the stitching is always higher than the permeability normal to the stitching. This is believed to be the result of two factors. Hammond [8] states that in the warp knit subgroup the majority of the tows are in the 0° or ±45° direction (the stitching is in the 0° direction) and that the resistance to flow across a fiber tow is higher than the resistance to flow in the direction of the fiber tow. Also, the Kevlar stitching compresses the fabric locally, creating areas of higher fiber volume fraction in the stitching region. In the normal to stitching direction, the permeability would decrease more dramatically since the fluid must pass through these regions of high permeability. In the parallel to stitching direction, the permeability is driven by the lower areas of permeability on either side of the stitching.

A comparison of the permeabilities of the 9-ply subgroup and the 54-ply preform composed of the 9-ply subgroups stitched through-the-thickness shows that the normal to the stitching permeability decreases dramatically when the 9-ply subgroups are stitched together. This results supports the argument stated earlier that the permeability decreases since the fluid must pass through regions of high permeability caused by the stitching .

# 3. Three-Dimensional Flow Visualization and FEM Model Results

## 3.1 Introduction

The isothermal flow of resin through a blade-stiffened preform section was modeled and experiments were completed to verify the results.

## 3.2 Literature Review

The numerical methods which have been considered for flow modeling through porous media are boundary element, boundary-fitted finite difference, geometric, and finite element methods.

Um and Lee [18] used the boundary element technique to model the flow of silicone oil through fiberglass in a rectangular mold.

Coulter and Guceri [19] modeled the infiltration of an isotropic rectangular graphite preform using boundary fitted finite difference methods. Gauvin and Trochu [20] used a boundary-fitted finite difference technique to model the flow through porous media. They concluded that the method was not suitable for molds containing interior obstacles or dividing/merging flow fronts, and that computation time was prohibitive.

Boccard [21] developed a geometric method of determining vent locations and fill times for RTM molds. The method is limited to thin flat isotropic preforms of constant fiber volume fraction. The mold area is divided into subdomains around each resin inlet and vent locations are chosen based on the distance between the radius from the injection port and the perimeter. The fill time for each subdomain is determined by considering the flow as being partly radial and channel flow. A coefficient is determined geometrically for the percentage of the flow which is radial and that which is channel. Various mold shapes with and without inserts were considered. Experimental fill times were compared to calculated results, and the difference in fill times was normally less than ten percent.

Young et al. [22] used Finite Element/Control Volume methods to model a two-dimensional rectangular mold filling experiment, using both uniform and non-uniform random fiber mat placement and bi-directional fiber mats. The model under-predicted inlet pressure, and the discrepancies were thought to be due to porosity variation in the mats and variation in mold thickness due to mold deflection. The modeled flow front progression matched the experimental results well.

Frachia, Castro, and Tucker [23] implemented a Finite Element/Control Volume technique to model the two-dimensional flow for an automobile hood. The model was also matched to experimental results of flow through a rectangular mold with multiple inplane reinforcements.

Wu [24] completed a three-dimensional flow model using Finite Element/Control Volume approach. It was noted from experimental results that an overshoot in inlet pressure at the start of injection and an underestimation of inlet pressure towards the end of the cycle occurred. It was theorized that the cause was due to initial fiber consolidation resulting in flow channeling. Trochu et al. [25] used a non-conforming finite element method to simulate the two-dimensional flow through porous media. A simulation of the flow through a lawnmower hood was completed. The results were visualized by a separate menu-driven program interface VISUFLOT which simulates the flow-front results in real-time.

MacRae [1] compared his Finite Element/Control Volume results to Young's [22] rectangular 2-D flow experimental results. The flow front locations agreed quite well. The inlet pressure showed some variation, especially towards the end of infiltration. Sources of error were given as:

- inaccurate estimation of preform permeability
- assumed dimensions of inlet port size
- neglection of surface tension and capillary forces
- numerical approximations of geometry and fluid flow
- non-inclusion of no-slip boundaries

MacRae [1] also compared results to Coulter's [19] experimental results. In Coulter's results, the effect of non-slip boundary conditions was shown to have some effect. Also, inlet pressure calculations varied from experimental results.

Tests were run at Virginia Tech [1] for rectangular mold filling w/ E-glass and corn oil. It was found that predicted and experimental flow front profiles did not agree, and was theorized to be due to deflection of the upper mold plate. Corrections were made for the fiber volume fraction and permeability due to the deflection predicted by a Finite Element analysis, and results were shown to compare reasonably well.

Experimental flow results for a single-blade stiffener processed by the Resin Film Infusion technique were presented by MacRae [1]. An optimized processing cycle predicted by a Finite Element/Control Volume model was recommended after initial experimental trials resulted in incomplete wet-out. The incomplete wet-out was also verified by modeling with the final flow front position agreeing fairly well with experiment results.

## 3.3 Theory

### 3.3.1 Finite Element/Control Volume Method

For the modeling of the RTM mold filling process, the Finite Element/Control Volume model developed at Virginia Tech [1] was implemented. The advantages of the Finite Element/Control Volume technique as compared to other numerical techniques are:

- ability to handle complex geometries
- conservation of mass upheld
- flow front tracking
- numerical stability
- ease of handling multiple vents and gates

The Finite Element/Control Volume technique requires that the mold geometry be divided into elements. At each node, a control volume is constructed by subdividing the element into smaller volumes and summing the contribution of adjacent volumes at each node.

Element subdivision is carried out by breaking the element volume into smaller volumes connected at the centroid of each element. The Finite Element Method solves for the pressure gradients. The pressure gradients are entered into Darcy's Law, to solve for the velocity field and the flow rate into the control volume. With the flow rate information, the fill factor for the control volume can be updated. The time step for the next iteration is determined by calculating the estimated time step to fill each control volume and using the smallest value.

## 3.3.2 Flow Model

The following assumptions are made:

- the preform consists of heterogeneous anisotropic media
- resin is an incompressible Newtonian fluid
- the no-slip boundary condition is not enforced along boundaries of tooling due to limitations of the numerical technique.
- capillary and inertial effects are neglected

The general equation for continuity is as follows:

$$\frac{\partial \rho}{\partial t} + \left(\rho v_i\right)_{,i} = 0 \qquad i \rightarrow 1,2,3 \tag{3-1}$$

where $\rho$ is the density of resin and $v_i$ is the interstitial velocity. The superficial velocity ($q_i$) is written as follows, and is substituted into the continuity equation:

$$q_i = \frac{v_i}{\phi} \qquad i \rightarrow 1,2,3 \tag{3-2}$$

Incompressibility is assumed, and the continuity equation is simplified:

$$q_{i,i} = 0 \qquad i \rightarrow 1,2,3 \tag{3-3}$$

60

The momentum equation is replaced with Darcy's Law:

$$q_i = -\frac{1}{\eta} S_{ij} P_{,j} \qquad i,j \rightarrow 1,2,3 \qquad (3\text{-}4)$$

which is then substituted into the continuity equation.

$$\left(\frac{1}{\eta} S_{ij} P_{,j}\right)_{,i} = 0 \qquad i,j \rightarrow 1,2,3 \qquad (3\text{-}5)$$

Either a pressure or flow rate can be applied as a boundary condition at the resin inlet. The pressure at the inlet is specified as follows:

$$P_i = P_{applied} \qquad (3\text{-}6)$$

The flow rate at the inlet is specified as follows:

$$Q_n = n_i \left(\frac{1}{\eta} S_{ij} P_{,j}\right) \qquad i,j \rightarrow 1,2,3$$

$$(3\text{-}7)$$

$$n_i = \text{unit vector normal at surface of inlet}$$

The boundary condition at the mold wall requires that the flow rate normal to the mold wall is zero:

$$Q_n = n_i \left(\frac{1}{\eta} S_{ij} P_{,j}\right) = 0 \qquad i,j \rightarrow 1,2,3 \qquad (3\text{-}8)$$

The Finite Element formulation provides for eight-noded isoparametric brick elements and utilizes linear interpolation functions. The Finite Element formulation is described in further detail in reference [1].

## 3.4 Material and Equipment

### 3.4.1 Blade-stiffened preform

Blade-stiffened preforms have been fabricated at NASA-Langley Research Center. The preform consists of a 54 ply multi-axial warp knit preform and a braided/woven stiffener stitched to it. Details of the fabrication are described in Section 2.6.5. The approximate outer dimensions of the preform are shown in Figure 3-1.

### 3.4.2 Blade-stiffened preform flow fixture

An instrumented mold that would permit measurement of the resin flow patterns that develop during impregnation of the blade-stiffened preform was fabricated (see Figure 3-2). The mold was designed with the following objectives:

- Ability to change volume fractions of the components of the preform.
- Fluid injection that would result in a three-dimensional flow pattern.
- Insensitivity of flow front development to pressure transducers implemented to measure flow front position.
- Dimensional accuracy and stability, especially when preform compaction load is present.
- Creation of boundary conditions which can be accurately replicated in Finite Element model.

See Appendix B for machining prints and dimensions. The mold consists of three plates - a lower mold plate and a left and right mold plate. The interior faces of the mold conform to the dimensions of the preform and are ground for dimensional accuracy. Ground
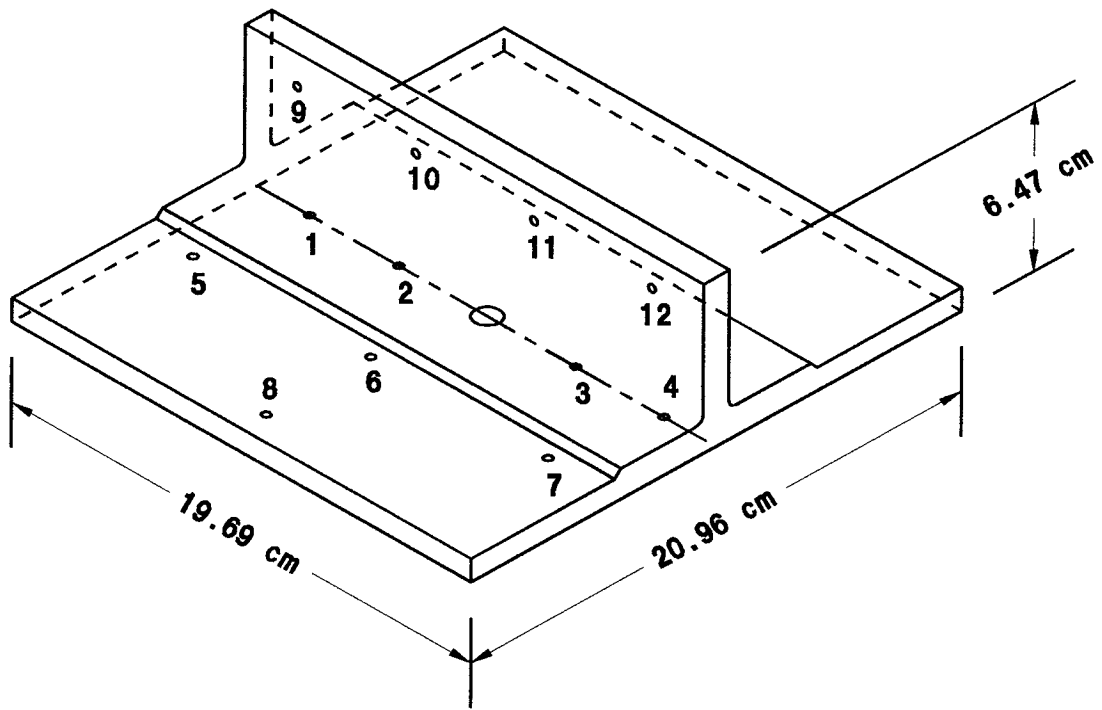
Figure 3-1    Blade-stiffened preform - approximate dimensions and pressure transducer locations.
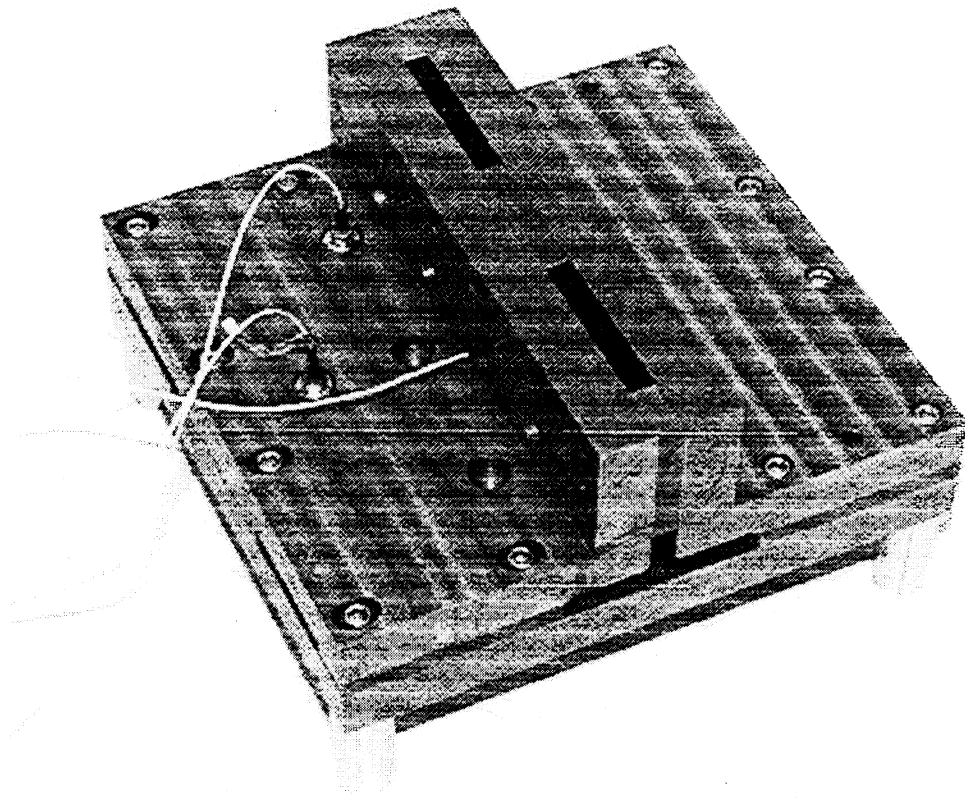
Figure 3-2    Blade-stiffened preform flow fixture.

spacers were implemented to allow for changes in fiber volume fraction. Steel was chosen as a structural material instead of materials such as plexiglass to meet the requirement of dimensional stability under preform compaction loads. The inlet of the mold was located at the center of the lower mold plate to allow for a three-dimensional flow pattern to develop.

The flow front position was measured by as many as six Entran EPX series pressure transducers. The sensor locations are shown Figure 3-1. The tip of each transducer is slightly offset from the interior mold face so that the transducer reading is not affected by the compaction load of the preform. The diameter of the transducer tip is 3.5 mm, which minimizes the effect of the transducer on the flow front.

The edges of the preform with the exception of the upper edge of the stiffener were potted with a two-part polyurethane (Hexcel Uralite 3138 Part A & B) to prevent flow through the edge of the preform (see Figure 2-20). See Appendix C for a description of the sample preparation method.

# 3.5 Model Processing

## 3.5.1 Pre-processing

PATRAN (PDA Engineering) was utilized to construct the geometry, discretize the geometry into elements, and apply boundary conditions and material properties. A PATRAN neutral file is output which contains all of the model data for the Finite Element model developed at Virginia Tech [1]. An example of a PATRAN session file used to construct the finite element mesh is listed Appendix D.

The model was run on IBM RS-6000 (SP2) workstations at NASA-Langley Research Center. The computing time for a 2060 element model was 7443 CPU seconds.

The finite element mesh (see Figure 3-3) generated was a quarter model of the entire preform and contained 2060 elements. There were two convergence issues of concern - (1) the overall element size to allow for accurate calculation of mold-filling time and (2) refinement of the mesh near the inlet where the high pressure gradients occur to calculate

accurate mold pressures. The creation of a highly refined mesh to confirm the convergence of the results was not pursued due to the CPU time which would have been necessary. Instead, the two convergence issues were treated separately. To ensure that the mesh near the inlet was refined enough, a small model of the inlet region was created. Once the level of refinement of the inlet region was confirmed to be sufficient by convergence of the pressure gradients, the overall element size for the entire quarter model was refined to confirm that correct mold-filling times were produced. The result is the finite element mesh depicted in Figure 3-3. The boundary conditions specified are zero flow rate normal to all surfaces except the inlet, and constant flow rate at the inlet. The initial condition specified is zero pressure at all nodes except for the nodes on the surface of the inlet where the pressure is not specified due to the constant flow rate condition.

### 3.5.2 Post-processing

PATRAN was utilized to input PATRAN formatted result files which contain nodal results of fill times, pressure values and flow front velocities at discrete time intervals. These results were post-processed to generate three-dimensional contour plots.

## 3.6 Experimental and FEM Results

### 3.6.1 Flat Panel Test Case

The flow of resin through a flat panel was modeled with geometry and input parameters of the same order of magnitude as those encountered in the blade-stiffened preform simulation. The panel had dimensions of 10.0 cm x 10.0 cm x 1.0 cm, and the mesh generated was 10 x 10 x 1 elements, respectively. The boundary conditions enforced included a 1.0 cm x 10 cm line source resin inlet with a constant resin flow rate, a pressure sink at the opposite 1.0 cm x 10.0 cm surface, and zero flow rate normal to all other surfaces. With these prescribed boundary conditions, the flow front becomes one-
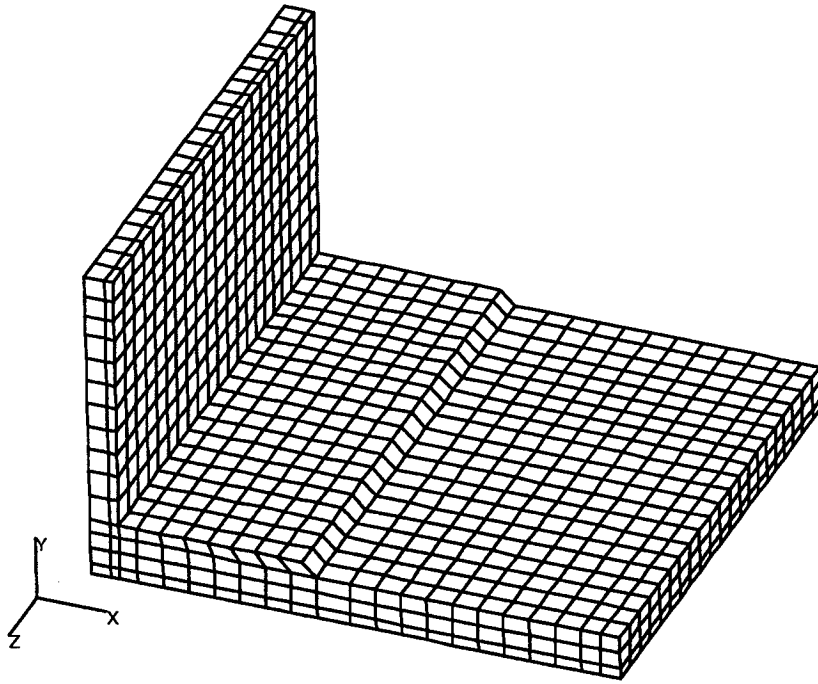
Figure 3-3    Quarter-model finite element mesh - blade-stiffened preform.

dimensional and the inlet pressure can be solved by a one-dimensional mold filling analysis:

$$P_{inlet} = \frac{t\, q^2\, \eta}{S\, \phi}$$

(3-9)

The model parameters assigned are listed in Table 3-1:

Table 3-1    Model parameters, flat panel.

| Variable | Quantity | Units |
|---|---|---|
| viscosity | 0.10 | Pa-sec |
| porosity | 0.45 | |
| inlet flow rate | 1.0 | cc/min |
| permeability | 1.0E-11 | $m^2$ |

The fill time and the inlet pressure at complete fill were identical to those calculated with a one-dimensional mold filling analysis, and the results were 2700 seconds and 16.67 kPa, respectively.

## 3.6.2 Blade-stiffened preform flow front test results

### 3.6.2.1 Test Description

A total of three flow front tests were completed. The blade-stiffened preform was impregnated with corn oil at a constant inlet flow rate of 3 cc/min. The flow rate was determined by initial test results to be approximately the highest flow rate possible without compression of the preform at the inlet due to high inlet pressures. Corn oil was used as a test fluid and had a viscosity of 0.0581 Pa-sec at room temperature. The spacers between

68

the lower mold plate and the upper mold plates were 0.899 cm thick and the spacers between the upper mold plates were 1.107 cm thick in order to maintain a fiber volume fraction of 55.0% across the entire preform. All edges were sealed with polyurethane except for the top edge of the blade, which was left open to allow air to escape from the mold. The four corners of the base of the preform were vented by placing a small diameter wire under the polyurethane seal until fluid was visible in order to allow air to escape.

The inlet pressure was monitored with an Omega pressure transducer, 0-100 psi. As many as six Entran transducers with pressure ranges of 0-50, 0-100, and 0-250 psi were used to monitor the flow front position. Because of the low pressures present in the mold other than at the inlet throughout the test, the pressure readings were not accurate enough to predict mold pressures and could only be used to predict the time at which the flow front passes over the transducer. Also, since there were more pressure taps (see Figure 3-1) than pressure transducers, the transducers were initially placed at pressure taps that the flow front would reach first. After the flow front passed these pressure taps, the pump was stopped and the transducers were moved to the next series of pressure taps, replugging the initial pressure taps. This was repeated until the flow front had been measured at all pressure taps. Data was sampled every two seconds during the duration of the tests.

### 3.6.2.2 Test results and FEM comparison

The permeabilities input to the model are those presented in Table 2-4. The FEM flow front visualization results are presented in Figure 3-4, and depicts the location of the flow front at select time intervals from t = 0 to complete mold fill at 4323 seconds. The pressure distribution data (Pascals) is presented in Figure 3-5 at a selected time of 3242 seconds. The inlet pressure was underestimated by an average of approximately 50% (see Figure 3-6).
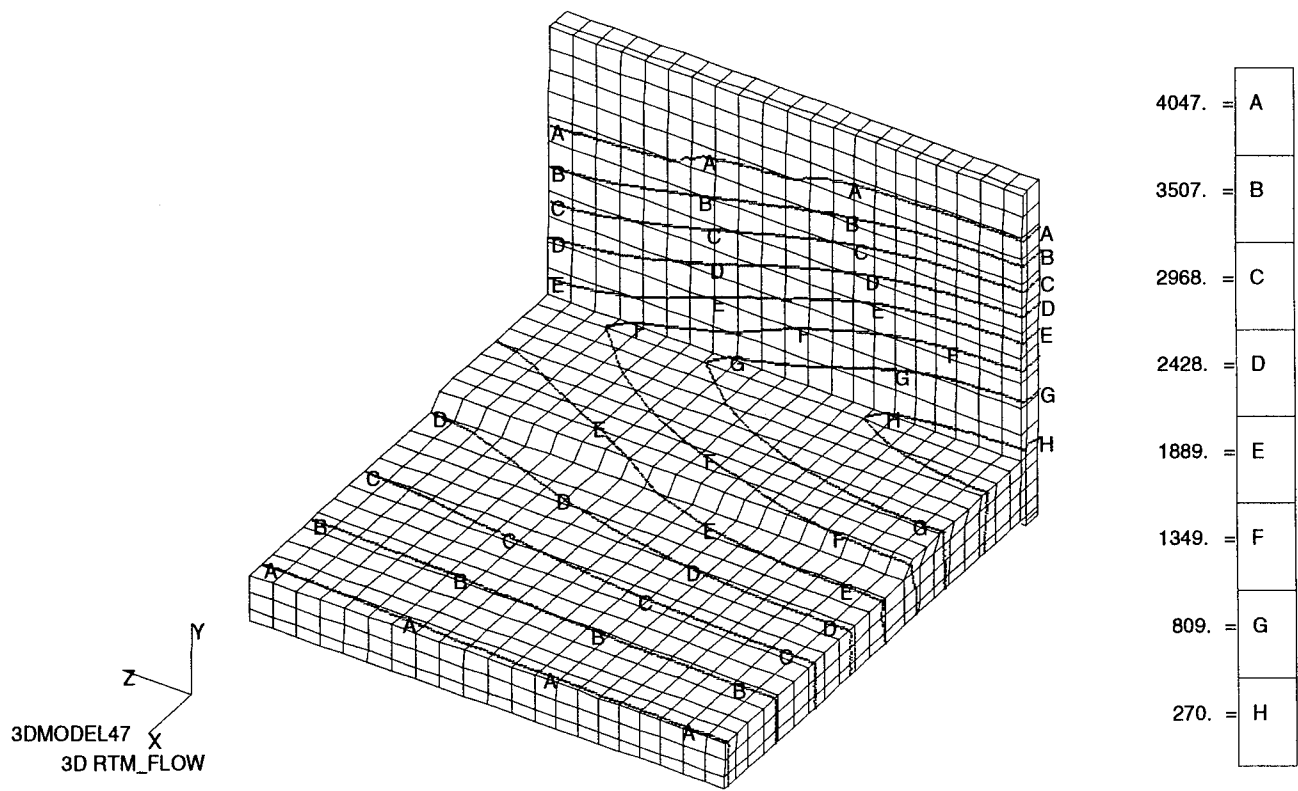
Figure 3-4     Flow front progression at selected time intervals (seconds), blade-stiffened preform.

| | |
|---|---|
| 66925. = | A |
| 20000. = | B |
| 17143. = | C |
| 14286. = | D |
| 11428. = | E |
| 8571. = | F |
| 5714. = | G |
| 2857. = | H |

3DMODEL47
3D RTM FLOW
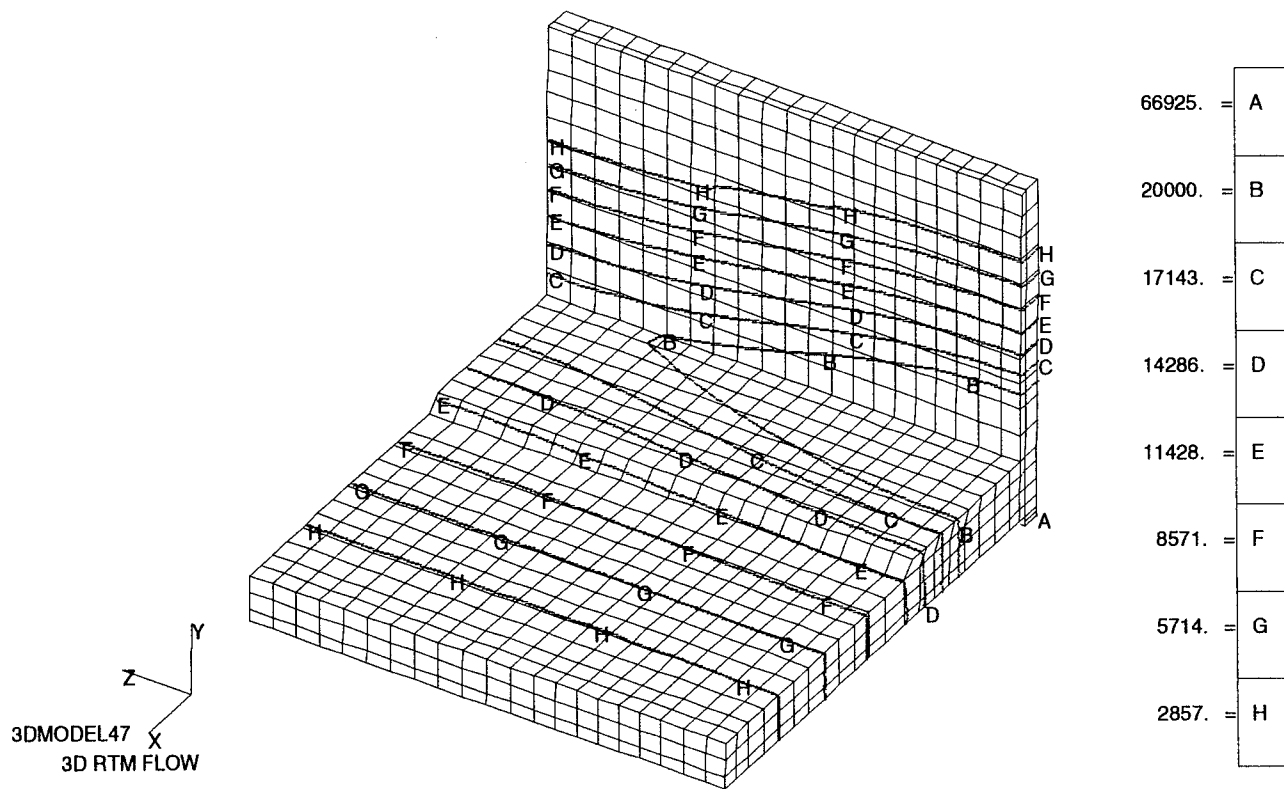
Figure 3-5    Pressure distribution (Pa) at 3242 seconds, blade-stiffened preform.
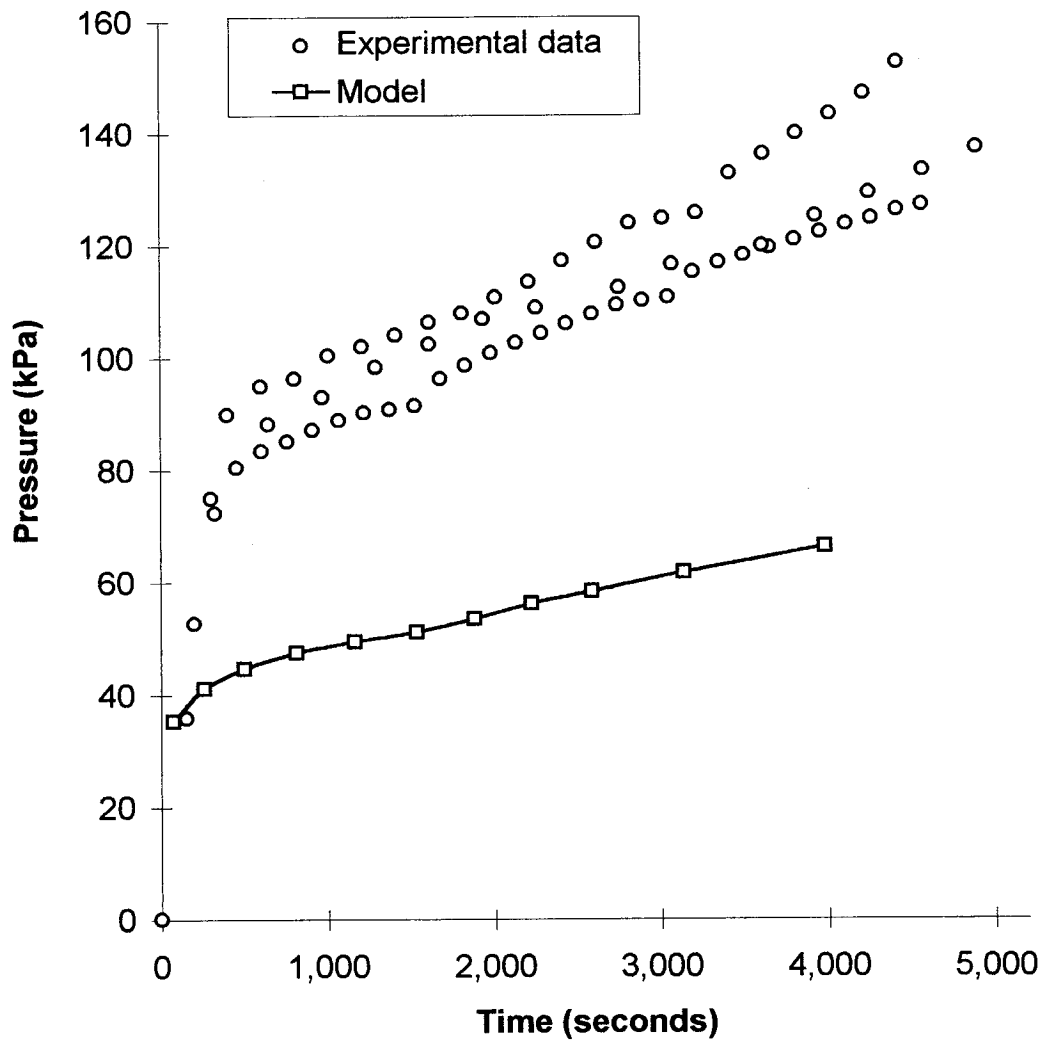
Figure 3-6    Experimental and model predicted inlet pressure, blade-stiffened preform.

Figure 3-7 presents the model predicted versus experimentally determined times at which the flow front passes the pressure tap locations. Figure 3-8 presents the percent difference in times between the model predicted times and the experimentally determined times for the flow front to pass the pressure tap locations. The experimentally measured flow front reached pressure tap locations 2/3 and 1/4 located on the bottom of the skin much more slowly than predicted by the model. The same results were noted for pressure tap locations 5-8 located on the top of the skin. The pressure tap locations 9-12 located on the blade wet out more quickly than predicted by the model.

Possible reasons for the mismatch in results are as follows:

1. Incorrect permeability data input to the model.

2. Assumption that the fiber volume fraction of the skin directly under the blade is maintained at 55%. This region is not supported on both faces by a mold surface, and can be affected by the mold bolting procedure.

3. Non-homogeneity of the region near the bottom of the blade and above the skin. The blade and blade flange region are manufactured as one item. The blade flanges are formed by bending the two halves of the preform blade flanges 90° and stitching the flange to the skin. Continuous fiber rovings are placed in the gap under the blade before it is stitched to the skin. This is not accounted for in the model.

If the error is a result of incorrect permeability data, the results indicate that on the average the permeability values input to the model were too high. If all of the permeability values were increased by approximately 100%, the inlet pressures would match well. This would not account for the differences noted in the flow front progression. In an attempt to explain the differences in the flow front location, a parametric study of the effects of changing permeabilities in the different regions was undertaken. Since it was noted that the flow front was fairly uniform across the thickness of the blade region, the transverse permeability of the blade region was determined not to be a factor and was not included in the parametric study.
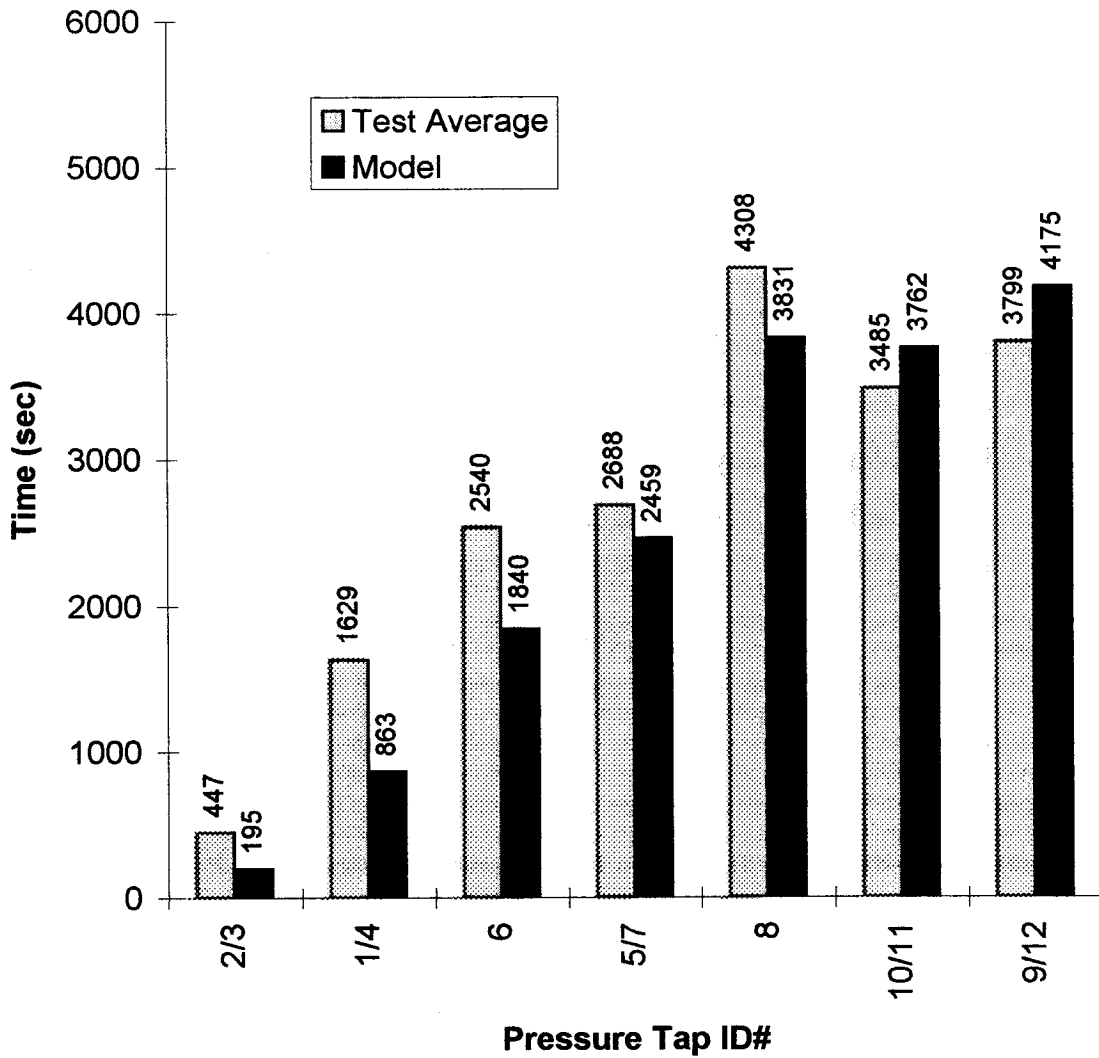
Figure 3-7    Experimental and model predicted wet-out times (seconds) at pressure tap

locations (see Figure 3-1), blade-stiffened preform.

Figure 3-8    Percent difference of wet-out times    $(t = 100(t_{model} - t_{experimental})/t_{experimental})$ at pressure tap locations (see Figure 3-1), blade-stiffened preform.

The order of magnitude of the variation used in the parametric study was determined from the standard deviation of the experimental error calculated from the E-glass permeability tests (see Section 2.6.1). The assumption made is that the standard deviation of the permeability due to variability of the material does not vary from E-glass to the components of the blade-stiffened preform. The revised permeabilities used in the study were equal to the measured permeabilities minus three standard deviations, which means that there is a 99% likelihood of the actual permeability falling within that range. The revised permeabilities were approximately 25% of the original estimated value.

The results of the parametric study (see Figure 3-9 to Figure 3-14) show that the reduction of any one of the permeability values to 25% of its original value is not sufficient to alter the inlet pressure to the level measured experimentally. The percent difference in wet-out times was reduced by the greatest amount when the skin permeability parallel to the stitching was reduced by 25% (see Figure 3-12). The average error in the normalized time for the flow front to reach the pressure tap locations was reduced from 24% to 12%. In all other cases, the maximum reduction in error was 5%.

The magnitude of the inlet pressure was increased to the greatest degree when the following permeabilities were decreased:

- parallel to stitching, skin (see Figure 3-9)
- normal to stitching, skin (see Figure 3-9)
- normal to stitching, skin/blade flange (see Figure 3-10)

It is also noted that the error in wet-out time for sensor 6 located on the top of the base was affected most by a reduction in the skin/flange permeability normal to the stitching, as the error in normalized wet-out time was reduced from 28% to 1% (see Figure 3-13).

In order to test the hypothesis that the fiber volume fraction of the skin directly under the blade is not 55%, the permeabilities in that region were decreased to correspond to fiber volume fractions of 58, 60, and 62%. The proposed reason for the discrepancy in fiber volume fraction is that the fiber volume fraction could possibly be affected by the bolting procedure. If the two upper mold plates are bolted tightly with the blade positioned between the plates prior to attaching the upper mold plates to the lower mold
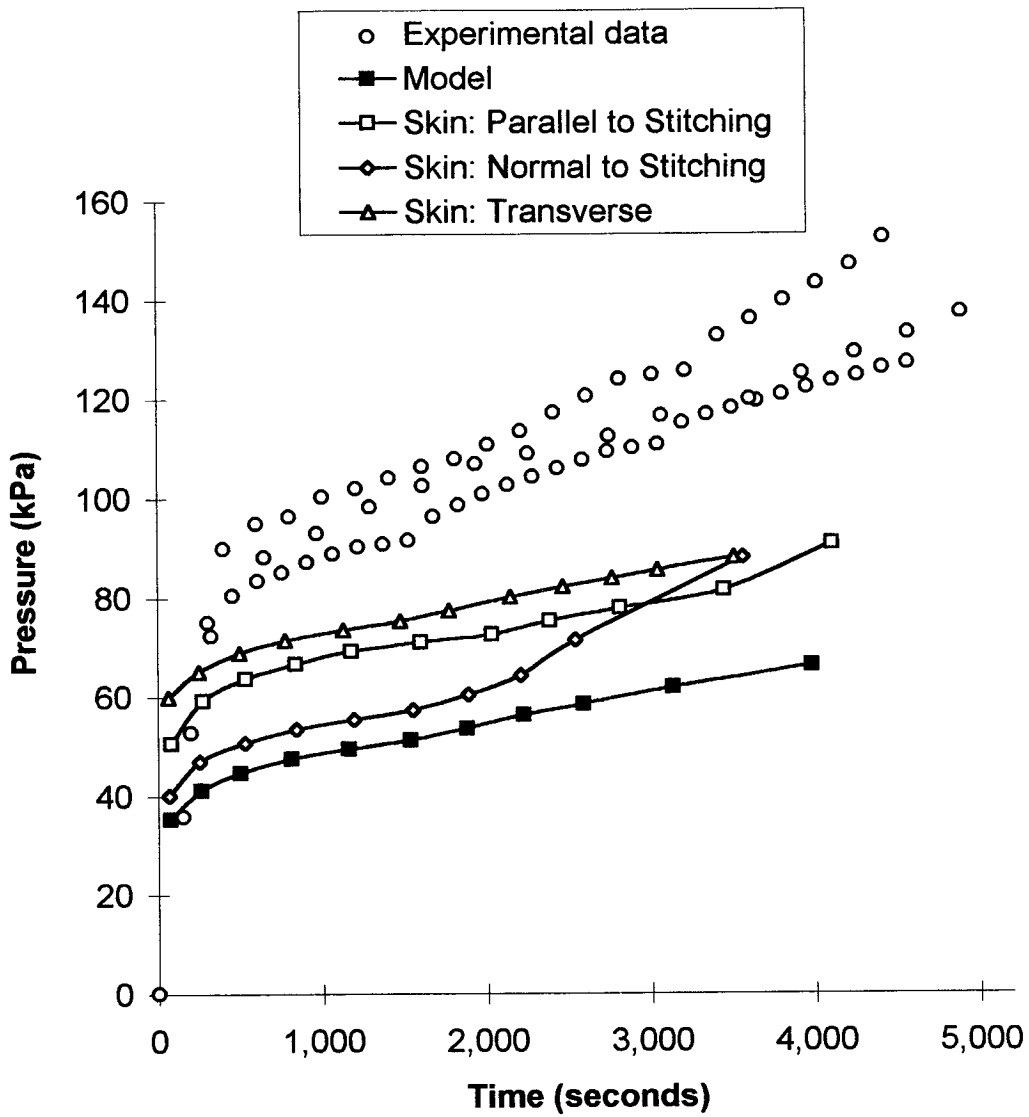
Figure 3-9    Inlet pressure, blade-stiffened preform. Experimental data and FEM results of model utilizing original permeability data and revised models with skin permeabilities reduced to 25% of original value in the direction stated.
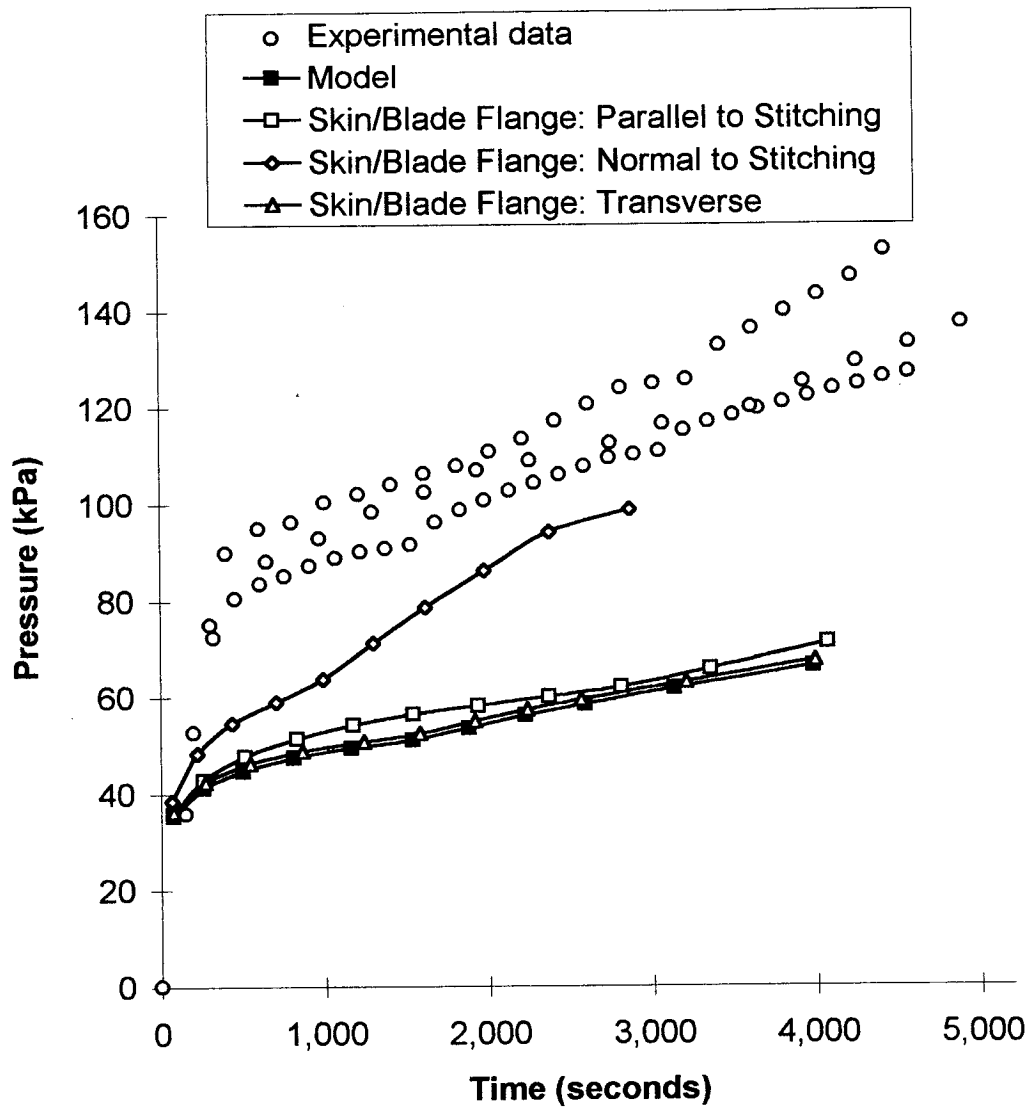
Figure 3-10    Inlet pressure, blade-stiffened preform. Experimental data and FEM results
of model utilizing original permeability data and revised models with
skin/blade flange permeabilities reduced to 25% of original value in the
direction stated.
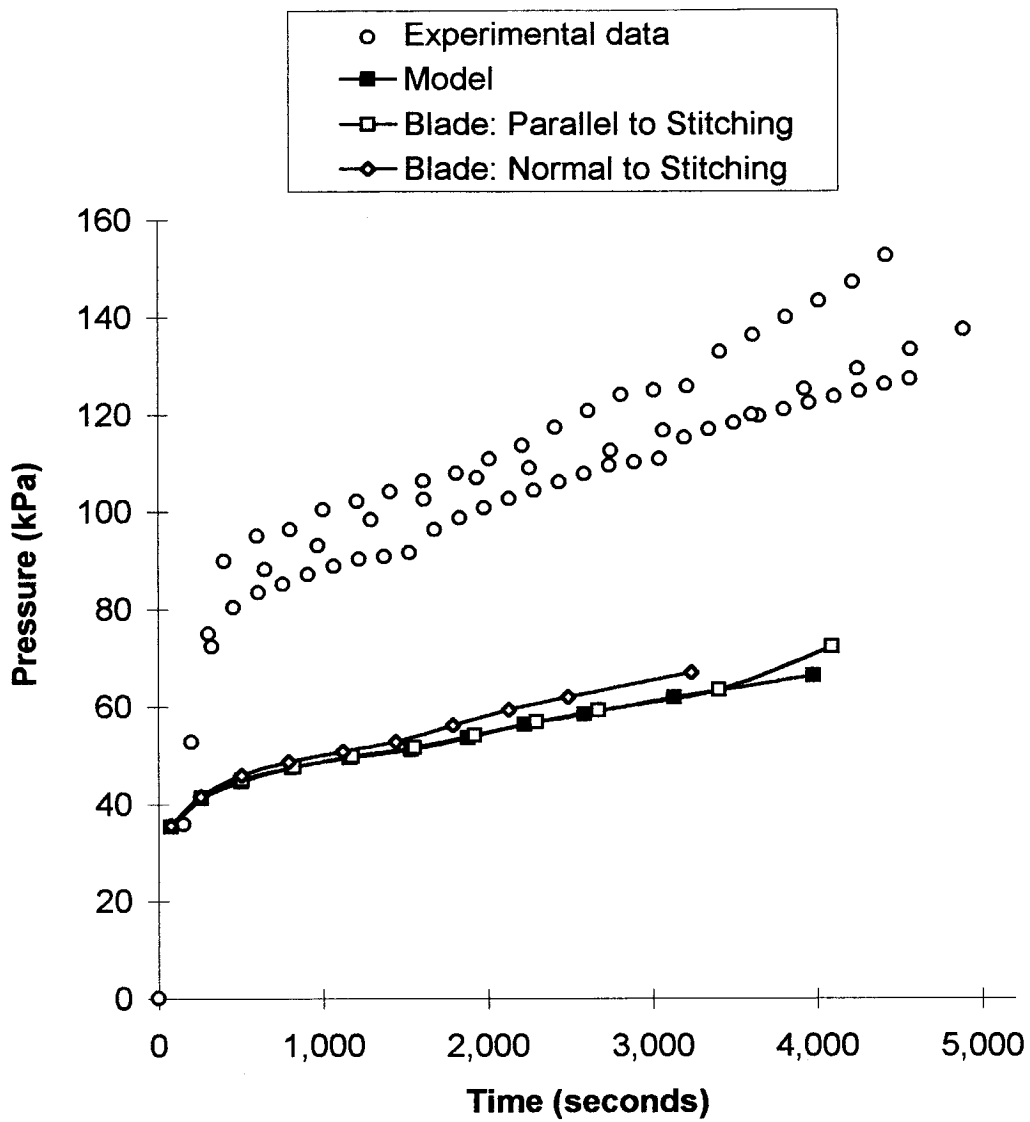
Figure 3-11    Inlet pressure, blade-stiffened preform.  Experimental data and FEM results

of model utilizing original permeability data and revised models with blade

permeabilities reduced to 25% of original value in the direction stated.
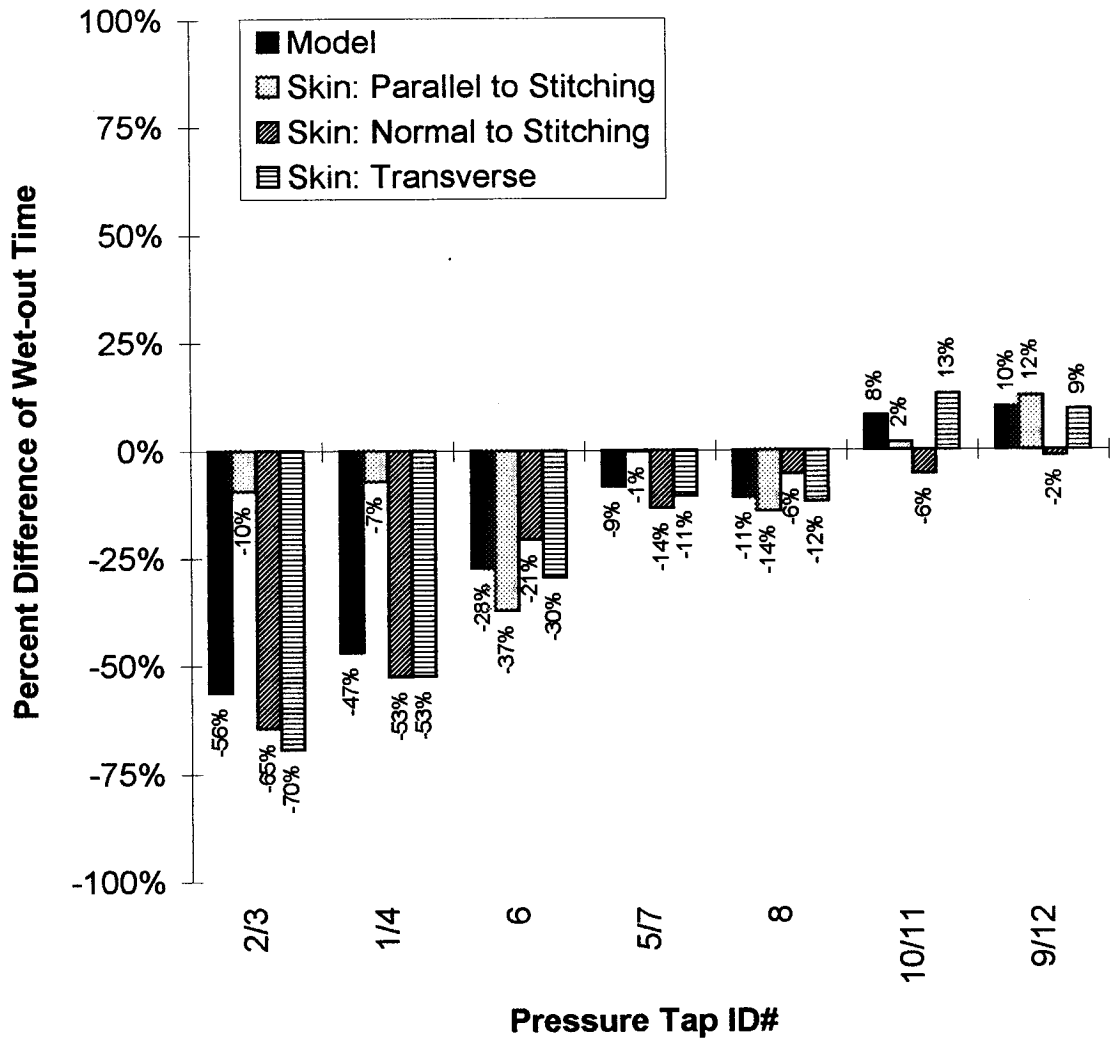
Figure 3-12    Percent difference of wet-out times    $(t = 100(t_{model} - t_{experimental})/t_{experimental})$ at

pressure tap locations (see Figure 3-1), blade-stiffened preform flow

fixture. FEM results comparison of model utilizing original permeability

data and revised models with skin permeabilities reduced to 25% of

original value in the direction stated.
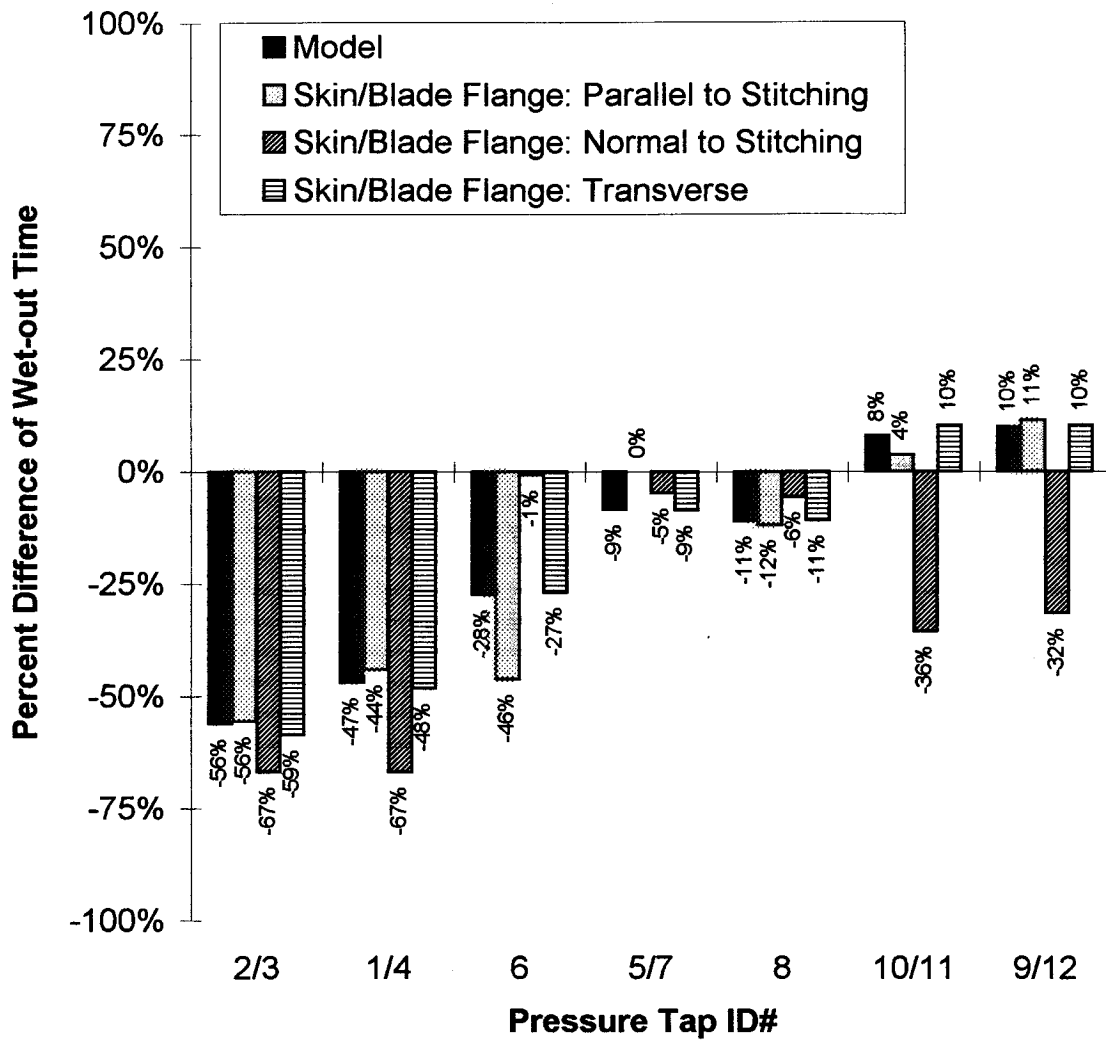
Figure 3-13    Percent difference of wet-out times    $(t = 100(t_{model} - t_{experimental})/t_{experimental})$ at

pressure tap locations (see Figure 3-1), blade-stiffened preform flow

fixture.  FEM results comparison of model utilizing original permeability

data and revised models with skin/blade flange permeabilities reduced to

25% of original value in the direction stated.
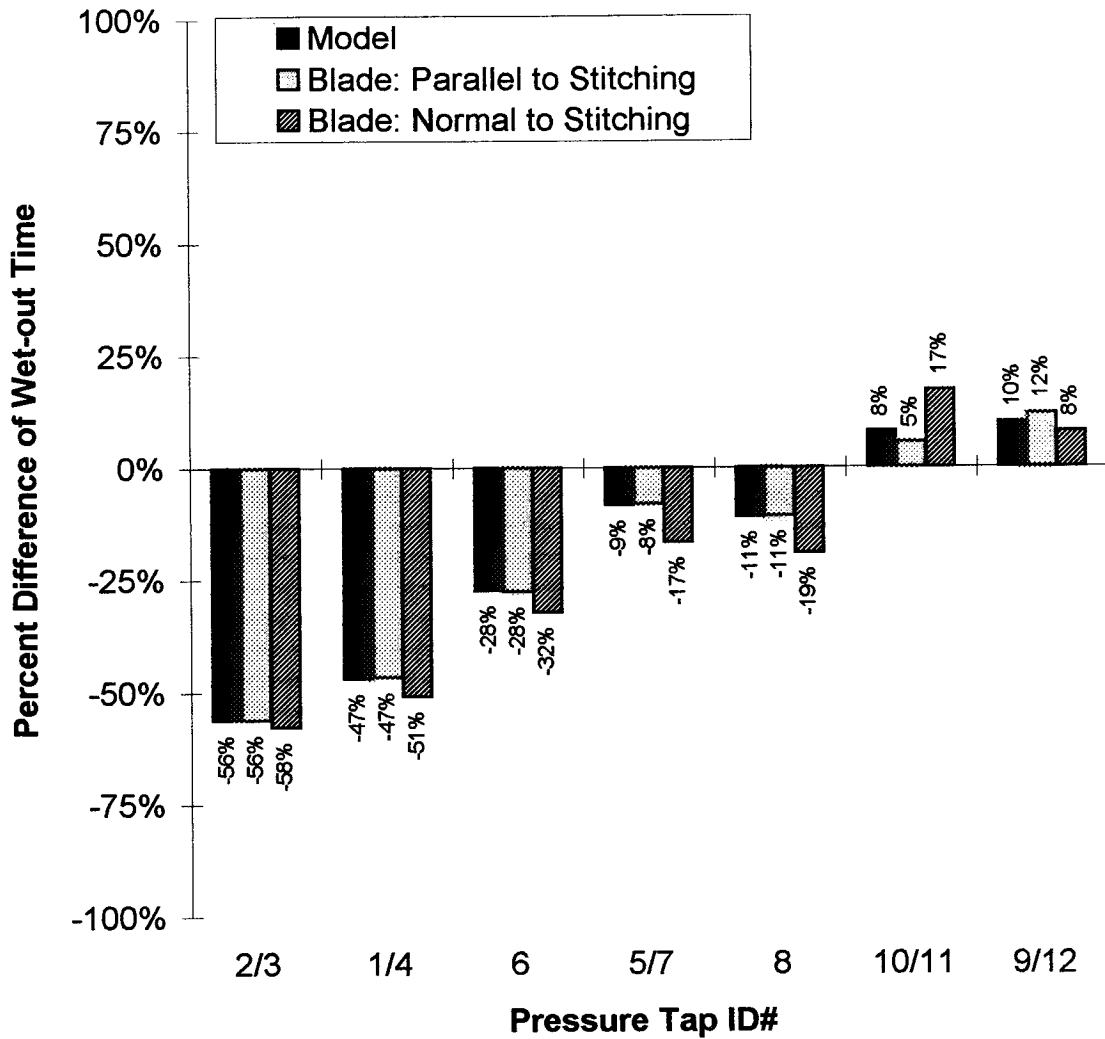
Figure 3-14    Percent difference of wet-out times   $(t = 100(t_{model} - t_{experimental})/t_{experimental})$ at
pressure tap locations (see Figure 3-1), blade-stiffened preform flow
fixture. FEM results comparison of model utilizing original permeability
data and revised models with blade permeabilities reduced to 25% of
original value in the direction stated.

C-2     r

plate, the friction between the blade and the fixture will restrict the blade from attaining its desired position between the two upper mold plates and further compress the skin. This would cause higher inlet pressures and slower flow front progression along the bottom surface of the skin along the centerline parallel to the stitching. These occurrences are substantiated by the original experimental data and model results (see Figure 3-6 to Figure 3-8).

The results of the change in fiber volume fraction of the skin directly under the blade were favorable. The average percent difference in wet-out times (Figure 3-15) was reduced to 12% when the fiber volume fraction was increased to 62%. The calculated inlet pressure curve (Figure 3-16) for a fiber volume fraction of 62% was approximately the same order of magnitude as the experimentally measured pressure curve. The pressure curve predicted by the revised model initially overpredicts the inlet pressure, followed by a region which approximates the experimental pressure curve fairly well.

The difficulties associated with modeling the heterogeneities of the region under the blade and above the skin are that the mass, fiber volume fraction, permeability, and distribution of the continuous rovings are unknown. It is noted from the model that the velocity profile in this region is primarily in the transverse direction to the fibers. Since the height of the region is negligible, the pressure drop across the region would be negligible if the transverse permeability is of the same relative order of magnitude or lower than that of the blade. Only if the transverse permeability was of a much lower order of magnitude or if the permeability parallel to the fibers was much higher creating a relatively resistance-free channel under the blade would the results be affected. Since the original model predicts correctly the percent difference in wet-out time (see Figure 3-8) between the pressure taps near the center of the blade (10/11) and the pressure taps near the edge of the blade (9/12), the permeability parallel to the direction of the continuous roving is assumed to not be high enough to create such an effect.
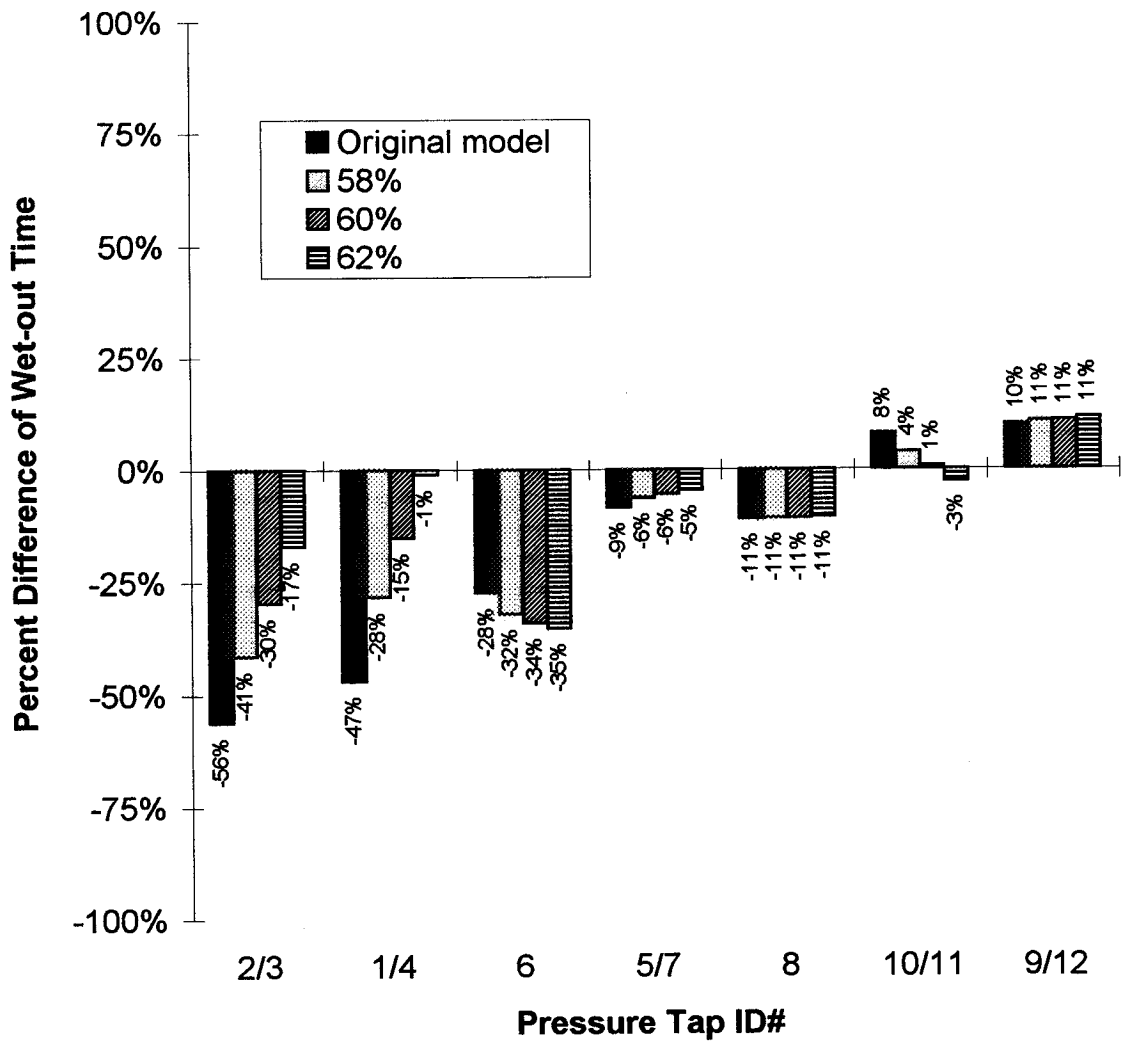
Figure 3-15    Percent difference of wet-out times    $(t = 100(t_{model} - t_{experimental})/t_{experimental})$ at
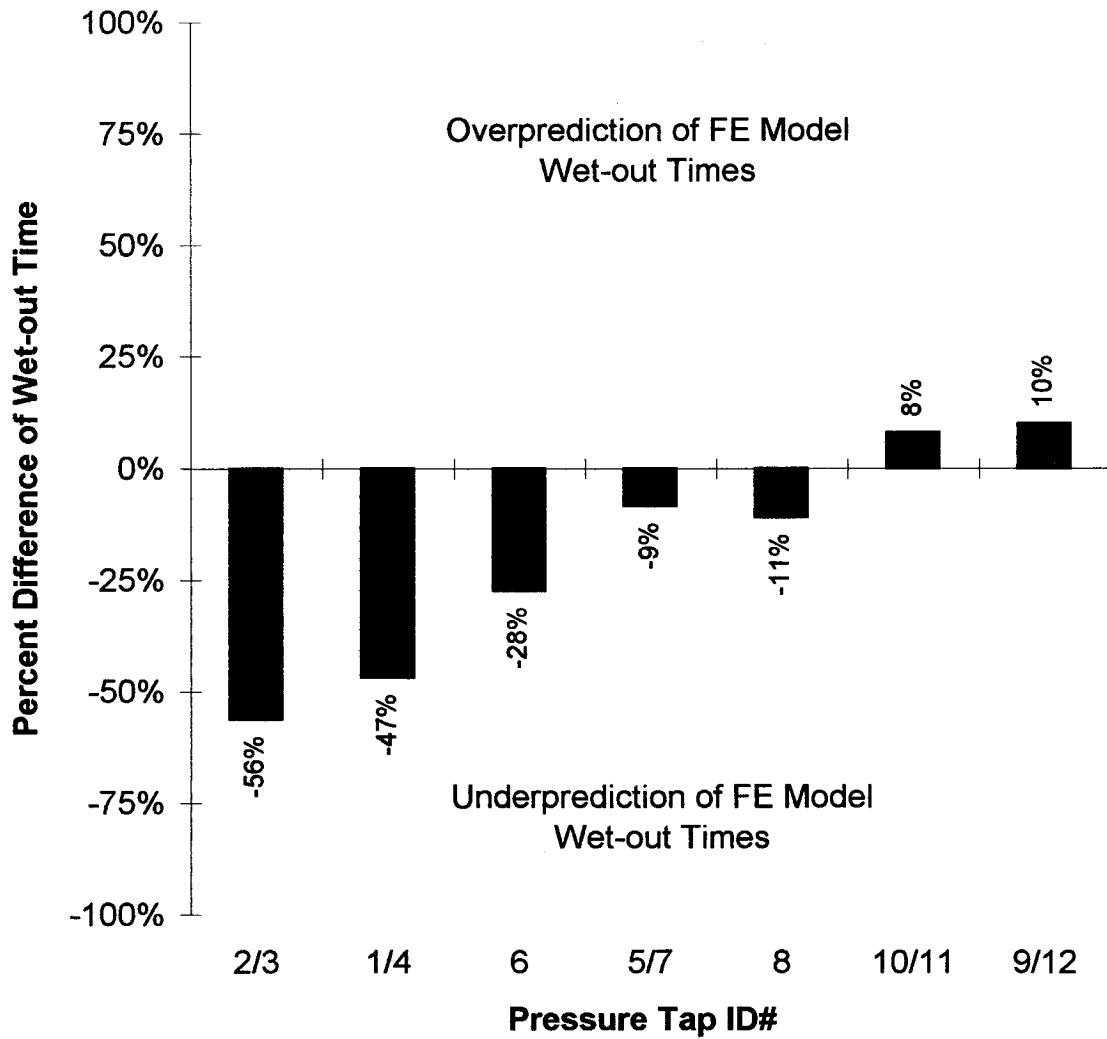pressure tap locations (see Figure 3-1), blade-stiffened preform.
Comparison of original model and experimental results to modified models
with increased fiber volume fraction (58-62%) in the region of the skin
directly under the blade.
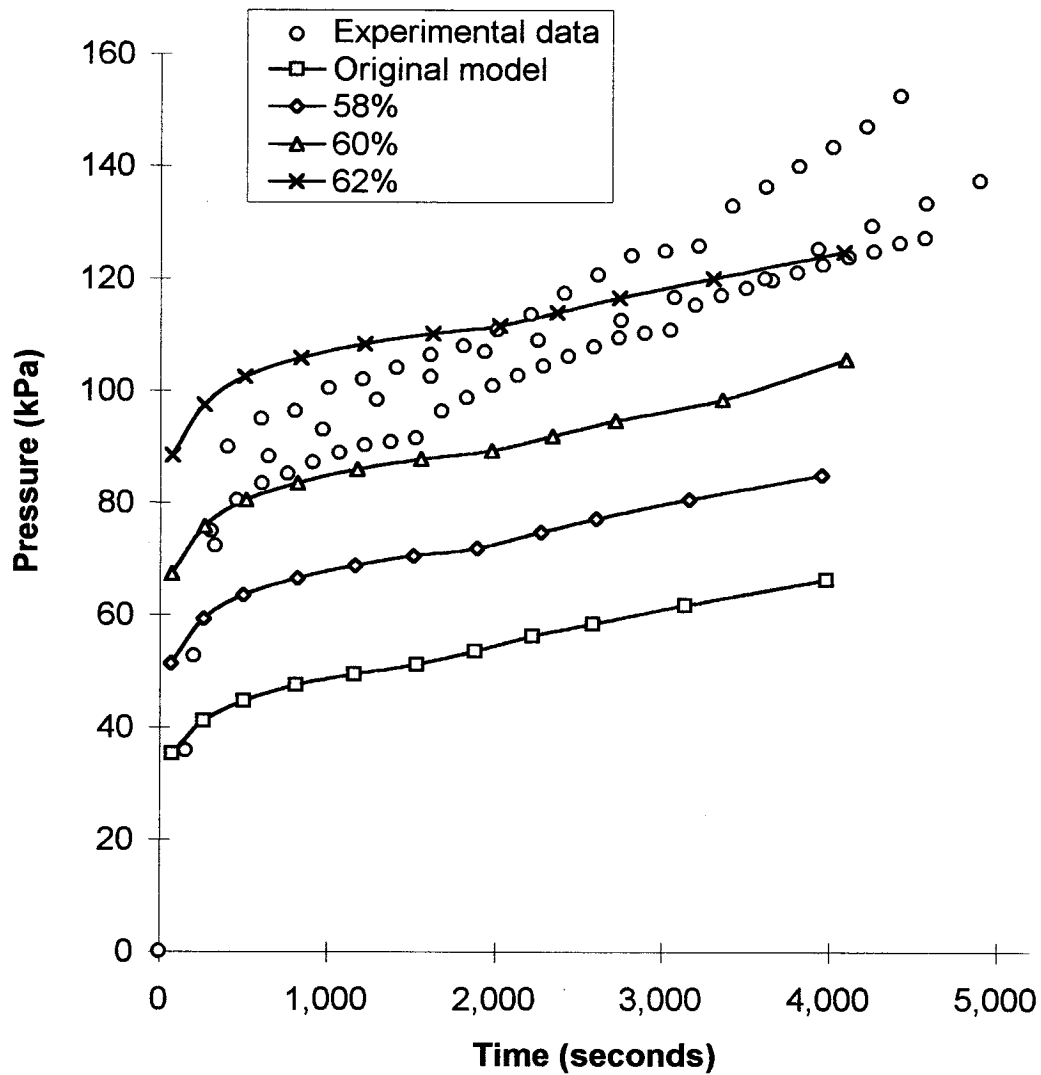
Figure 3-16    Inlet pressure, blade-stiffened preform. Comparison of original model and
experimental results to modified models with increased fiber volume
fraction (58-62%) in the region of the skin directly under the blade.

# 4. PR-500 Resin Kinetics and Viscosity

## 4.1 Introduction

The polymerization of thermosetting resins is modeled to determine the degree of cure and cure rate of the reaction chemistry. The modeling allows for prediction of mold temperatures due to the curing process and an estimation of the time needed to reach a final degree of cure.

The chemorheological behavior of thermoset resins is an important factor in processing a composite panel. It affects the flow characteristics of the mold filling process, the pressure gradient within the mold, and the porosity of the finished panel. The viscosity of a thermosetting resin is determined as a function of the degree of cure and temperature of the resin. A model can be used to predict optimum processing cycles and to minimize resin viscosity while ensuring complete mold fill.

## 4.2 Literature Review

### 4.2.1 Thermosetting Resin Cure Kinetics Modeling

Cure kinetics models are often developed to relate the cure reaction rate to the temperature and extent of cure. Several factors must be taken into account when determining which model is most applicable:

- Accuracy
- Robustness
- Simplicity of determining cure kinetics parameters
- Simplicity of final model

The majority of cure kinetics models can be categorized into three types:

- Empirical (phenomenological)
- Mechanistic
- Statistical

Empirical (phenomenological) models are used to describe the principal characteristics of the cure, without considering the mechanics of the curing process. These are typically used when a specific resin is to be modeled and the results are to be used to estimate the curing rate and degree of cure. Mechanistic models attempt to explain the chemical reaction based on the initial amounts and characteristics of the individual components. Normally, several simplifying assumptions need to be made in order to end up with a reasonable model. Finally, the statistical models noted are based on a factorial design [26], varying the desired inputs such as temperature and inhibitor level to statistically determine the coefficients. For example, if a $2^4$ factorial design is used (four variables measured at two levels) 16 isothermal runs would be made to determine the coefficients.

Another significant factor to be taken into account is the method of data measurement. Model parameters can be determined from isothermal DSC scans, dynamic DSC scans, or a combination of both. Dynamic scans typically take less time to complete and are useful in determining the overall heat of reaction. As stated by Martin and Salla [27], the activation energy (E) can be determined with good precision and accuracy, although the frequency factor (A) is more difficult to estimate, and the results are normally poor. It has been stated [28] that the kinetic parameters achieved from isothermal scans can adequately simulate both isothermal and dynamic experiments while the kinetic parameters determined from dynamic scans can only model dynamic experiments. The reason being that the data taken using dynamic scans must be altered to take into consideration the inhibition time of the resin. For an isothermal scan, the inhibition time is taken as the point where the reaction becomes exothermic.

## 4.2.2 Empirical Models

The empirical models can be divided into two categories [27]: nth-order reaction models of the form

$$f(\alpha) = (1 - \alpha)^n \qquad (4\text{-}1)$$

where $\alpha$ is the degree of cure and $n$ is the order of reaction, and autocatalytic reaction models of the form

$$f(\alpha) = \alpha^m (1 - \alpha)^n \qquad (4\text{-}2)$$

where $m$ is also an order of reaction. From previous work [27], it has been demonstrated that the autocatalyzed model better duplicates the curing process of thermosets such as unsaturated polyesters than the nth order model, at least in the case of isothermal experiments. One of the simpler autocatalyzed empirical models is proposed by Lam, Plaumann, and Tran [29]. The model takes into account the ultimate degree of conversion ($\alpha_u$), which is normally less than unity.

$$\frac{d\alpha}{dt} = k\alpha^m (\alpha_u - \alpha)^n, \qquad m + n = 2 \qquad (4\text{-}3)$$

$$k = A \exp\left[\frac{-E}{RT}\right] \qquad (4\text{-}4)$$

where $\dfrac{d\alpha}{dt}$ is the reaction rate, $R$ is the universal gas constant and $T$ is the temperature. A model proposed by Kamal and coworkers [30] combines the autocatalytic and nth order models:

88

$$\frac{da}{dt} = \left(k_1 + k_2 \, a^m\right)\left(1 - a\right)^n \tag{4-5}$$

$$k_i = A_i \exp\left[\frac{-E_i}{RT}\right] \qquad i \rightarrow 1,2 \tag{4-6}$$

For a summary of proposed kinetics models for cure characterization of thermosets, see Gebart [31].

## 4.2.3 Thermosetting Resin Viscosity Models

The viscosity of a thermosetting resin is driven by two factors - molecular structural effects caused by the chemical curing reaction and variation in segment mobility as affected by temperature [32]. The curing process is described as the transformation of the fluid resin into a rubbery state and then to a solid glass as a result of the cross-linking and 3-D network formation of the polymeric chains.

The majority of viscosity models which have been proposed are of two types - mechanistic models based on the Williams-Landel-Ferry equation and empirical models. The WLF equation describes the temperature dependence of the viscosity of a polymeric liquid to the glass transition temperature at a fixed molecular weight. Kenny, Apicella, and Nicolais [32] proposed a WLF type model to represent the cure of an epoxy/amine system as follows:

$$\frac{\eta(T,\alpha)}{\eta(T_0)} = \left(g\frac{M_w(\alpha)}{M_{w0}}\right)^{3.4} \frac{\exp\left\{C_1\left(T_r - T_{g0}\right)/\left(C_2 + T_r - T_{g0}\right)\right\}}{\exp\left\{C_1\left(T_r - T_g(\alpha)\right)/\left(C_2 + T_r - T_g(\alpha)\right)\right\}} \tag{4-7}$$

$\eta$: viscosity

$M_w$: molecular weight average

$M_{w0}$: initial molecular weight average

$g$: ratio of the radii of gyration of a branched chain to a linear chain of the same molecular weight

$T_r$: reference temperature

$T_0$: initial temperature

$T_g$: glass transition temperature of the reacting system

$T_{g0}$: initial glass transition temperature

$C_1, C_2$: constants

The equation requires knowledge of the molecular weight and glass transition temperature of the thermoset as a function of degree of cure.

An empirical model for the viscous behavior of a thermosetting polyurethane has been proposed by Castro and Macosko [33]:

$$\eta = \eta_0 \cdot \left( \frac{\alpha_g}{\alpha_g - \alpha} \right)^{(c_1 + c_2 \alpha)} \tag{4-8}$$

$$\eta_0 = A_\eta \exp\left( \frac{E_\eta}{R * T} \right) \tag{4-9}$$

where $\alpha_g$ is the degree of cure at gel, $A_\eta$ is the frequency factor, $E_\eta$ is the activation energy, and $c_1$ and $c_2$ are experimental constants.

Gebart [31] summarizes eleven empirical viscosity models used for the characterization of thermosetting resins.

## 4.3 Theory

### 4.3.1 Cure Kinetics

The degree of cure of a thermosetting resin is defined as the amount of heat evolved at a specific time divided by the total heat of reaction.

$$\alpha = \frac{H(t)}{H_r} \qquad (4\text{-}10)$$

$H(t)$: amount of heat evolved at time t

$H_r$: total heat of reaction

The degree of cure is calculated by integrating the rate of reaction over the time interval.

$$\alpha = \int_0^t \left(\frac{d\alpha}{dt}\right) dt \qquad (4\text{-}11)$$

The amount of heat evolved at time t for the neat resin is calculated by integrating the rate of heat generation ($dH/dt$) over the time interval.

$$H(t) = \int_0^t \frac{dH}{dt} dt \qquad (4\text{-}12)$$

The total heat of reaction of the resin is calculated by integrating the rate of heat generation over the entire time interval required for the resin to become completely cured.

$$H_r = \int_0^{t_r} \frac{dH}{dt} dt \qquad (4\text{-}13)$$

where $t_r$ is the time required for the resin to become completely cured. To compute the total heat of reaction for a saturated preform, the effects of the preform must be added to the heat generation term. The total heat of reaction ($H_R$) for a saturated preform is calculated.

$$H_R = \frac{\rho_r}{\rho_c} \, v_r \, H_r \qquad (4\text{-}14)$$

$\rho_c$:  density of resin saturated preform
$\rho_r$:  density of resin
$v_r$:  resin volume fraction

The rate of change of the total heat of reaction ( $\dot{H}_R$ ) can then be calculated as follows:

$$\dot{H}_R = \frac{d\alpha}{dt} \, H_R \qquad (4\text{-}15)$$

## 4.4 Resin Kinetics: Experimental Results

The cure kinetics of PR-500, a one part high-performance epoxy designed for the Resin Transfer Molding process, were modeled. Isothermal DSC scans with residual dynamic scans were completed at 160°, 170°, 180°, 190°, and 200°C on a Dupont 910 DSC with a TA2100 controller.

The resin samples were prepared by pouring the resin in a thin sheet and refrigerating to -4°C. Solid resin samples were obtained by breaking the thin sheet into smaller particles. The samples were weighed and set into DSC pans. Hermetically sealed sample pans were used to minimize mass loss during the curing stage.

The DSC cell was preheated to the desired test temperature prior to placing the sample. Each sample was heated isothermally for 160 minutes and immediately ramped from the test temperature at 10 C/min. to 300 C to ensure that the sample was completely

cured and to obtain the total heat of reaction for each sample. The sample rate used was 1 sample/second. The data were then fit to Equations 4-5 and 4-6.

The data were manipulated prior to curve-fitting (see Figure 4-1 and Figure 4-2). From the isothermal scan, the horizontal base-line was taken to be a line parallel to the time axis intercepting the heat generation curve at 160 minutes, and corresponds to zero heat flow. The intercept of the base-line with the heat generation curve was assumed to be t = 0. The total area beneath the heat generation curve and the base-line from t=0 to t=160 minutes is the total isothermal heat of reaction ($H_{Riso}$) generated during the isothermal scan.

The amount of heat evolved during the dynamic scan was measured by setting a baseline tangent to the heat generation curve near the local minimums (see Figure 4-2) . The area between the curve and the baseline was calculated, and represents the total amount of residual heat of reaction ($H_{Rdyn}$). The total heat of reaction ($H_R$) was calculated as follows:

$$H_R = H_{Riso} + H_{Rdyn} \qquad (4\text{-}16)$$

The ratio of the heat generated at a given time divided by the sum of the total heat evolved during both the isothermal and dynamic scan is considered the degree of cure ($\alpha$). See Figure 4-3.

A Levenberg-Marquardt non-linear least squares curve-fitting algorithm [34] was used to simultaneously fit the six parameters $A_1, E_1, A_2, E_2, m$, and $n$ in Equations 4-5 and 4-6 to the data obtained at different temperatures. The parameters were varied until the error between the data curves and the model was minimized. The final resin kinetic parameters are shown in Table 4-1.
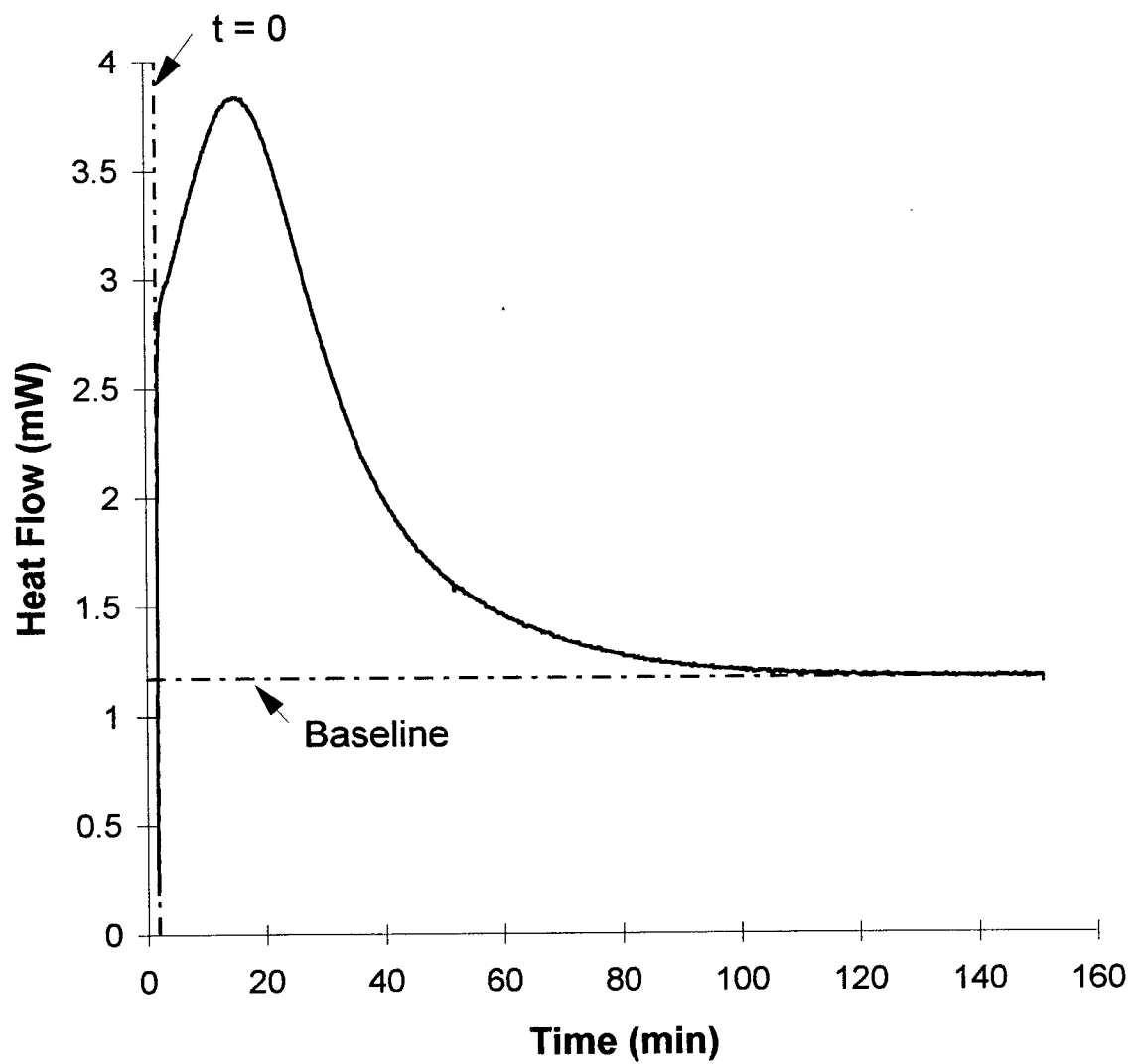
Figure 4-1    180°C Isothermal DSC scan, 3M PR-500 epoxy resin.

Temperature profile:
10 C/min to 300 C

Baseline
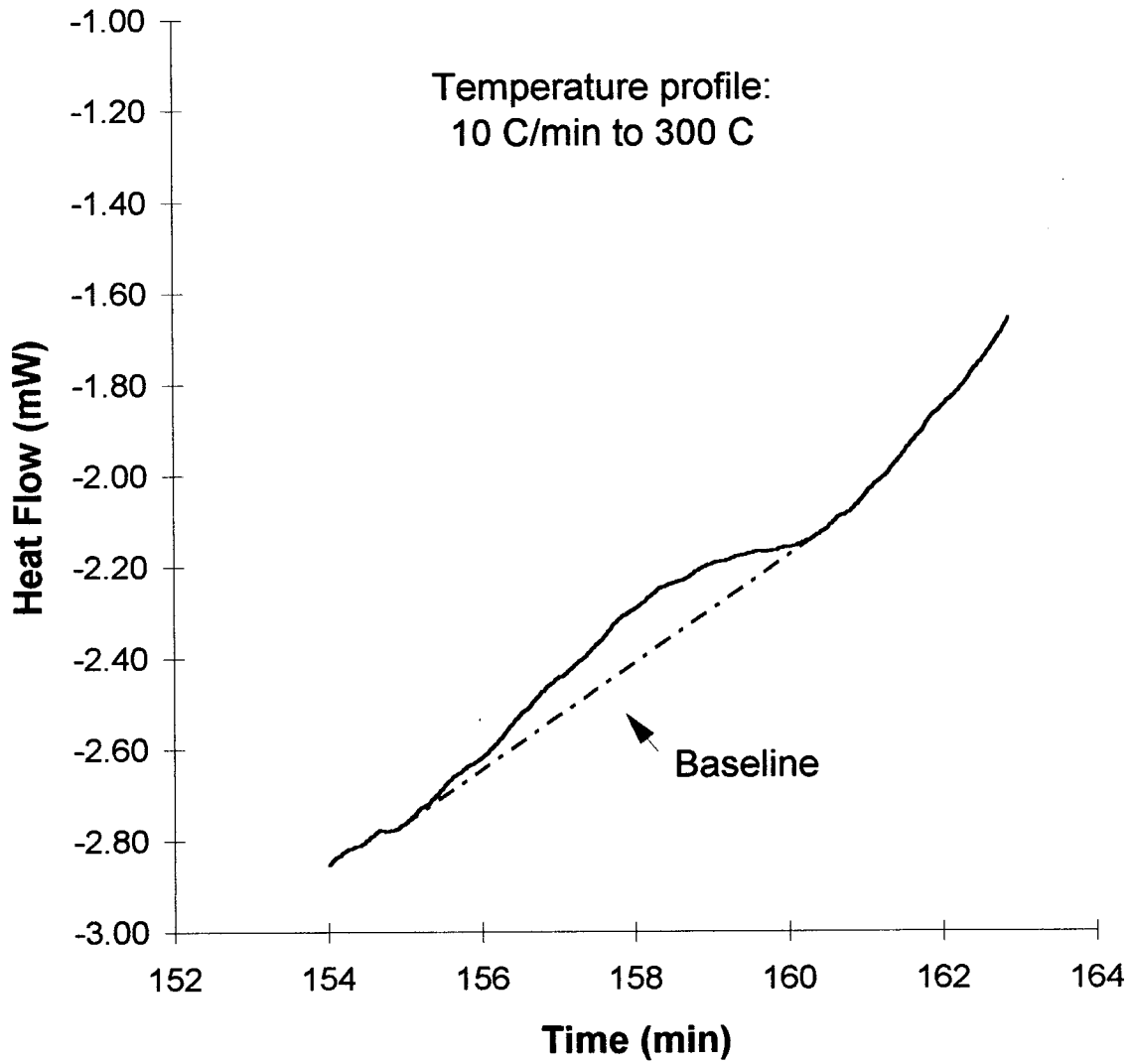
Figure 4-2      180°C residual dynamic DSC scan, 3M PR-500 epoxy resin.
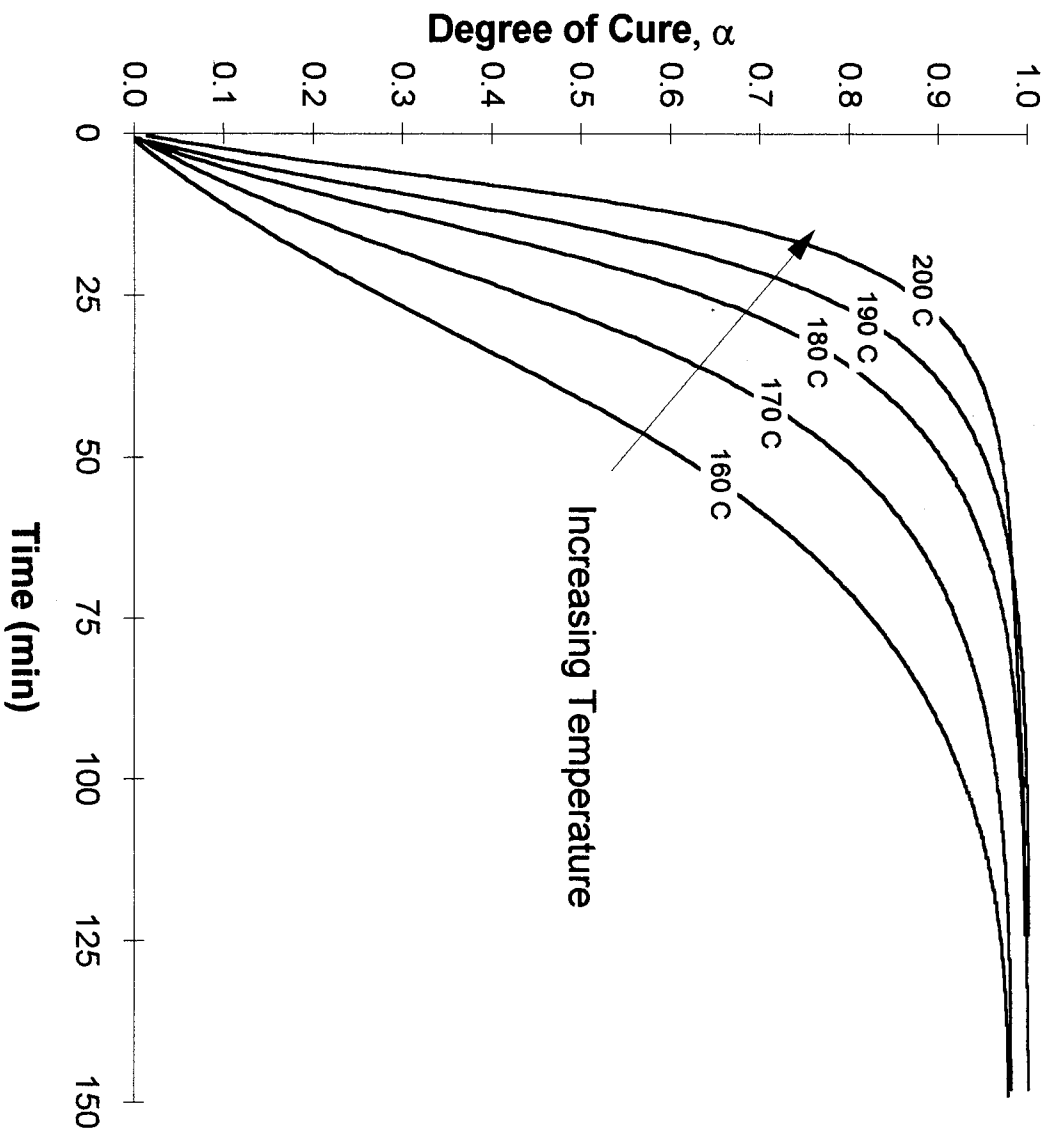
Figure 4-3    Degree of cure vs. time, 3M PR-500 epoxy resin.

Table 4-1      PR-500 resin kinetics parameters

| A₁ (1/min.) | E₁ (kJ/kmol) | A₂ (1/min.) | E₂ (kJ/kmol) | m | n |
|---|---|---|---|---|---|
| .3122E+07 | .7151E+05 | .2286E+05 | .4656E+05 | .9993E+00 | .1352E+01 |

A comparison between the measured and calculated cure rate versus degree of cure at various temperatures is shown in Figure 4-4. Overall, the agreement between the predicted cure rate and the measured cure rate is very good.

The model was verified for the following ramp-hold sequence. A DSC scan was performed on a weighed PR-500 resin sample placed in a hermetically sealed sample pan. The sample was ramped at 7.5°C for 25 minutes from 30°C to 217.5°C. The sample was immediately quenched. The DSC was then preheated to 217.5°C, and the sample was again placed in the DSC cell and scanned at 217.5°C for 25 additional minutes. The predicted degree of cure was then plotted against the experimental data as shown in Figure 4-5.

## 4.5 Resin Viscosity: Experimental Results

The rheometric data was supplied by 3M and was taken at isothermal temperatures of 150, 160, 180, 190, and 200°C. The viscosity versus time data is presented in Figure 4-6.

Initially, the data were converted to viscosity versus degree of cure (see Figure 4-7) by implementing the model previously developed for the cure kinetics. The degree of cure at which the resin gels ($\alpha_g$) is assumed to be a linear function of temperature for the resin system studied (see Figure 4-8). For this resin system, $\alpha_g$ was considered to be the degree of cure at a viscosity of 10.0 Pa-sec. A linear least squares fit to the data was
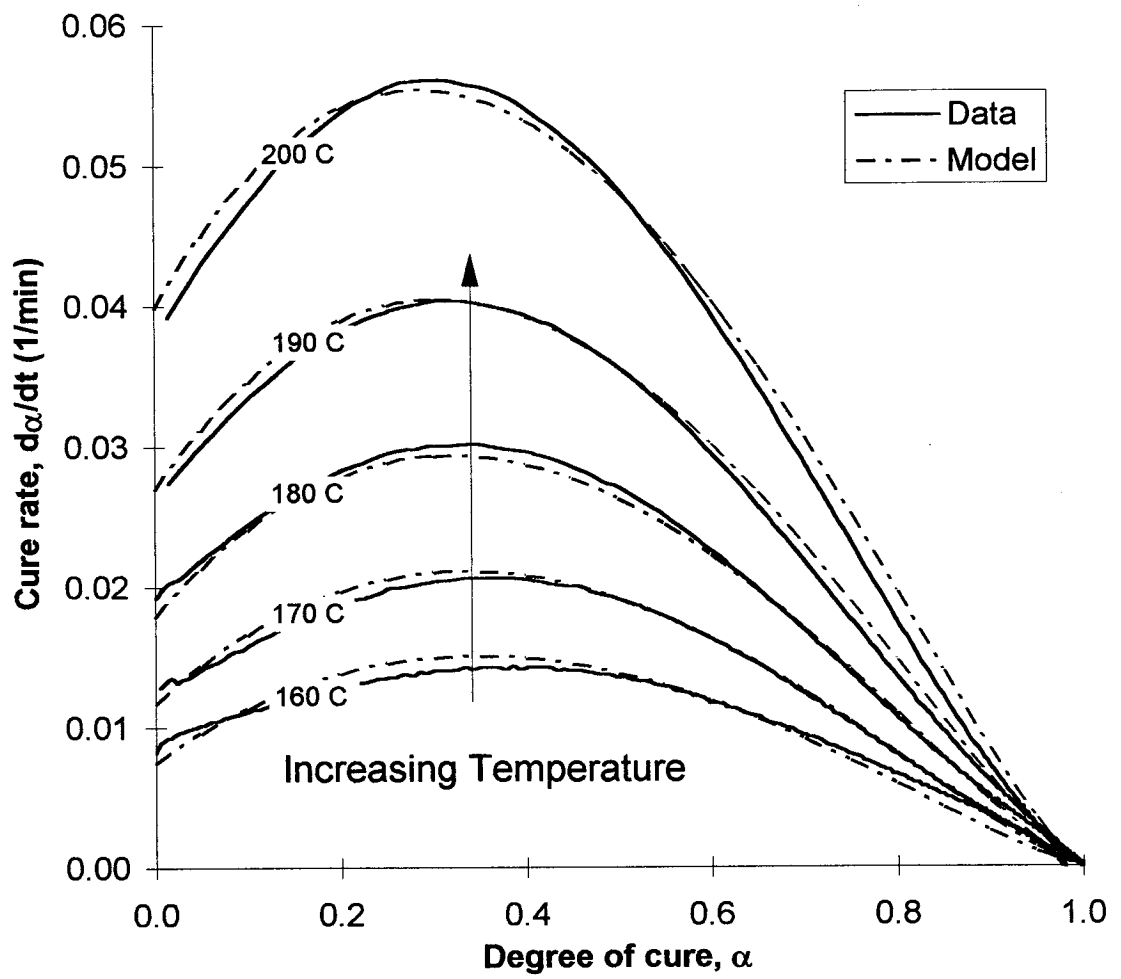
Figure 4-4    Cure rate versus degree of cure - experimental and model results, 3M PR-
500 epoxy resin.

1. Ramp from 30C at 7.5C/min for 25 minutes to 217.5C
2. Hold at 217.5C for 25 minutes
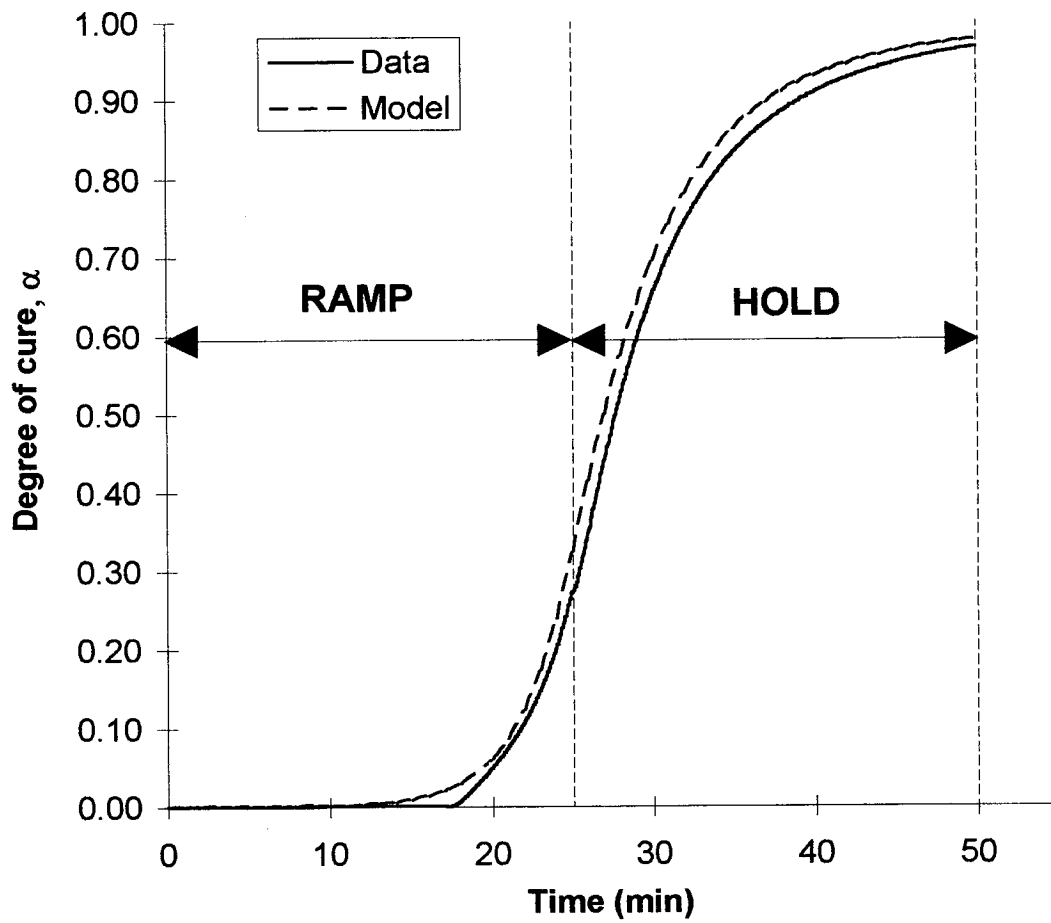
Figure 4-5    Cure kinetics model verification - degree of cure versus time, 3M PR-500 epoxy resin.
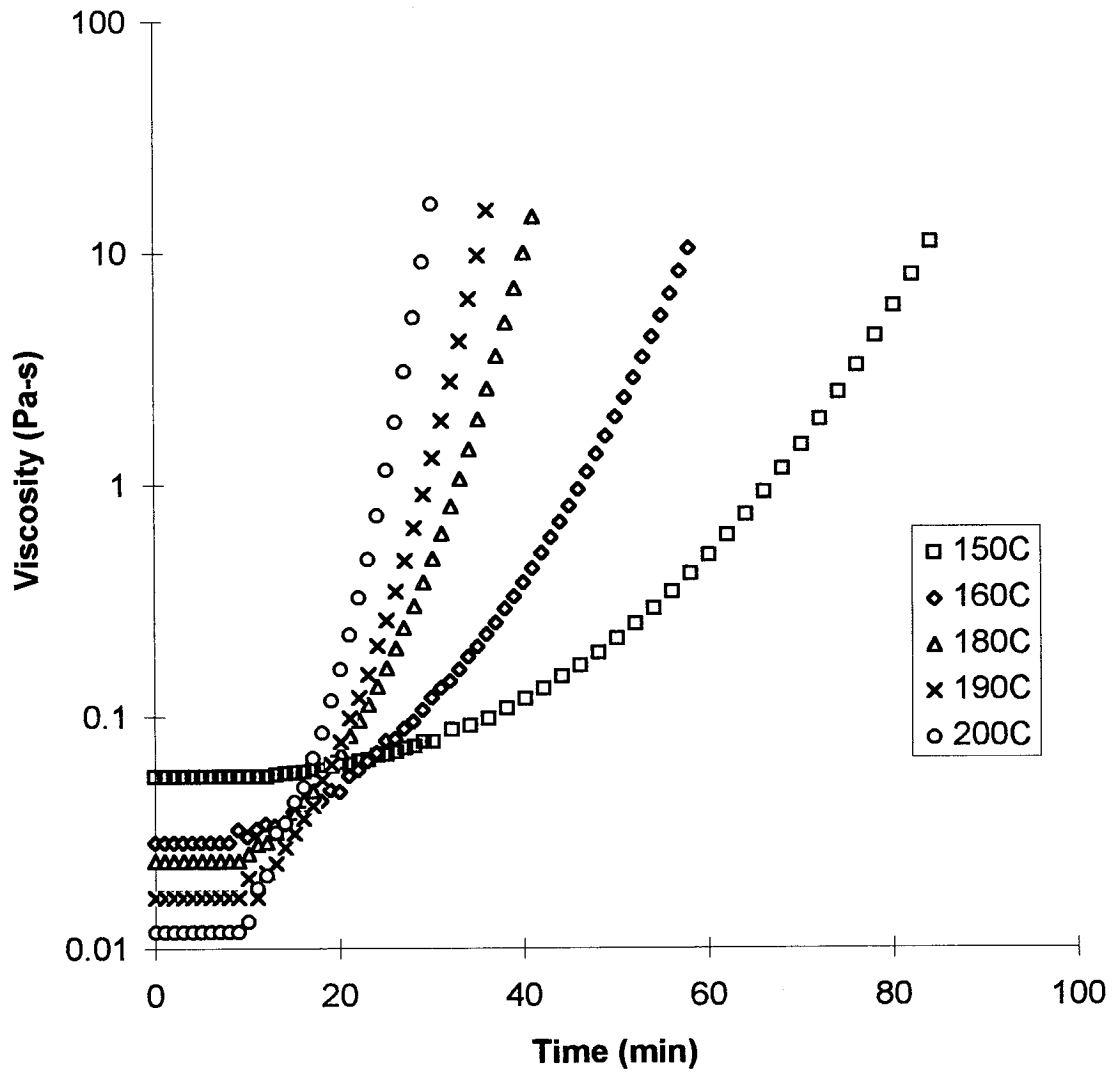
Figure 4-6    Viscosity versus time data, 3M PR-500 epoxy resin.
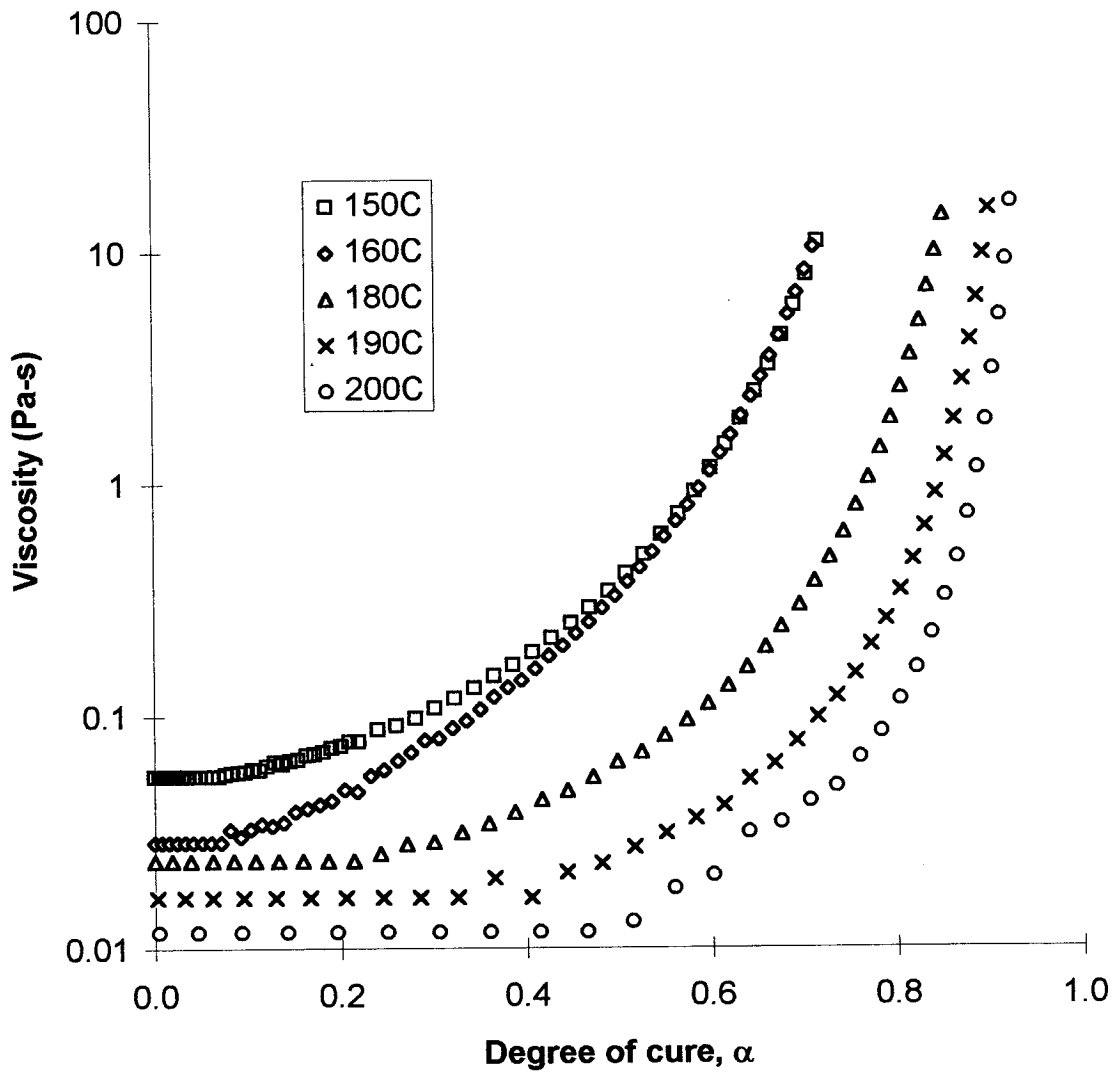
Figure 4-7       Viscosity versus degree of cure, 3M PR-500 epoxy resin.
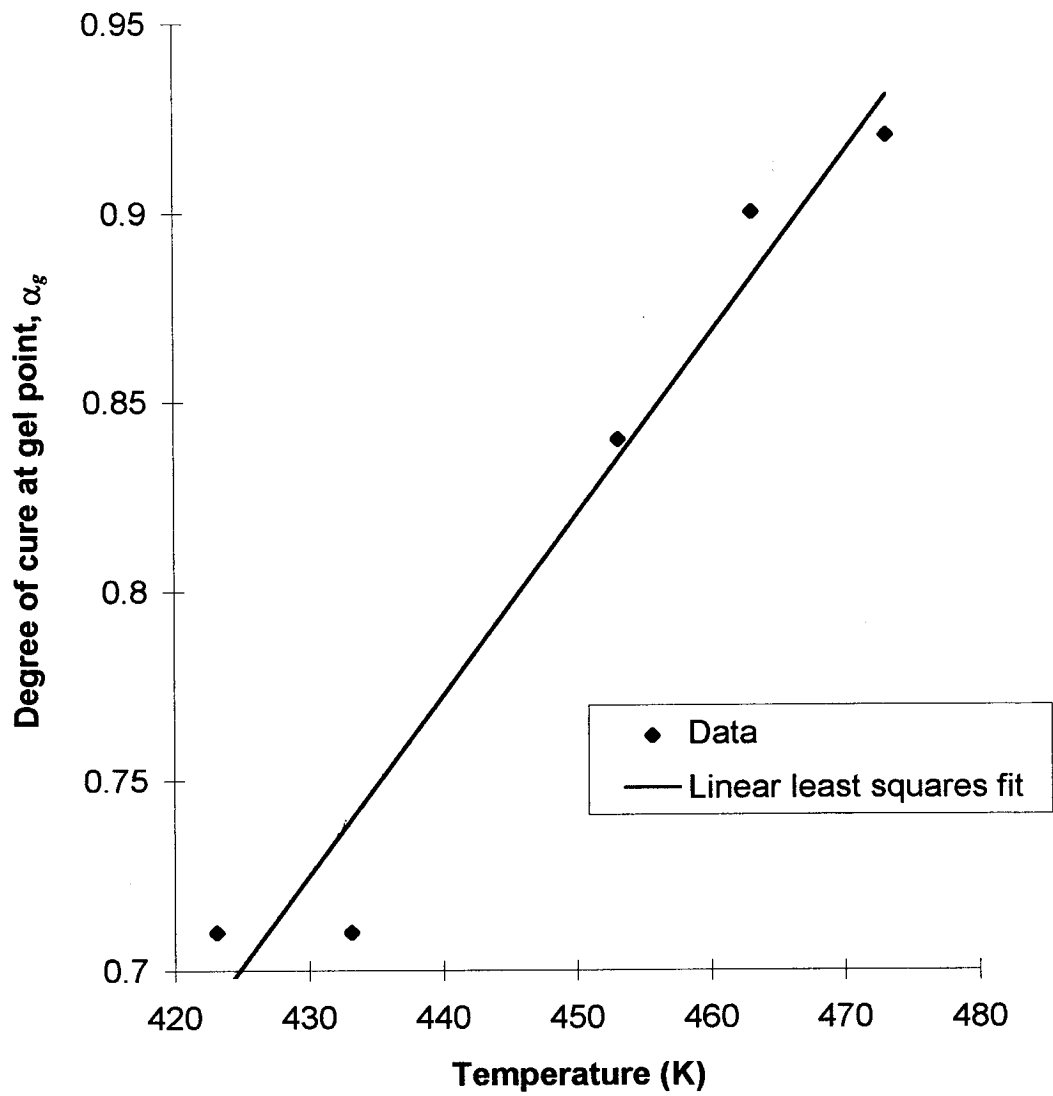
Figure 4-8    Degree of cure at gel point versus isothermal temperature, 3M PR-500
epoxy resin.

completed and the results are plotted in Figure 4-8:

$$\alpha_g(T) = 0.004779T - 1.33057 \tag{4-17}$$

Castro and Macosko's viscosity model [33] discussed in Section 4.2.3 was modified to account for the temperature dependence of $\alpha_g$:

$$\eta = \eta_0 \cdot \left( \frac{\alpha_g(T)}{\alpha_g(T) - \alpha} \right)^{(c_1 + c_2 \alpha)} \tag{4-18}$$

$$\eta_0 = A_\eta \cdot \exp\left( \frac{E_\eta}{RT} \right) \tag{4-19}$$

$$\alpha_g(T) = c_3 T + c_4 \tag{4-20}$$

A Levenberg-Marquardt non-linear least squares curve-fitting algorithm [34] was used to simultaneously fit the four parameters $A_\eta, E_\eta, c_1$, and $c_2$. The parameters were varied until the error between the data curves and the model was minimized. The following error function was minimized:

$$\chi^2 = \sum_{i=1}^{n} w_i (\eta_i - \eta_{\text{mod}}) \tag{4-21}$$

where $n$ is the number of viscosity data points, $\eta_i$ is the ith viscosity data point, $\eta_{\text{mod}}$ is the model predicted viscosity, and $w_i$ is a weighting function. Because of the logarithmic nature of the viscosity model, the weighting function was defined as $w_i = \dfrac{1}{\eta_i}$ and

$$\chi^2 = \sum_{i=1}^{n} \frac{(\eta_i - \eta_{mod})}{\eta_i} \qquad (4\text{-}22)$$

The result of such a weighting function was to assign an higher probability of the function passing through the data points at lower viscosities.

Only the 150, 180, 190, and 200°C data was fit to the model. The 160°C data were not used because of the discrepancy in the viscosity versus degree of cure results (see Figure 4-7) when compared to the data taken at other temperatures. Also, only viscosity data in the range of 0.00 - 0.20 Pa-s was used to fit the model. The calculated parameters are presented in Table 4-2.

Table 4-2    PR-500 viscosity model parameters.

| $A_\eta$ (Pa-s) | $E_\eta$ (kJ/kmol) | $c_1$ | $c_2$ | $c_3$ (K$^{-1}$) | $c_4$ |
|---|---|---|---|---|---|
| .2838E-7 | 0.5107E+5 | .4909E+0 | .6615E+0 | .4779E-2 | -.1331E+1 |

The model predicts the viscosities at an initial degree of cure of zero fairly close (see Figure 4-9 and Figure 4-10). At temperatures at or below 180°C the model fits well with the viscosity data before gelation. At higher cure temperatures, it over-predicts the viscosity before gelation. Also, the viscosity rise during cure is under-predicted at lower cure temperatures. Finally, the model slightly over-predicts the degree of cure at which the resin gels at lower isothermal temperatures and under-predicts the degree of cure at which the resin gels at higher temperature ranges. These results are felt to be due to the

104
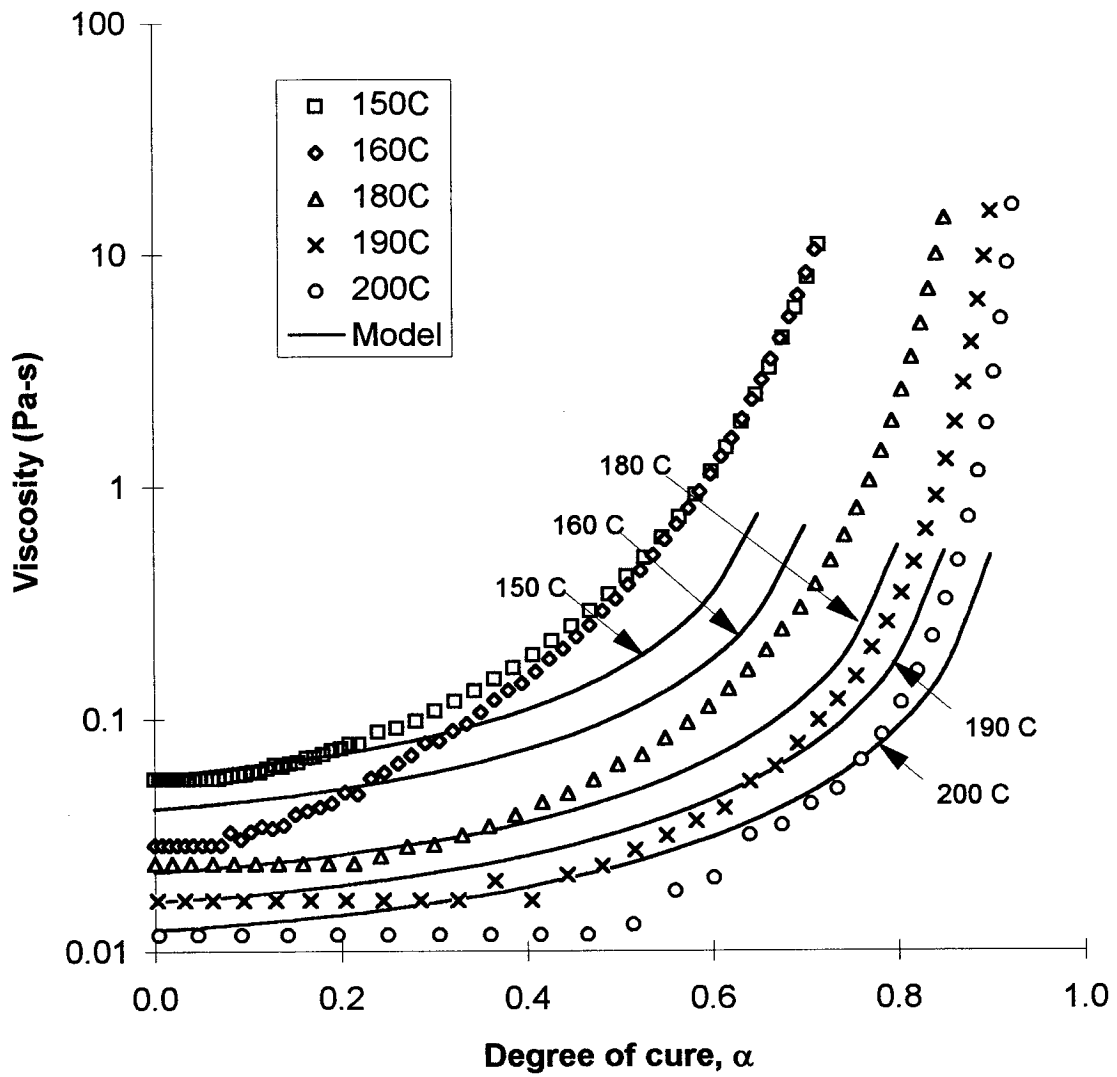
Figure 4-9    Viscosity versus degree of cure, 3M PR-500 epoxy resin.
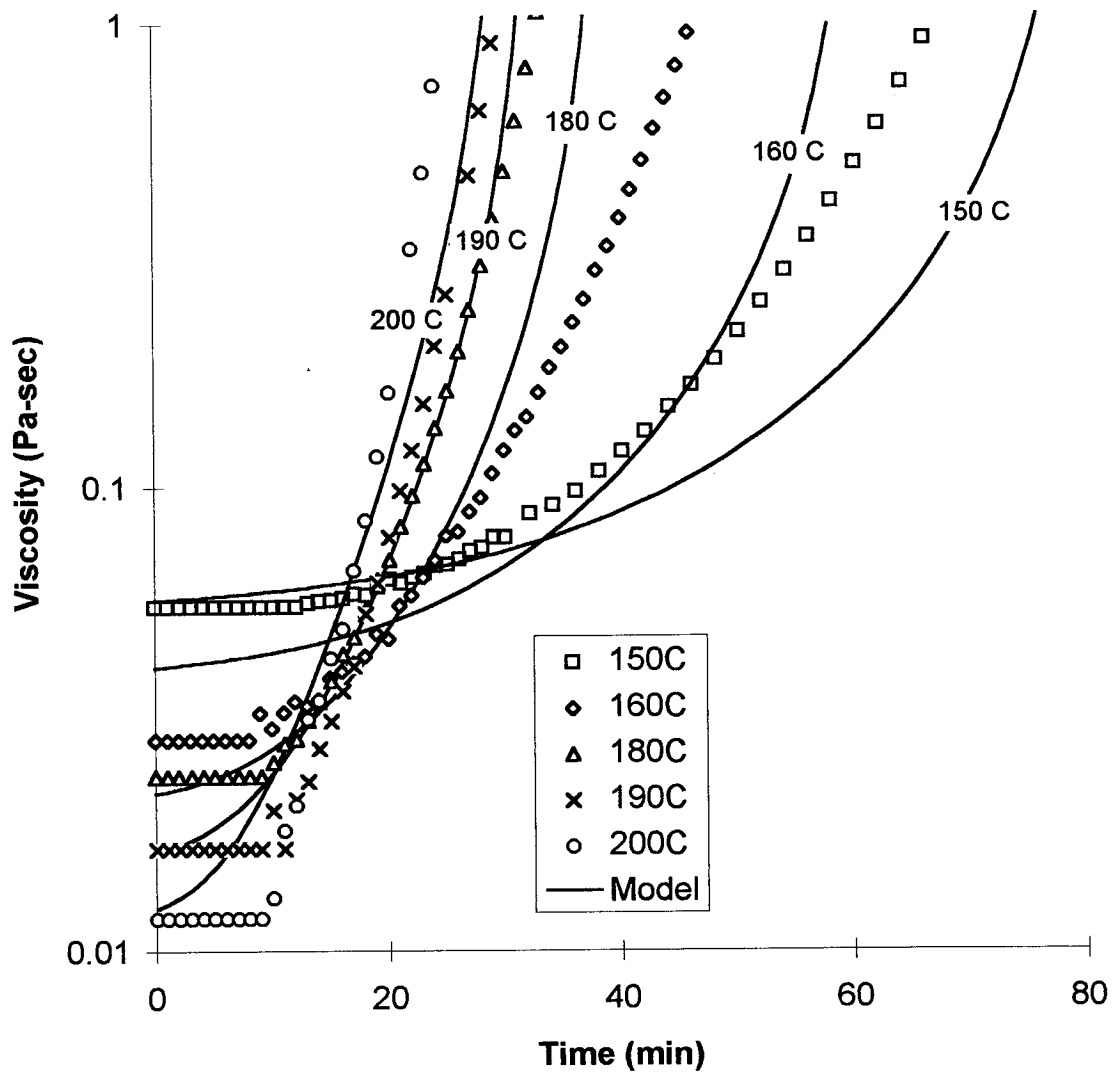
Figure 4-10    Viscosity versus time, 3M PR-500 epoxy resin.

limitations of the ability of the model to fit the discontinuity in slope of the viscosity versus time high temperature data. This occurs when the slope in viscosity abruptly changes as gelation begins.

# 5. Resin Transfer Molding Experiments and Model Verification

## 5.1 Introduction

Three PR-500 epoxy resin/IM7 8HS carbon fabric flat panels were fabricated by the Resin Transfer Molding process. Temperature, pressure, and FDEMS sensor measurements were taken to monitor the process conditions. Pressure and flow front position data obtained during the experiments were compared with the predictions of the RTM simulation model.

## 5.2 Literature Review

Kendall and Rudd [35] undertook experiments to characterize practical RTM cycles, using pressure transducer, thermocouple, and dielectric sensor feedback to better understand the process. Their results were not compared to theoretical models. It was emphasized that two of the most critical parameters to be measured for real-time control are mold filling and mold opening. They determined that the use of thermocouples to determine the resin flow front position was ineffective since as the flow front progresses, the rate of change of temperature with respect to time becomes negligible. The use of pressure transducers to measure flow front position was recommended for processes with long flow lengths and/or slow impregnation rates with the added benefit of being non-intrusive. In addition, hydrostatic pressure increases which take place during the heating of the liquid resin can be measured. Kendall noted that the peak mold pressure was five times greater than the peak impregnation pressure, an important consideration in the design of molds. Also, they considered the use of metal sheathed thermocouples ineffective because of the lag introduced by the sheathing. Therefore, it was recommended to use twisted wire thermocouples (40 AWG) to minimize the delay. The

use of pressure transducers at the inlet was recommended to prevent excessive pressure due to resin gelation and excessive shot size. The detrimental effects of overpressurization were noted to include fiber wash, localized mold distortion, resin leakage, and clamp damage. It was noted that a thermocouple located near the resin inlet could be an effective measure of the degree of cure since the resin would have had the shortest residence time and would be the final place to cure. The possibility of using a pressure transducer at the inlet to detect the volumetric changes in the resin during the curing process was deemed to be a less reliable method and would require positive pressure to be maintained in the mold following impregnation.

Hammond [8] ran flat panel RTM tests with Shell 1895/W resin and IM7/8HS preforms. The panels were injected with resin at the perimeter of the preform. Inlet pressure as well as FDEMS sensor data were taken. Hammond reports a good match between FDEMS sensor data and model predicted wet-out times, with the exception of FDEMS sensors located near the edge of the preform. He attributed the difference in predicted and measured wet-out times for the FDEMS sensors near the edge of the preform to a mismatch in location of the preform within the mold.

## 5.3 Equipment

A steel mold which utilized both center-port and perimeter injection methods (see Figure 5-1 and Figure 5-2) was used to manufacture flat rectangular panels. The mold cavity was 31.75 cm wide, 31.75 cm long, and approximately 2.54 cm thick. The mold was comprised of the following four mold components:

- Lower mold plate LP1 (six FDEMS sensors) or lower mold plate LP2 (three FDEMS sensors). See Figure 5-3 for details.
- Picture frame PF1 (center port injection) or picture frame PF2 (perimeter injection). See Figure 5-4 for details.
- Spacer plate
- Upper mold plate

UPPER MOLD
PLATE

SPACER
PLATE

INJECTION PORT

PREFORM

OUTLET PORT

WARP DIRECTION

FDEMS
SENSOR PORT:

LOWER MOLD
PLATE

TEMPERATURE/PRESSURE
SENSOR PORT:
11 TOTAL

MOLD
FRONT
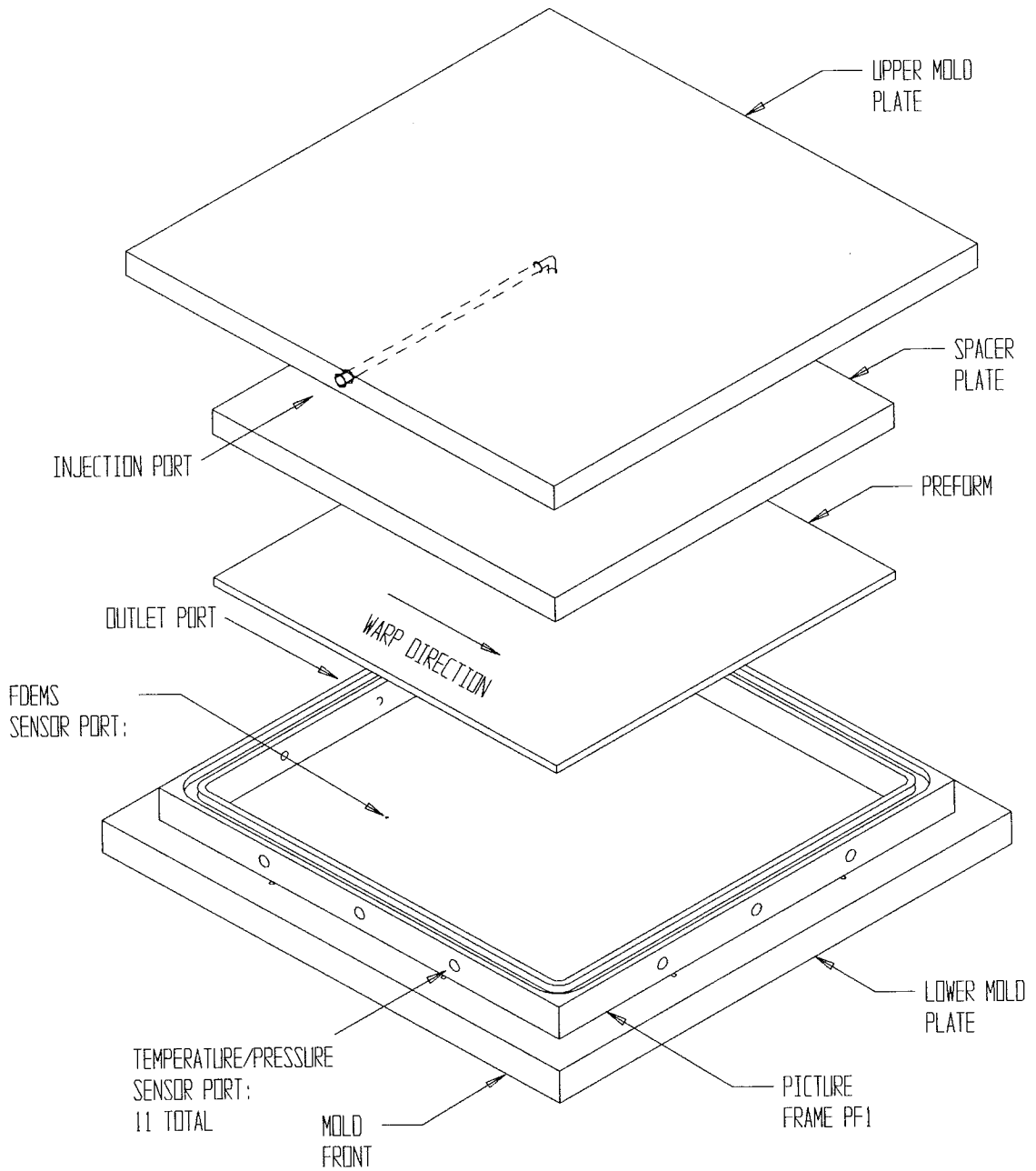
PICTURE
FRAME PF1

Figure 5-1    RTM mold, center port injection - picture frame PF1.

OUTLET
PORT

UPPER MOLD
PLATE

SPACER
PLATE

PREFORM

FDEMS
SENSOR PORT

WARP DIRECTION

INJECTION PORT

LOWER MOLD
PLATE

RESIN
CHANNEL

TEMPERATURE/PRESSURE
SENSOR PORT:
11 TOTAL

MOLD
FRONT
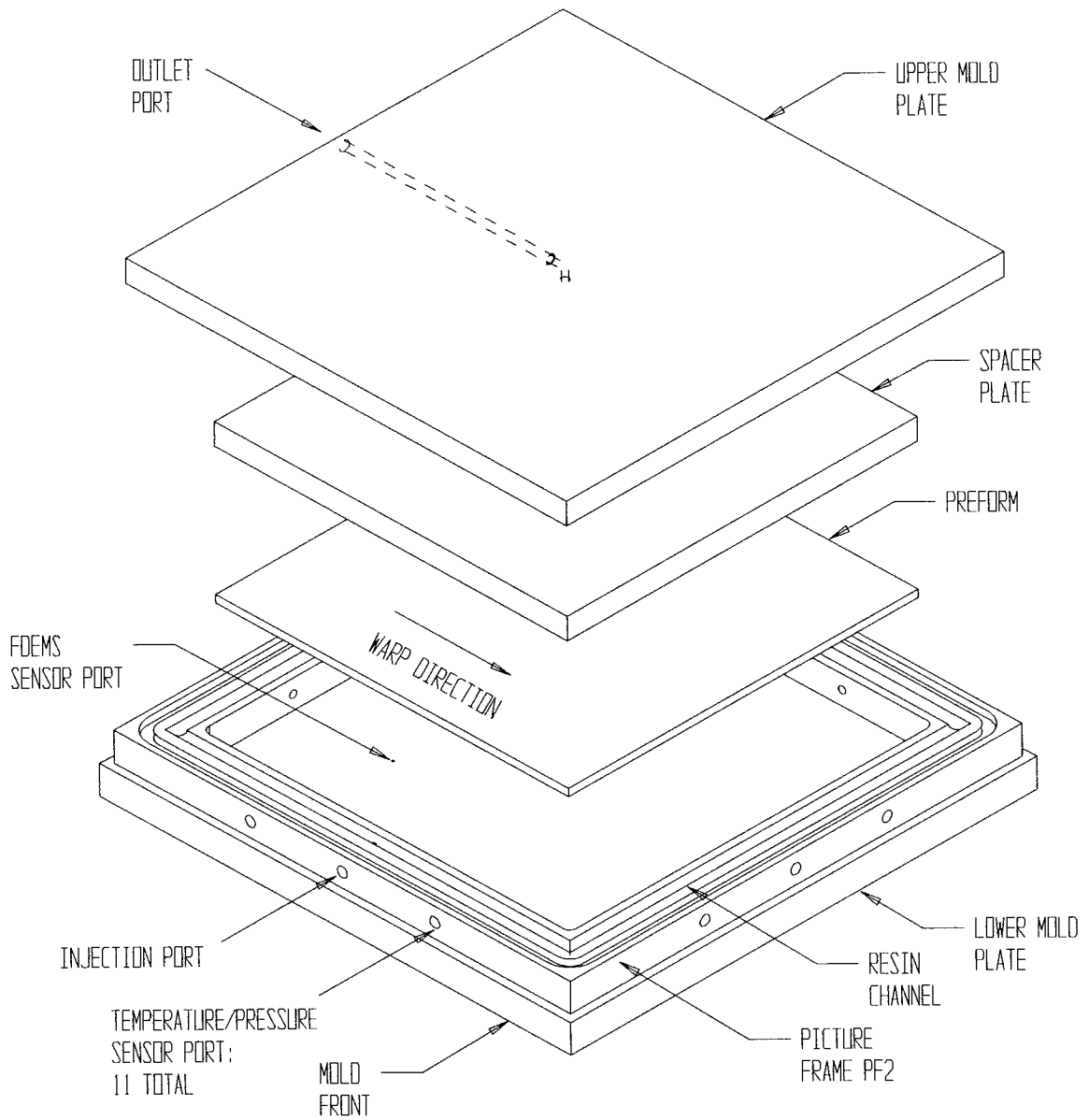
PICTURE
FRAME PF2

Figure 5-2    RTM mold, perimeter injection - picture frame PF2.

111
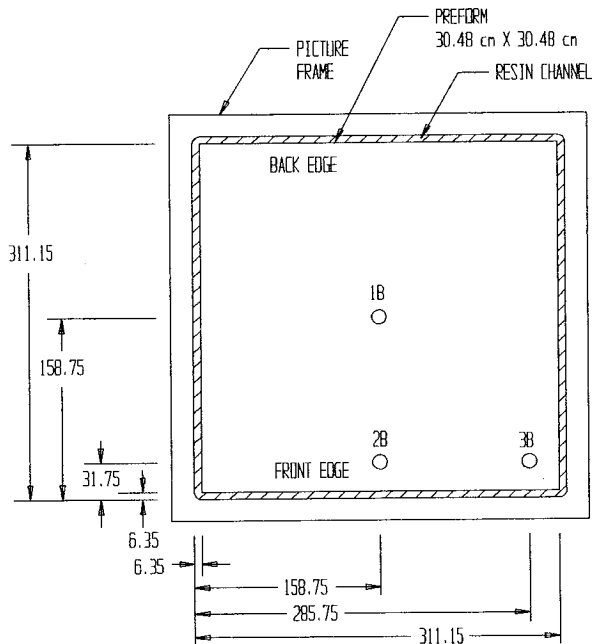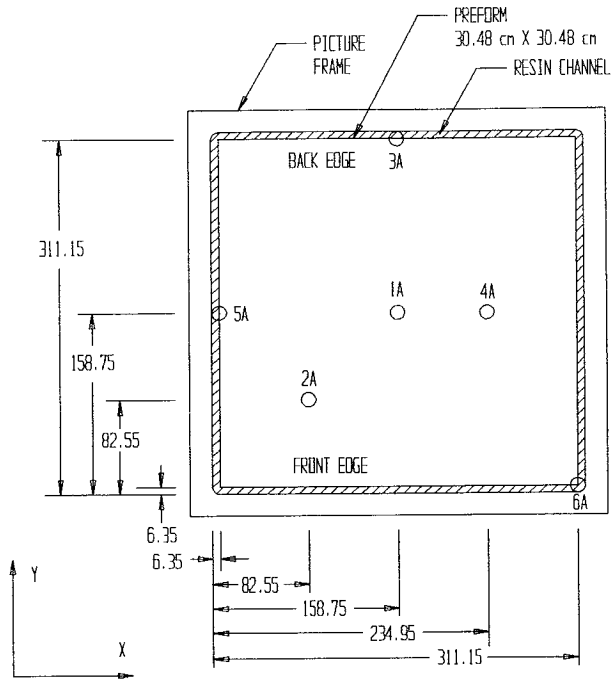
Figure 5-3    FDEMS sensor location, lower mold plate LP1 (top) and lower mold plate LP2 (bottom).

.254 MM GAP

UPPER MOLD PLATE

OUTLET PORT

SPACER PLATE

INJECTION PORT

PREFORM

LOWER MOLD PLATE

PICTURE FRAME PF2 SCHEMATIC - PERIMETER INJECTION

UPPER MOLD PLATE

INJECTION PORT

SPACER PLATE

OUTLET PORT

PREFORM

LOWER MOLD PLATE

PICTURE FRAME PF1 SCHEMATIC - CENTER PORT INJECTION
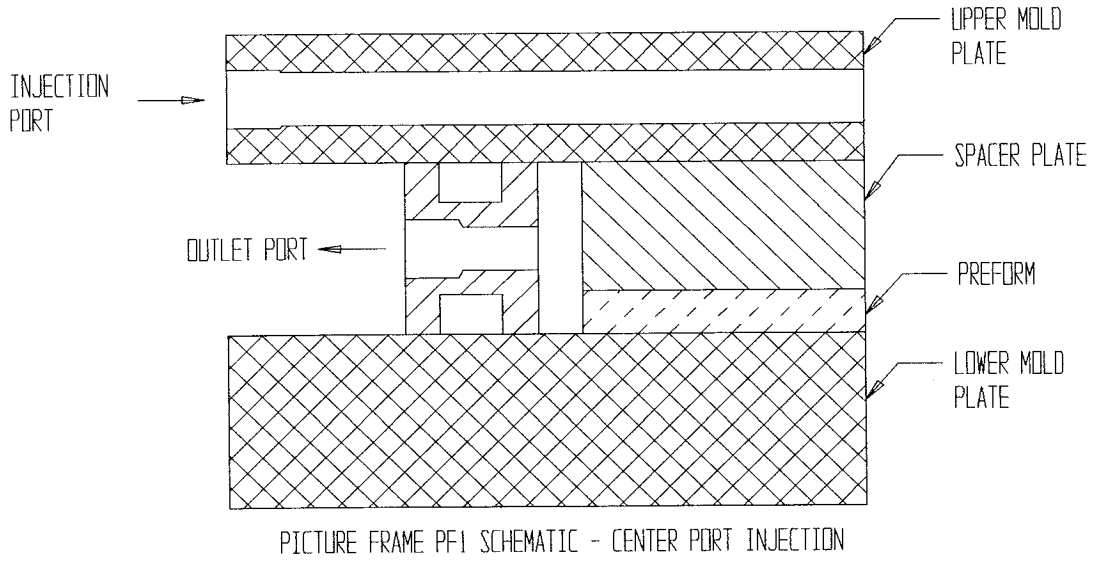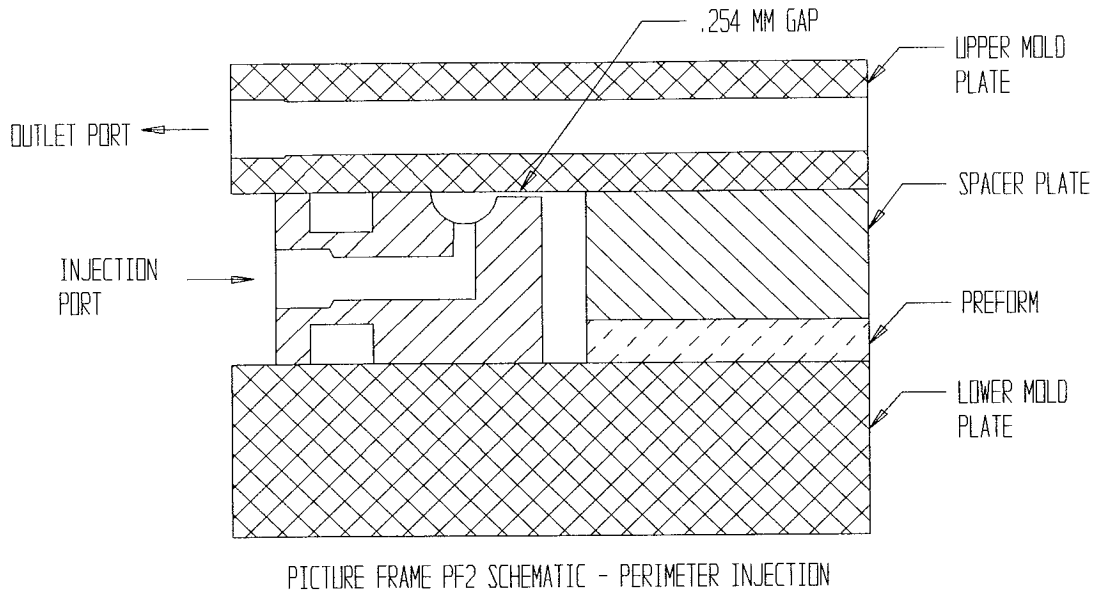
Figure 5-4    RTM mold  - picture frames PF1 and PF2 detail.

Up to six frequency dependent electromagnetic (FDEMS) sensors were utilized to sense flow front position and were mounted on the bottom side of the lower mold plate [36]. The sensors were mounted in specially designed plugs which were screwed into cavities machined into the bottom of the lower mold plates. 1.58 mm diameter holes were drilled in the lower plate at the geometric center of each cavity to create a resin sensing port between the FDEMS and the preform. Lower mold plate LP1 had six FDEMS sensor locations and lower mold plate LP2 had three FDEMS sensor locations (see Figure 5-3).

Picture frames PF1 and PF2 each had twelve 1/8 inch NPT taps around the perimeter to allow pressure transducers and thermocouples to be routed into the mold. The dimensions of the spacer plate were 15.24 cm wide x 15.24 cm long x 1.905 cm thick. With the spacer plate installed, the approximate mold cavity height is 0.63 cm.

Picture frame PF1 (see Figure 5-1 and Figure 5-4) was designed for center port injection of the flat panels. The resin enters the preform at the center of the preform through the upper mold and spacer plates. After the resin saturates the preform and fills the 0.635 cm channel surrounding the preform, it exits the mold at a port located in the picture frame.

Picture frame PF2 (see Figure 5-2 and Figure 5-4) was designed for perimeter injection. The resin is injected into the picture frame inlet port which then fills a cavity traversing the entire perimeter of the picture frame. A small 0.254 mm thick by 63.5 mm wide gap connects the channel to the mold. The picture frame was designed to evenly distribute the resin around the perimeter of the mold cavity prior to filling the mold cavity. The volume of the cylindrical groove on the upper surface of the picture frame (see Figure 5-4) was estimated at 48.67 cc.

Resin injection and cure of the preform was performed in a Wabash compression molding press with 60 cm x 60 cm heated platens. A mold closure pressure of 1080 kPa was used for all experiments. The press used a microprocessor to control the platen pressure and the platen temperature.

A RADIUS injection pump was used to preheat and deliver the PR-500 epoxy resin at a constant flow rate. The pump was a piston-type pump capable of pumping up to 2100

cc of resin continuously at a rate of 150 cc/min. and maintaining a constant resin temperature of up to 177 °C. The maximum injection pressure possible was 827 kPa.

The LabVIEW data acquisition system described in Chapter 2 was used to monitor mold temperatures and pressures. The system was configured to monitor up to six channels of analog data.

A system developed by the College of William and Mary was used to measure the output from up to six in situ FDEMS sensors [37]. These sensors were developed to monitor capacitance and conductance of thermoset resins. The output was used to indicate the wet-out time at each FDEMS sensor location.

## 5.4 Test Descriptions

A summary of the test parameters is presented in Table 5-1. The tests completed include one perimeter injection and two center port injection experiments. A detailed description of the individual tests is given.

### 5.4.1 Test 1, Perimeter Injection

A 16 ply, 30.48 cm wide x 30.48 cm long rectangular panel was fabricated from IM7 8HS woven fabric and PR-500 epoxy resin. The warp (0°) direction was aligned parallel to the front edge of the mold (see Figure 5-2). The fabric mass was 632.8 g. The fabricated thickness of the panel was measured at five locations (four corners and center) and averaged. The average panel thickness was 0.6142 cm gave a fiber volume fraction of 61.53%. The resin was injected at a constant flow rate of 20 cc/min. and a vacuum was pulled on the outlet to reduce the likelihood of voids and entrapment of air. Lower mold plate LP1 with six FDEMS sensor locations was utilized. Six FDEMS sensors, four thermocouples, and two pressure signals were monitored.

Table 5-1      RTM experiments - test parameters

| Parameter | Test 1 | Test 2 | Test 3 |
|---|---|---|---|
| Injection type | Perimeter | Center Port | Center Port |
| Injection rate | 20 cc/min. | 10 cc/min. | 10 cc/min. |
| Preform material | IM7 8HS | IM7 8HS | IM7 8HS |
| Number of plies | 16 | 16 . | 16 |
| Preform width | 30.48 cm | 30.48 cm | 30.48 cm |
| Preform length | 30.48 cm | 30.48 cm | 30.48 cm |
| Panel thickness | 0.6142 cm | 0.6096 cm | -- |
| Preform mass | 632.8 g | 627.4 g | -- |
| Fiber volume fraction | 61.53% | 61.55% | 61.54% * |
| Permeability, $S_{xx}$ | 5.31e-12 m$^2$ | 5.30e-12 m$^2$ | 5.30e-12 m$^2$ |
| Permeability, $S_{yy}$ | 3.01e-12 m$^2$ | 3.00e-12 m$^2$ | 3.00e-12 m$^2$ |
| Permeability, $S_{zz}$ | 1.71e-13 m$^2$ | 1.70e-13 m$^2$ | 1.70e-13 m$^2$ |
| Mold Temperature | 156 °C | 156 °C | 156 °C |
| Resin Averaged Viscosity | 0.050 Pa-s | 0.058 Pa-s | 0.058 Pa-s |
| Estimated Fill Time ** | 23.31 min. | 41.64 min. | 41.64 min. |

* Average of results from Test A and Test B
** Includes channel surrounding preform and cavity located on upper surface of Picture Frame B used in Test A.

### 5.4.2  Test 2, Center Port Injection

A 16 ply, 30.48 cm wide x 30.48 cm long rectangular panel was fabricated from IM7 8HS woven fabric and PR-500 epoxy resin. The fabric mass was 627.4 g. The fabricated thickness of the panel was measured at five locations (four corners and center) and averaged. The average panel thickness was 0.6096 cm and gave a fiber volume fraction of 61.55%. The resin was injected at a constant flow rate of 10 cc/min. and a vacuum was pulled on the outlet to reduce the likelihood of voids and entrapment of air. The resin was injected through the upper mold plate into the center of the preform. A punch was used to create a 0.635 cm diameter hole in the center of the preform through all plies to reduce the effect of the through-the-thickness permeability and to create a two-dimensional flow pattern. The resin outlet port was located on the side of the picture frame. Lower mold plate LP1 with six FDEMS sensor locations was utilized. Six FDEMS sensors, two thermocouples, and two pressure signals were monitored.

### 5.4.3  Test 3, Center Port Injection

Test 3 was similar to Test 2 with the following exceptions. Lower mold plate LP2 with three FDEMS sensor locations was utilized. Three FDEMS sensors, one thermocouple, and two pressure signals were monitored. Also, the fabric mass and panel thickness measurements were not taken, so the porosity and panel thickness were assumed to be similar to those measured in Test 2.

## 5.5  Finite Element Mesh Generation

Finite element meshes were generated for Test 1 (see Figure 5-5) and Tests 2 and 3 (see Figure 5-6). The finite element meshes generated were quarter models of the entire preform. The warp direction of the preform is oriented with the x-axis for both cases.
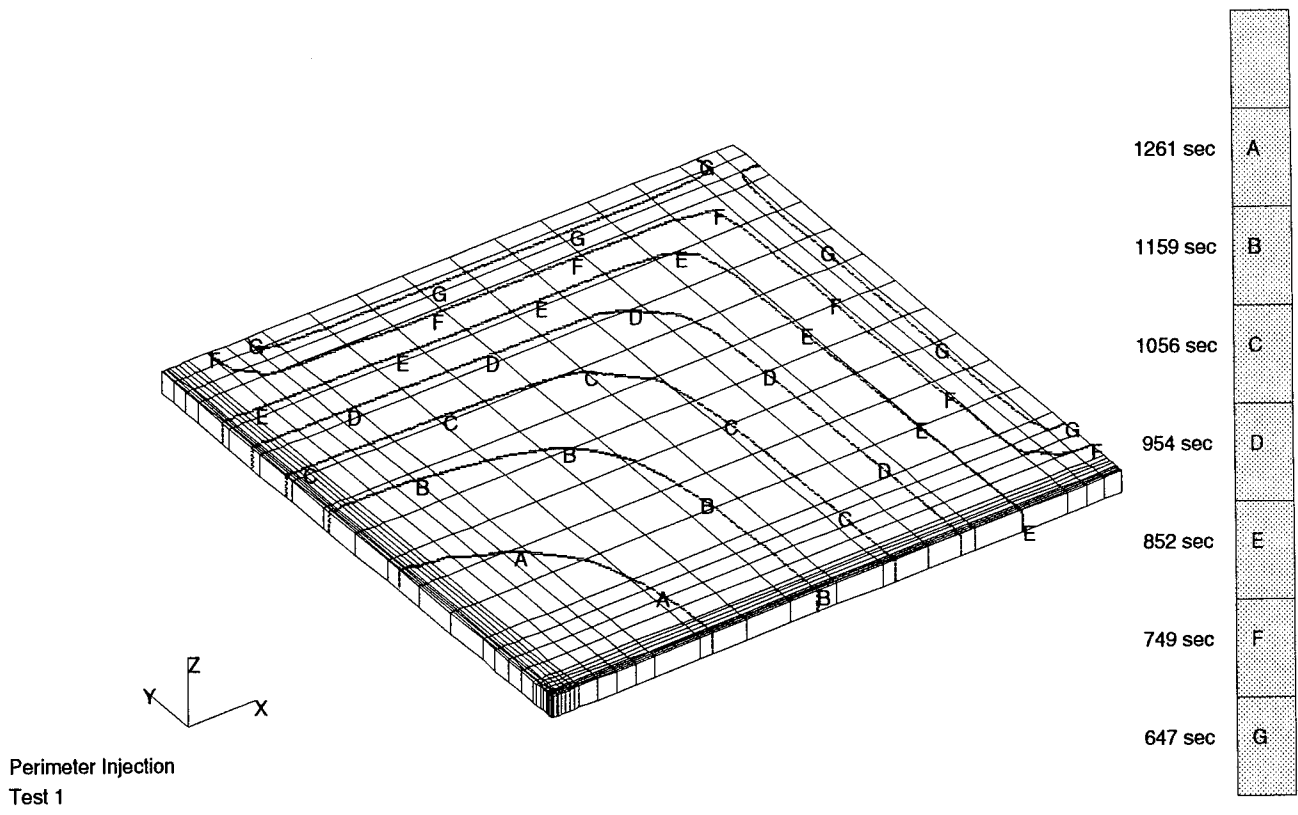
Figure 5-5    Flow front progression at selected time intervals (seconds), Test 1.

| | |
|---|---|
| 2084 sec | A |
| 1764 sec | B |
| 1443 sec | C |
| 1122 sec | D |
| 802 sec | E |
| 481 sec | F |
| 160 sec | G |

Center-port Injection
Tests 2and 3
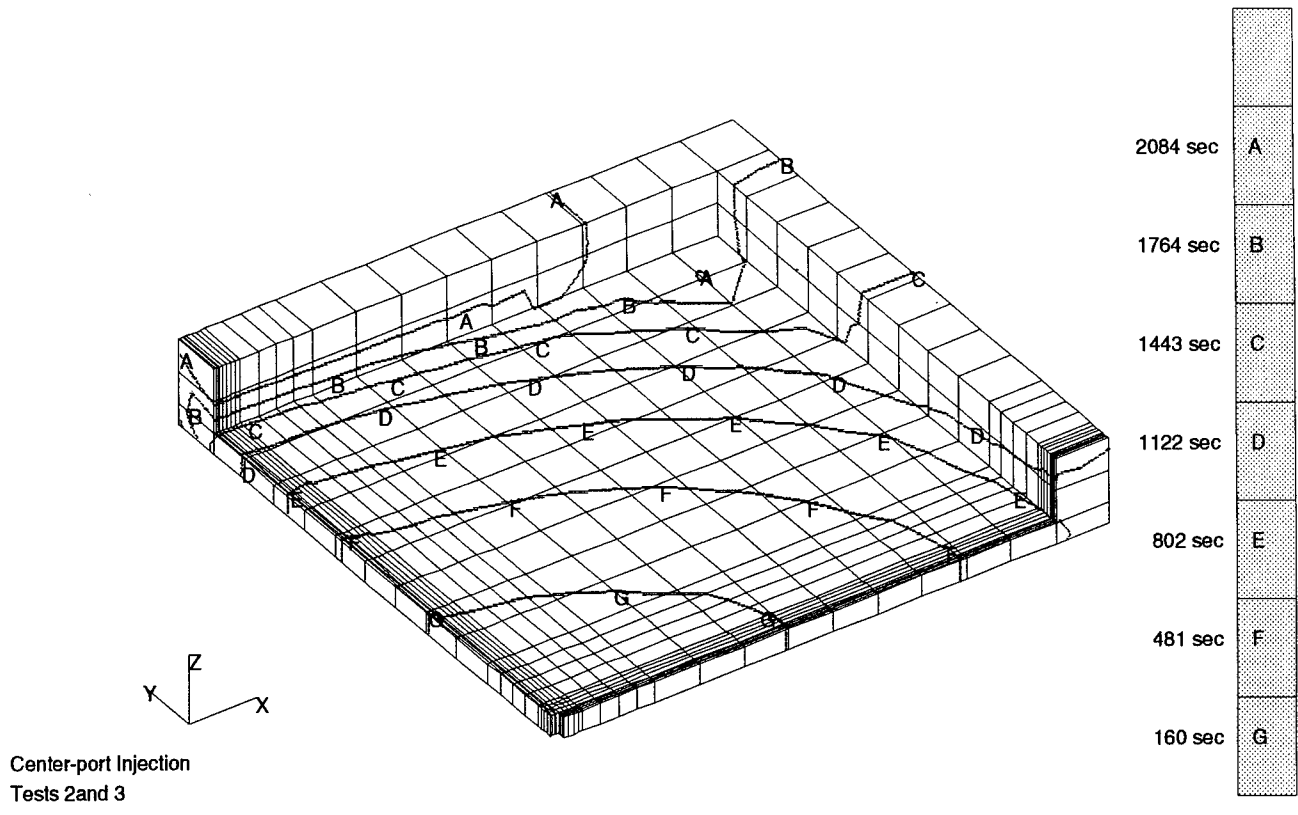
Figure 5-6    Flow front progression at selected time intervals (seconds), Tests 2 and 3.

The assumption was made for Test 1 that the resin is uniformly distributed around the edge of the preform. The cylindrical groove along the top of picture frame PF2 (see Figure 5-4) and the channel around the perimeter of the spacer plate were not included in the mesh. The version of the FEM solver used did not allow for inlet flow rate boundary conditions to be prescribed to elements with different surface areas. Therefore, the constant flow rate boundary condition was applied only to the faces of the eighteen largest elements on the outer edges of the model (see Figure 5-5). The first three rows of elements on the two outer edges of the mesh surrounding the preform were then assigned a high permeability ($1.0e-9$ m$^2$) to ensure that the flow front was uniformly distributed around the edge of the preform before impregnation of the preform began. The circular resin outlet had to be approximated as a square port since only orthogonal, hexagonal elements are allowed. Hence, the outlet was modeled as a 0.498 cm x 0.498 cm surface at the center of the upper surface of the preform. The mesh generated for Test 1 contained 576 elements and 1250 nodes.

The mesh generated for Tests 2 and 3 includes the 0.635 cm wide channel surrounding the preform and spacer plate. The channel region was modeled as an area of high permeability ($1.00e-9$ m$^2$), to approximate a viscous flow through an open channel. Since the version of the FEM solver used did not allow the input of regions with differing porosities, the width of the channel region was increased to account for the 100% porosity of the channel. Again, the 0.635 cm diameter cylindrical inlet geometry was approximated by a 0.498 cm x 0.498 cm square inlet port to maintain the same surface area at the resin inlet. The mesh generated for Tests 2 and 3 contained 554 elements and 1202 nodes.

The boundary conditions enforced for both meshes were zero flow rate normal to all surfaces except the inlet, and constant flow rate at the inlet. The initial condition prescribed is zero pressure at all nodes except for the nodes on the surface of the inlet where the pressure is not specified due to the constant velocity condition. Also, for Test 1 a pressure sink is prescribed at the nodes on the .498 cm x .498 cm outlet surface at the center of the preform and the flow rate boundary condition is removed.

## 5.6 Results

### 5.6.1 Perimeter Injection

It is noted that the temperature of the panel perimeter and the panel center (see Figure 5-7) maintained a constant temperature throughout the process. The calculated isothermal viscosity varies from 0.047 to 0.057 Pa-s (see Figure 4-10), with an average viscosity of 0.050 Pa-s during the mold filling process. Since the mold temperature is constant and the viscosity variation is small, the simplification of constant viscosity for the process model was considered valid.

Since the assumption was made that the resin is evenly distributed around the edge of the preform for Test 1, predicted wet-out times could not be determined at sensor locations 3A, 5A, and 6A at the edges of the preform (see Figure 5-3). Therefore, only wet-out times measured by the three FDEMS sensors located beneath the preform are compared with model predictions (see Figure 5-8). The average percent difference between the measured and calculated wet-out time was 15%. From the inlet pressure results (see Figure 5-9), it is noted that complete mold fill occurred at approximately 22 minutes. Since the wet-out time measured at FDEMS sensor 1A was three minutes greater than the mold fill time, it is possible that the FDEMS sensors do not always wet out immediately as the flow front passes over the resin sensing port.

The measured and calculated inlet pressure curves matched fairly well (see Figure 5-6). The inlet pressure was measured in the perimeter surrounding the preform, and a 40 kPa pressure level was measured prior to the beginning of preform wet-out. This pressure was not predicted by the model. It is possible that the 40 kPa pressure offset is due to air pressure being built up in the cavity surrounding the spacer plate (see Figure 5-4). Once the resin fills the cavity surrounding the preform and spacer plate past the height of the preform, the air is not able to vent through the porous preform and must be forced into the preform or stay in the gap surrounding the preform. This pressure difference would also account for the early wet-out of FDEMS sensors 2A and 4A.
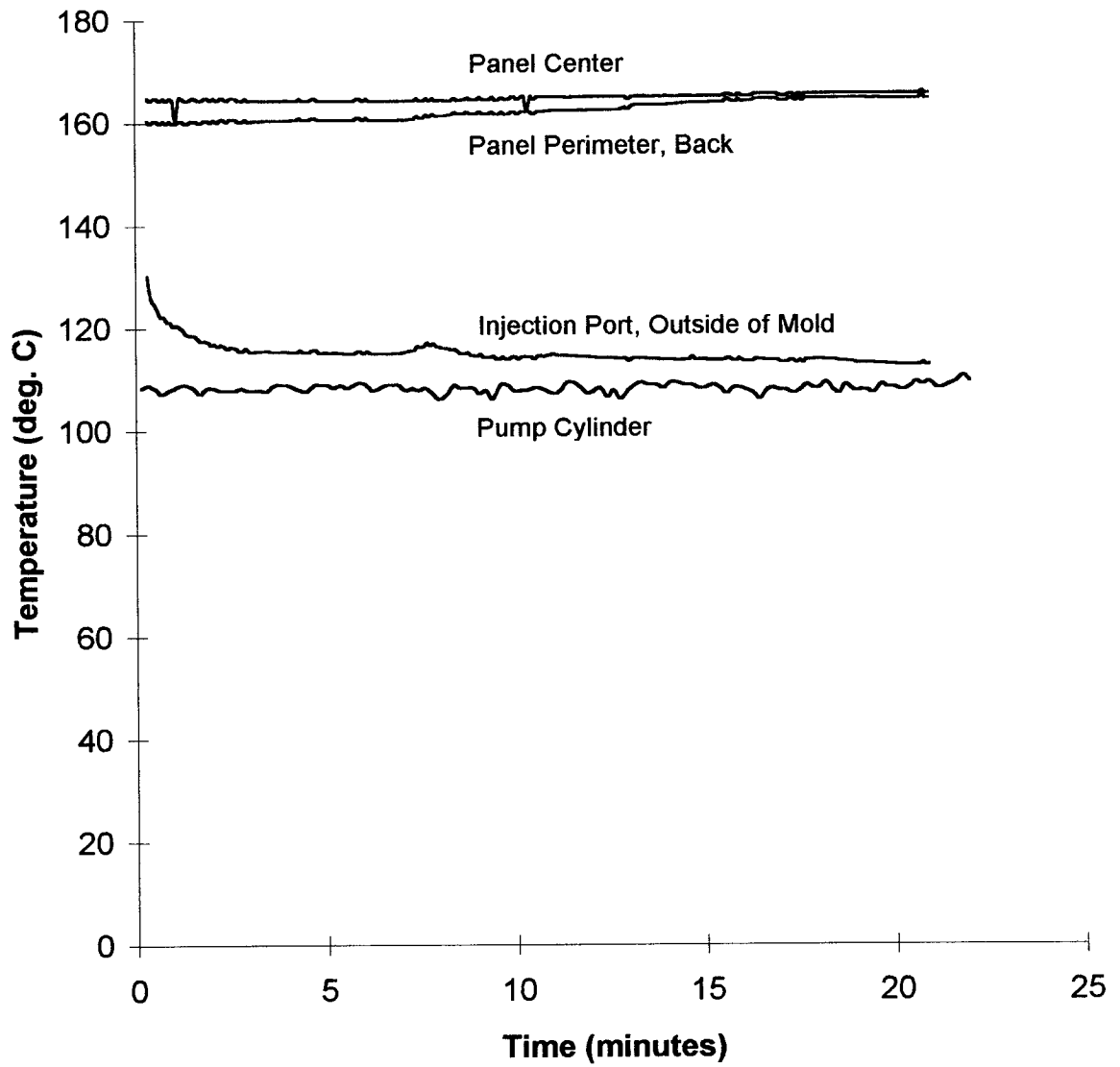
Figure 5-7    Experimental temperatures versus time, Test 1.
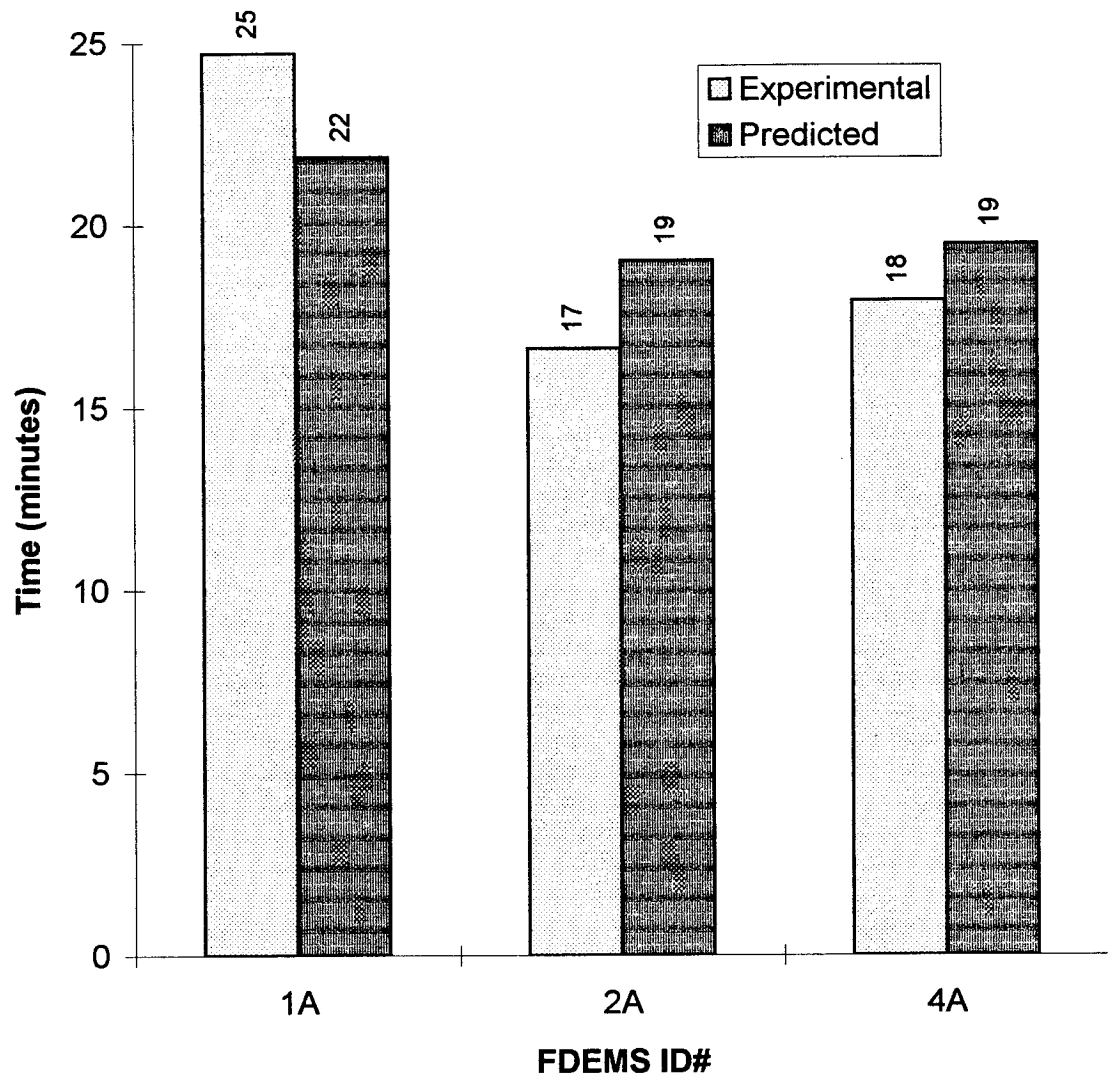
Figure 5-8    Experimental and predicted wet-out times at FDEMS sensor locations, Test 1.
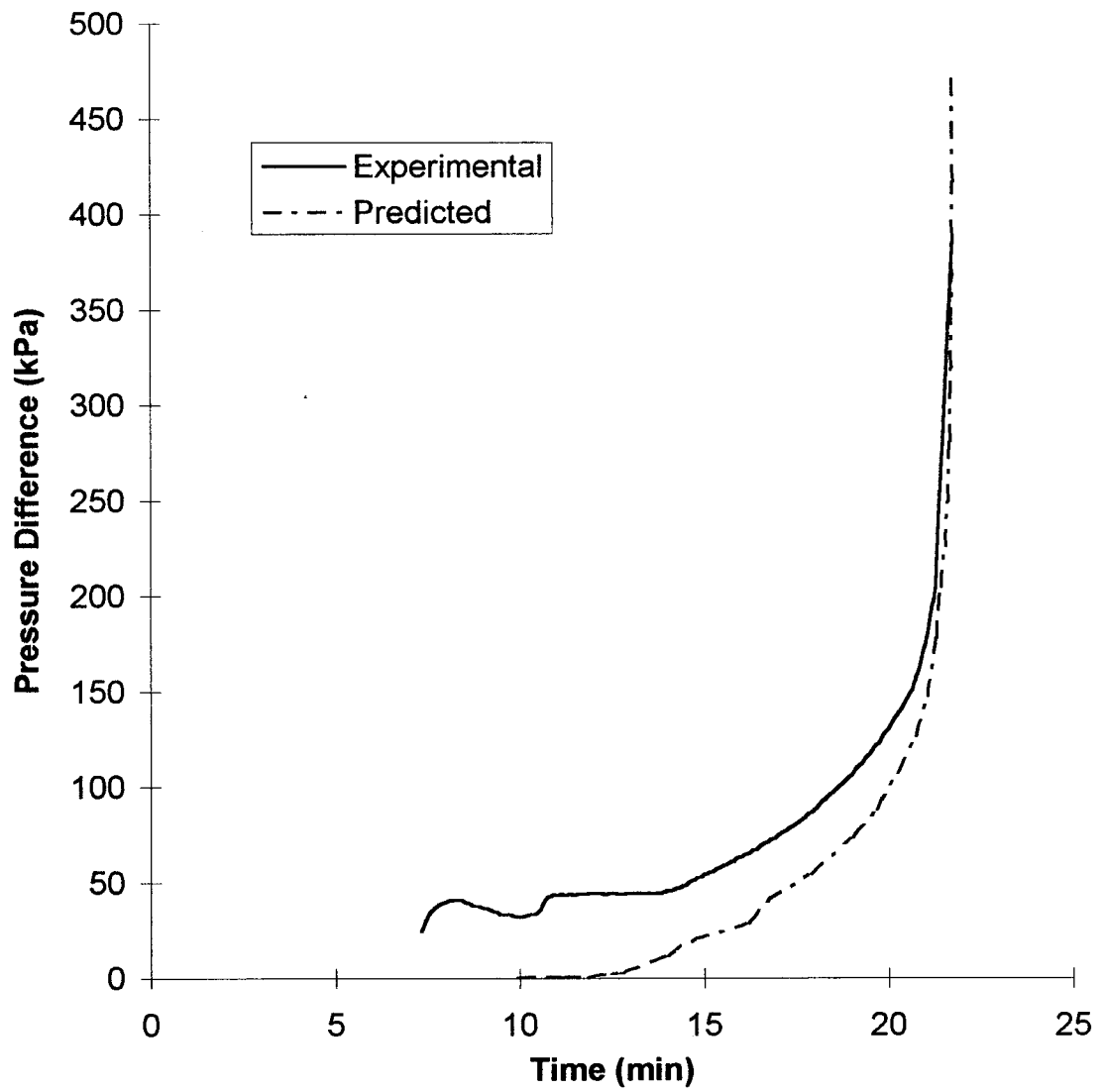
Figure 5-9    Experimental and predicted inlet pressure versus time, Test 1.

The impact of the pressure drop from the Poiseuille pipe flow through the 0.63 cm diameter x 17.0 cm long inlet port located in the upper mold plate was studied. It was calculated to be 0.06 kPa, and therefore had a negligible effect on the results.

## 5.6.2 Center-Port Injection

It is noted that again the temperature of the panel perimeter and the panel center (see Figure 5-10) maintained a constant temperature throughout the process. The calculated isothermal viscosity varies from 0.047 to 0.087 Pa-s. The calculated average viscosity during the mold filling cycle is 0.058 Pa-s. Therefore, the majority of the viscosity rise takes place during a short time at the end of the mold filling cycle. The simplification of constant viscosity for the process model is considered valid for the first half of the processing cycle, but can cause an underprediction of mold pressures during the latter part of the processing cycle.

The measured inlet pressures were significantly higher than those predicted by the model (see Figure 5-11). Possible causes for the difference in inlet pressure are as follows:

- Deformation of the fibers at the inlet caused by the punch used to create the 0.32 cm diameter hole.

- Discrepancies between actual and measured permeabilities

The predicted wet-out times and the FDEMS measured times for Tests 2 (FDEMS ID# 2A-6A) and 3 (FDEMS ID# 2B-3B) are presented in Figure 5-12. The FDEMS measured wet-out times did not correlate well with the predicted times. Sensors 4A and 3B did not wet out at all. Two sensors at the perimeter of the preform (3A and 6A) wet out earlier than predicted by the model, and the rest of the sensors had a delayed wet-out. It is possible that a resin path was created by the thermocouple wire, allowing for premature wet-out of the sensors at the perimeter, with the exception of 5A. The delayed wet-out of many of the FDEMS sensors along with the lack of wet-out of two FDEMS sensors supports the possibility that the pressures in the were not high enough to quickly wet out the sensors located in the cavities in the lower mold plate.
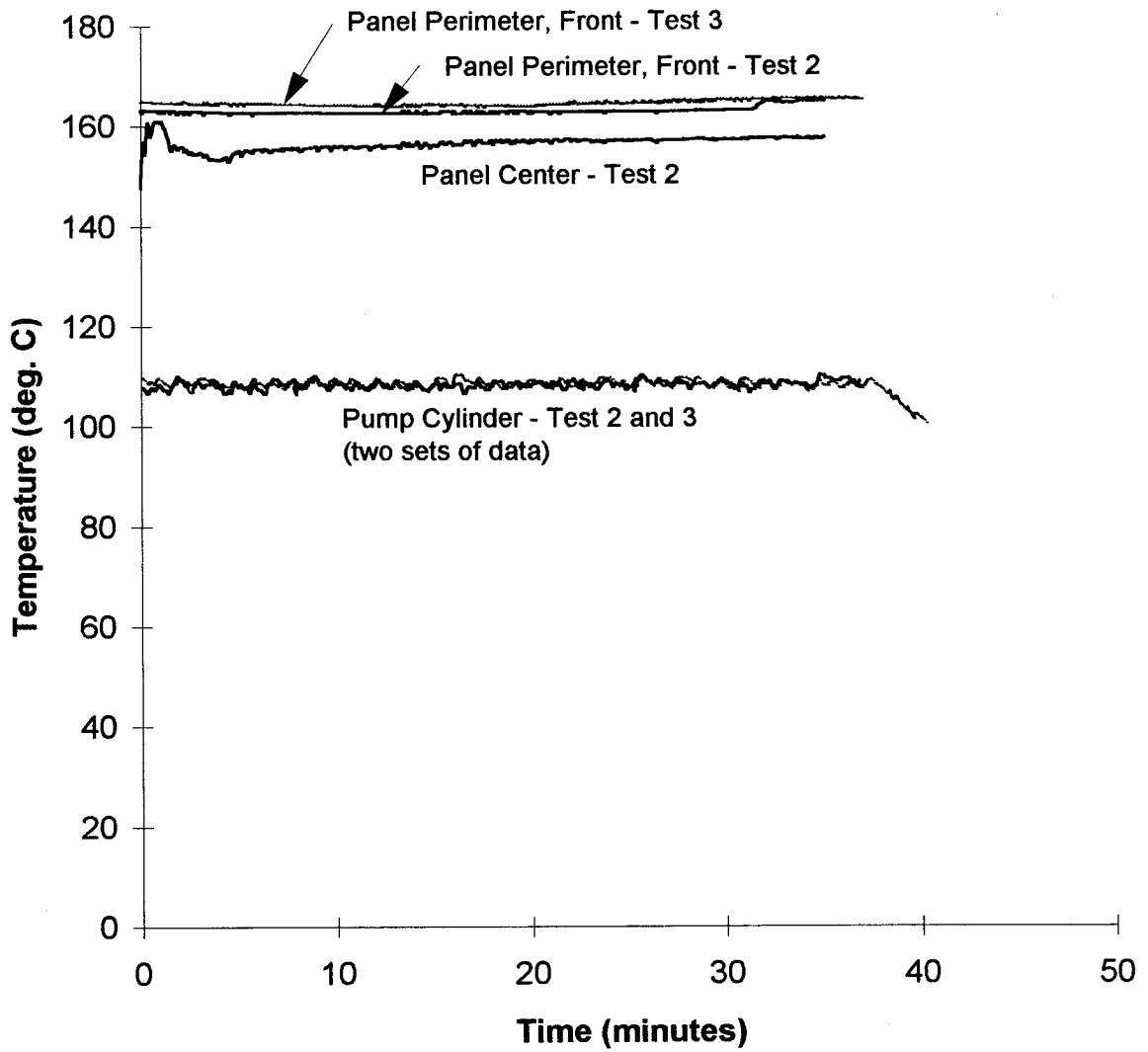
Figure 5-10    Experimental temperatures versus time, Tests 2 and 3.
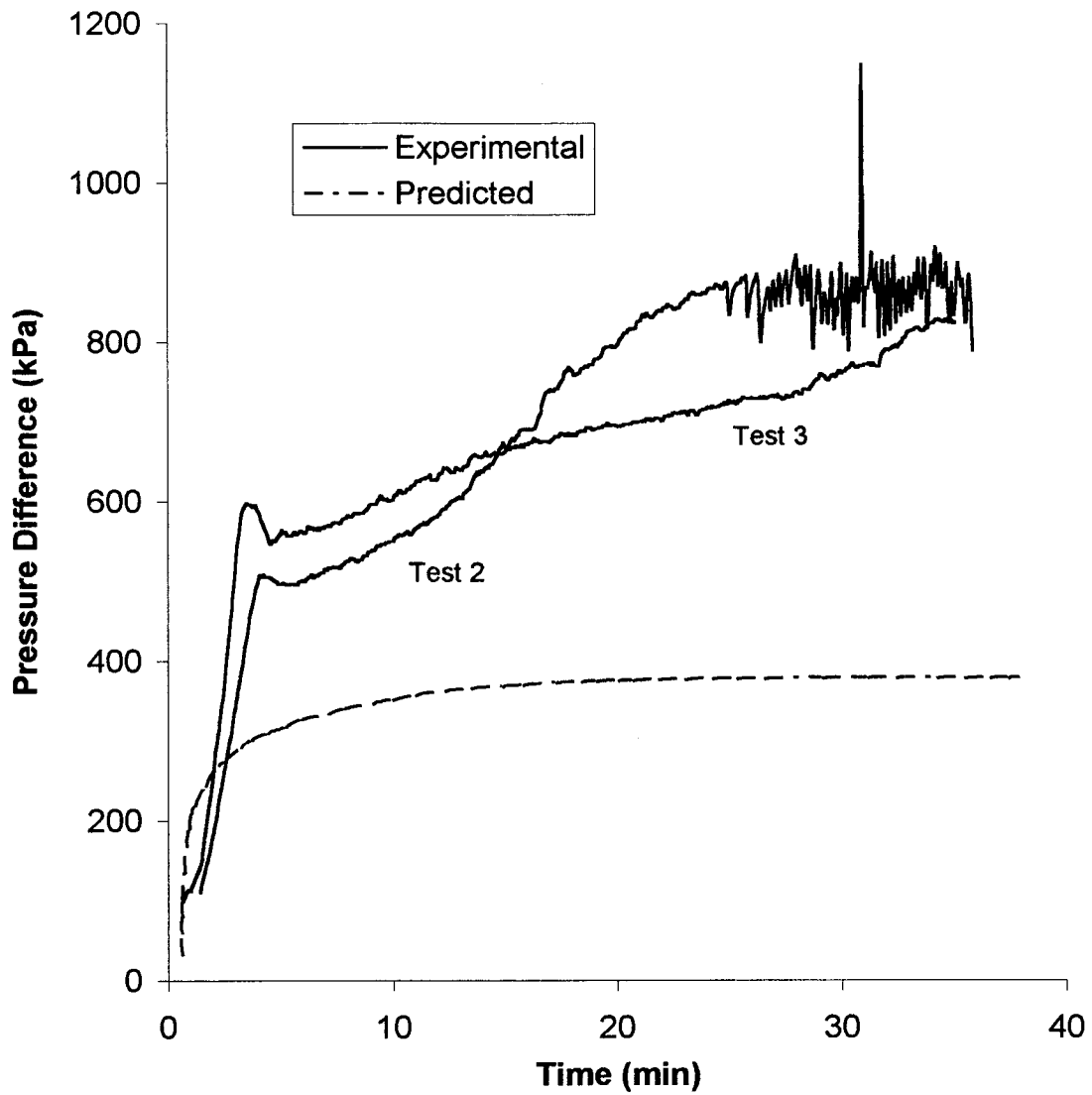
Figure 5-11    Experimental and predicted inlet pressure versus time, Tests 2 and 3.
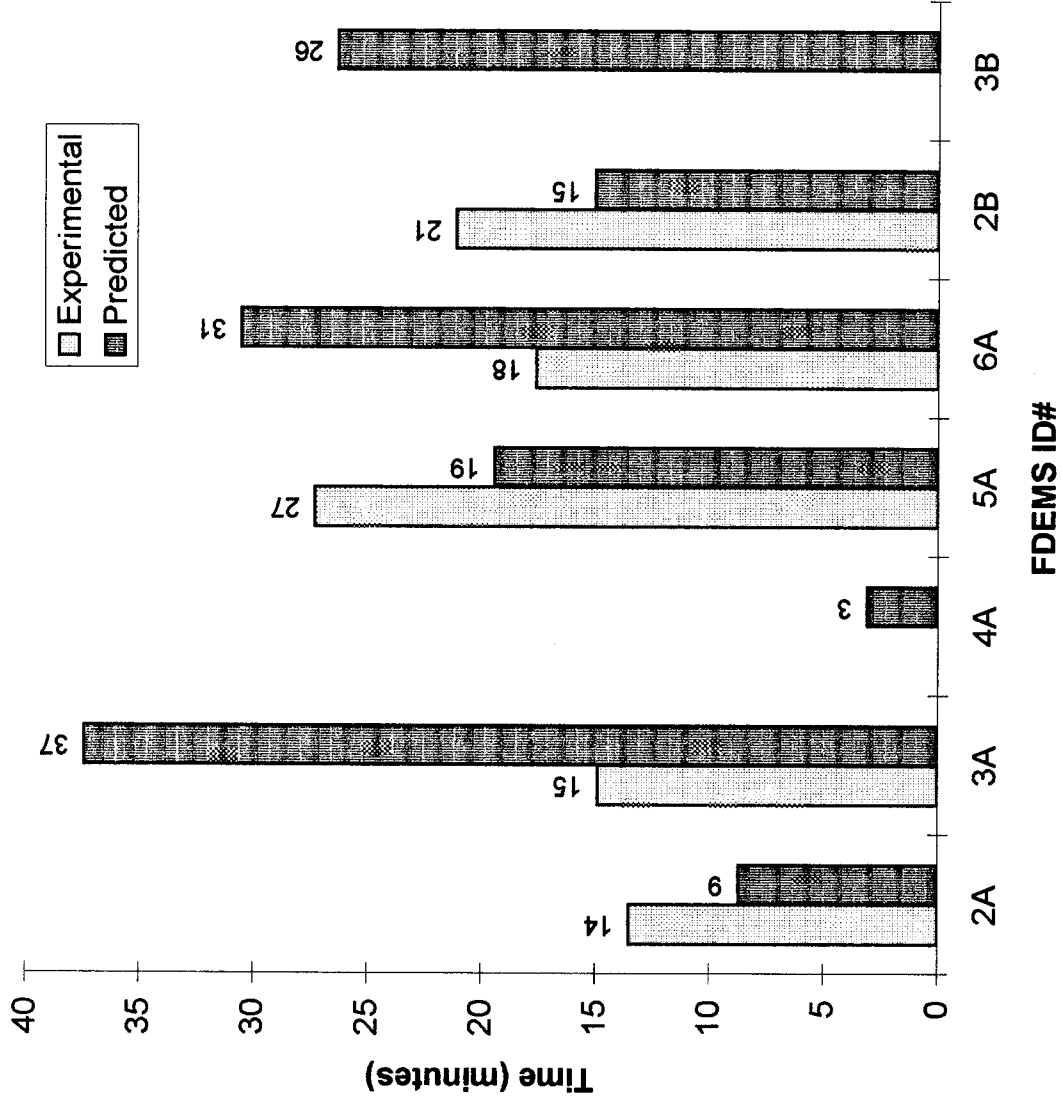
Figure 5-12   Experimental and predicted wet-out times at FDEMS sensor locations, Tests 2 and 3.

# 6. Conclusions and Future Work

## 6.1 Conclusions

The focus of this research was to verify a RTM process simulation model which was solved by the Finite Element/Control Volume technique. The program required measuring the permeability and compaction characteristics of the preform and cure kinetics and viscosity of the resin. The flow of resin through a blade-stiffened preform was measured with flush-mount pressure transducers and the results were compared to model results. Finally, flat panels were fabricated by Resin Transfer Molding in an instrumented mold. The instrumentation included pressure transducers, thermocouples, and FDEMS sensors to monitor the process. The data was compared to FEM results.

### 6.1.1 Permeability Measurement

A system capable of real-time, in-plane advancing front permeability as well as steady-state permeability measurements of thick, high fiber volume fraction preforms has been developed. The fixture permeability measurements have been verified with results from Virginia Tech Fixture B using both Style 162 E-glass and IM7/8HS fabric.

Verification of the use of pressure transducers as an indicator of flow front position has been completed.

The advancing front permeability has been shown to closely match the steady-state permeability for Style 162 E-glass at a fiber volume fraction of 55%. The interstitial velocity calculated from the pressure taps was slower than the actual averaged velocity calculated from the inlet flow rate. This indicates that edge effects are noticeable and create a two-dimensional flow pattern.

A method has been developed to measure the principal directions and permeabilities as a function of fiber volume fraction of a preform. Results obtained from an 81-ply multi-axial warp knit preform showed the principal axes are nearly aligned with the directions parallel and normal to the stitching.

The permeabilities and compaction characteristics of materials which are components of a blade-stiffened preform have been fully characterized. Comparison of the 9-ply multi-axial warp knit subgroup with a stitched 54-ply multi-axial warp knit preform shows that the permeability normal to the stitching direction of the sub-ply decreases dramatically when stitched. Also, the normal to the stitching permeability is lower than the parallel to stitching permeability in both the sub-ply material and the fully stitched warp-knit preform.

## 6.1.2 Blade-stiffened preform experimental and FEM flow results

The mold filling process, governed by Darcy's law, was modeled and measured for a blade-stiffened preform comprised of permeable materials assumed to be orthotropic. The model calculated inlet pressures were approximately 50% of the experimental values and the average error in wet-out times at selected locations was 24%.

A parametric study was performed to assess the result of changing individual permeability values for the different regions of the blade-stiffened preform on the wet-out times and inlet pressure. The results showed that the maximum reduction in average error in wet-out times was reduced to 12%. Also, the inlet pressure curve increased to approximately 65% of the experimentally determined pressure curve. It was shown that a reduction in any one of the permeability values to 25% of the original value incorporated in the model was not sufficient to raise the predicted inlet pressure to the measured values.

In addition to the parametric study, simulations were run to study the effect of changes in the fiber volume fraction in the wing skin located directly under the blade. It was found that an increase in fiber volume fraction from 55 to 62% resulted in a reduction in average error of normalized wet-out times from 24% to 12%, and increased the magnitude of the inlet pressure to approximately the measured value.

### 6.1.3 Cure kinetics results

The combined autocatalytic/nth order cure kinetics model developed by Kamal et. al. [30] was used to characterize PR-500 epoxy resin. Isothermal DSC data along with residual dynamic scans were completed to determine the kinetic parameters. It was shown that the model fits the experimental data well, and the kinetics model was able to accurately predict the degree of cure for an arbitrary ramp-hold sequence.

### 6.1.4 Viscosity model results

An empirical viscosity model was fit to isothermal viscosity data of PR-500 epoxy resin. The degree of cure at gel was determined to be a linear function of temperature, and these results were incorporated into the viscosity model. The model fits the data fairly well at low temperatures and degree of cure. High temperature data following the onset of gelation did not match the calculated viscosity as well.

### 6.1.5 RTM process modeling results

Results from perimeter injection tests correlated well with model results. The initial resin inlet pressure was higher than predicted by the RTM model and is possibly caused by air trapped in the mold cavity. Center-port injection results did not match well with FEM results. The inlet pressure was predicted to be only 50% of the measured inlet pressure. Also, the RTM simulation model predicted and measured FDEMS sensor wet-out times did not agree well. This is believed to be caused by the delay in resin passing through the hole located between the FDEMS sensor and the preform. It is also aggravated by the lower mold pressures inherent to center-port injection.

131

## 6.2 Future Work

### 6.2.1 Future Permeability Characterization

Characterization of the non-homogeneity of the preform material and its effects on permeability variance is a topic which is of interest. Since material characteristics can change both from lot to lot and within a batch, the effect of these parameters should be studied. The results would give confidence to the limits put on permeabilities used to complete modeling of molding processes.

A study of the effects of two-dimensional flow front velocity profiles caused by the boundary heterogeneities on permeability calculations should be undertaken. Methods to reduce the likelihood of the edge effect during measurements or methods to account for it are needed to ensure accurate results.

Further investigation of the principal axes of preform materials fabricated using different manufacturing techniques should be completed. The principal permeabilities and directions of the 9-ply subgroups for the multi-axial warp knit material should be characterized and compared to the stitched multi-axial warp knit preform principal permeabilities and directions. This work along with the characterization of stitching effects currently being completed at Virginia Tech would give experimental evidence for models of complex preforms based on the characteristics of the base materials and manufacturing techniques.

### 6.2.2 Recommended permeability fixtures

It is recommended that an in-plane radial fixture with adjustable fiber volume fraction be incorporated into the existing die set. Using pressure transducers for flow front position indication and with previous knowledge of principal directions gained from VT Fixture C, the investigator would be able to determine permeabilities accurately. This information would aid in the characterization of the effect of boundary heterogeneities on permeability measurement. Further, it is recommended that the current transverse

permeability Fixture A be incorporated into the existing die set to take advantage of the LVDT feedback.

## 6.2.3  Recommended permeability fixture fabrication methods

Suggested modifications for future fixtures would be as follows:

- Cylinder material should be a through-hardened tool steel. The steps to take to build the cylinder should be:
    - Pre-machine outer dimensions and bolt holes
    - Drill starter hole for wire EDM for both cavity and dowel pin holes
    - Through-harden
    - Wire EDM cavity and dowel pin holes
    - Grind or EDM O-ring starting groove on CNC equipment
    - Coat w/ Armalloy™ coating to protect from oxidation
- Building material for other components of the fixture should be stainless steel. This eliminates coating cost, and allows for future modifications to be made to fixture components without removing the coating. Also, coating is limited in its depth of penetration in deeper grooves.

Outer dimensions of piston tip should be wire EDM'd or ground on CNC equipment to accurately match dimensions of piston and cylinder.

## 6.2.4  Future blade-stiffened flow fixture work

It is recommended that more tests be run to understand the reasons for a mismatch in experimental and FEM results. The one-dimensional permeabilities input into the flow model should be more thoroughly measured from material of the same batch as that used in the flow fixture. If enough material is made available, a study of the experimental error in permeability measurement including the effect of material inhomogeneities would be possible.

An attempt to measure the fiber volume fraction or to ensure a constant fiber volume fraction of the wing skin directly under the blade should be made. Work should be

done to understand the effects of the nonhomogeneities of the region between the blade and the wing skin, and influenced by the continuous strand rovings.

Finally, it is recommended that similar flow studies be completed which involve conditions more similar to those seen during manufacturing. These include introduction of vacuum both to compress the fabric and to reduce voids, and non-isothermal injection of resin by the resin film infusion technique.

## 6.2.5 Recommended flow fixture fabrication modifications

Modifications to be made when manufacturing future flow fixtures are recommended:

- Mold should be built with closed edges and not necessarily with the ability to test multiple volume fractions.
- Ability to introduce vacuum is desirable to reduce chance of trapped air.
- Ability to introduce flow front from edge face to obtain two-dimensional results from same fixture.

## 6.2.6 Future resin characterization work

The cure kinetics model should be experimentally verified by data other than DSC data. Furthermore, a dynamic viscosity test should be run to see whether the viscosity model can also predict dynamic data. If possible, more isothermal viscosity data should be taken for the PR-500 to check the accuracy of the original viscosity data at 160C.

## 6.2.7 Future RTM process modeling

It is recommended that more work be completed in flat panel processing and instrumentation of the molds to better verify the modeling. In order to instrument molds, it is recommended that thermocouples be routed into the mold and preform via the upper or lower mold plates, instead of the picture frame. This would reduce the level disruption of the flow pattern from the T/C wires. In addition, high temperature pressure transducers should be introduced as in-mold sensors and placed on the upper or lower mold plates.

These would be able to verify both flow front position data from the FDEMS sensors, and also measure in-mold pressures. It is recommended to use pressure transducers similar to the Entran EPX series to minimize disruption of flow front patterns. Finally, the ability to offset the pressure transducer tip from the face of the mold would allow verification of resin pressures only.

A method of mounting the FDEMS sensors in direct contact with the panel would be beneficial. This would reduce the time lag for the resin to travel through the drilled hole located between the FDEMS sensor and the panel. It is recommended that FDEMS sensors not be located directly at the edge of the preform adjacent to the surrounding resin channel. If the preform shifts a small amount, the time measured for wet-out of the sensor can shift dramatically.

The following change in the test method is recommended. The hole punched in the center of the preform for the center port injection case can cause deformation of the fibers, having an unknown effect on permeability. Since modeling can account for the through-the-thickness flow of resin, it is recommended not to remove the fabric with a punch.

Isothermal center-port injection tests using non-reactive fluids should be completed to better understand the mismatch in inlet pressure.

# References

[1] Macrae, J.D. "Development and Verification of a Resin Film Infusion/Resin Transfer Molding Simulation Model for Fabrication of Advanced Textile Composites." Master's Thesis, Virginia Polytechnic Institute and State University, 1994.

[2] Darcy, H. Les Fontaines Publiques de la Villa de Dijon. Dalmount: 1856.

[3] Adams, K.L., Rebenfield, L., "Permeability Characteristics of Multilayer Reinforcements. Part 1: Experimental Observations." Polymer Composites, Vol. 12, No. 3 (June 1991): pp. 179-185.

[4] Sadiq, T., Parnas, R., Advani, S. "Experimental Investigation of Flow in Resin Transfer Molding." 24th International SAMPE Technical Conference, October 20-22, 1992. pp. 660-T674.

[5] Gebart, B.R. "Permeability of Unidirectional Reinforcements for RTM." Journal of Composite Materials, Vol. 26, No. 8 (1992): pp. 1100-1133.

[6] Cai, Z., Berdichevsky, A.L. "Estimation of the Resin Flow Permeability of Fiber Tow Preforms Using the Self-Consistent Method." Polymer Composites, Vol. 15, No. 3, (June 1994): pp. 24-246.

[7] Parnas, R.S., Phelan, Jr., F.R. "The Effects of Heterogeneities in Resin Transfer Molding Preforms on Mold Filling." 36th International SAMPE Symposium, Vol. 36, No. 1 (April 15-18, 1991): pp. 506-520.

[8] Hammond, V.H. "Verification of a Two-Dimensional Infiltration Model for the Resin Transfer Molding Process." Master's Thesis, Virginia Polytechnic Institute and State University, 1993.

[9] Kim, Y.R., Mcarthy, S.P., Fanucci, J.P., Nolet, S.C., Koppernaes, C. "Resin Flow Through Fiber Reinforcements During Composites Processing." Proceedings of the 22nd International SAMPE Technical Conference, SAMPE, Covina, CA, (1990): pp 709-723.

[10] Weideman, M.H. "An Infiltration/Cure Model for Manufacture of Fabric Composites by the Resin Infusion Process." Master's Thesis, Virginia Polytechnic Institute and State University, 1992.

[11] Chan, A.W., Larive, D.E, Morgan, R.J. "Anisotropic Permeability of Fiber Preforms: Constant Flow Rate Measurement." Journal of Composite Materials, Vol. 27, No. 10 (1993): pp. 996-1008.

[12] Wang, T.J., Wu, C.H., Lee, L.J. "In-plane Permeability Measurement and Analysis in Liquid Composite Molding" Polymer Composites, Vol. 15, No. 4 (August 1994): pp. 278-288.

[13] Trevino, L., Rupel, K., Young, W.B., Liou, M.J., Lee, L.J., "Analysis of Resin Injection Molding in Molds with Preplaced Fiber Mats. I: Permeability and Compressiblity Measurements." Polymer Composites, Vol. 12, No. 1 (February 1991): pp. 20-29.

[14] Wu, C.H., Wang, T.J., Lee, L.J. "Trans-plane Fluid Permeability Measurement and its Application in Liquid Composite Molding." Polymer Composites, Vol. 15, No. 4, (August 1994): pp. 289-298.

[15] Ahn, S.H., Lee, W.I., Springer, G.S. "Measurement of Three-dimensional Permeability of Fiber Preforms Using Embedded Fiber Optic Sensors." Journal of Composite Materials, Vol. 29, No. 6 (1995): pp. 714-732.

[16] Deaton, J.W., Dexter, H.B., Markus, A., Rohwer, K. "Evaluation of Briaded Stiffener Concepts for Transport Aircraft Wing Structure Applications." Fifth NASA/DOD Advanced Composites Technology Conference, August 22-25, 1994.

[17] Mendenhall, W. "Introduction to Linear Models and the Design and Analysis of Experiments." Wadsworth Publishing Co, California, 1968.

[18] Um, M.K., Lee, W.I., "Numerical Simulation of the Resin Transfer Molding Process Using Boundary Element Methods." Proceedings of the 35th International SAMPE Symposium, (1990): pp. 1905-1916.

[19] Coulter, J.P., Guceri, S.I. "Resin Impregnation During the Manufacturing of Composite Materials Subject to a Prescribed Injection Rate." Journal of Reinforced Plastics and Composites, Vol. 7, No. 3 (May 1988): pp. 200-219.

[20] Gauvin, R., Trochu, F. "Comparison Between Numerical and Experimental Results for Mold Filling in Resin Transfer Molding." Plastics, Rubber, and Composites Processing and Applications, Vol. 19, No. 3, (1993): pp. 151-157.

[21] Boccard, A., Lee, W.I., Springer, G.S. "Model for Determining the Vent Locations and the Fill Time of Resin Transfer Molds." Journal of Composite Materials, accepted for publication.

[22] Young, W.B., Rupel, K., Han, K., Lee, L.J., Liou, M.J. "Analysis of Resin Injection Molding in Molds with Preplaced Fiber Mats. II: Numerical Simulation and Experiments of Mold Filling." Polymer Composites, Vol. 12, No. 1 (Feb. 1991): pp. 30-38.

[23] Frachia, C.A., Castro, J., Tucker, C.L. "A Finite Element/Control Volume Simulation of Resin Transfer Mold Filling." Proceedings of the American Society for Composites, Fourth Technical Conference, (Oct. 3-5, 1989): pp. 157-166.

[24] Wu, C.H., Wang, T.J., Lee, L.J. "Trans-plane Fluid Permeability Measurement and its Application in Liquid Composite Molding." Polymer Composites, Vol. 15, No. 4, (August 1994): pp. 289-298.

[25] Trochu, F., Gauvin, R., Gao, D.M., Boudreault, J. "RTMFLOT - An Integrated Software Environment for the Computer Simulation of the Resin Transfer Molding Process." Journal of Reinforced Plastics and Composites, Vol. 13, No. 3 (March 1994): pp. 262-270.

[26] Muzumdar, S.V., Lee, L.J., "Prediction of Gel-Time in the Cure of Unsaturated Polyester Resins: Mechanistic and Statistical Analyses." Society of Plastics Engineers Technical Papers ANTEC '91, Vol. 37 (1991): pp. 737-742.

[27] Martin, J.L., Salla, J.M., "Models of Reaction Commonly Employed in the Curing of Thermosetting Resins." Thermochimica Acta, Vol.207 (1992): pp. 279-304.

[28] Medina Calderon, J.A., Gonzalez-Romero, V.M., Avalos Munguia, T.G., "Phenomenologic Kinetic Models for Polymerization Reaction of Polyester Resin and Styrene, Isothermic and Non-Isothermic, Considering Reaction Times" ANTEC '92 (1992): pp. 1948-1953.

[29] Lam, P.W.K., Plaumann, H.P., Tran, T., "An Improved Kinetic Model for the Autocatalytic Curing of Styrene-Based Thermoset Resins." Journal of Applied Polymer Science, Vol. 41 (1990): pp. 3043-3057.

[30] Kamal, M.R., Sourour, S, Ryan, M., "Kinetics and Thermal Characterization of Thermoset Cure." Polymer Engineering Science, Vol. 13 (1973): pp. 59-64.

[31] Gebart, B.R., "SICOMP/TCV - A Suite of Computer Programs for Material Characterization and Simulation of Cure and Heat Transfer." SICOMP Technical Report 92-008. (April 1992).

[32] Kenny, J.M., Apicella, A., and Nicolais, L., "A Model for the Thermal and Chemorheological behavior of Thermosets. (I): Processing of Epoxy-Based Composites." Polymer Engineering and Science, Vol. 29, No. 15 (1989): pp. 973-983.

[33] Castro, J.M., Macosko, C., "Studies of mold filling and curing in the reaction injection molding process." AICHE Journal, Vol. 28 (1982): pp. 251-260.

[34] Press, W.H., Teukolsky, S.A., Vetterling, W.T., Flannery, B.P., Numerical Recipes in FORTRAN: the Art of Scientific Computing, 2nd ed. (Cambridge: Cambridge University Press, 1992), pp. 678-683.

[35] Kendall, K.N., Rudd, C.D. "Flow and Cure Phenomena in Liquid Composite Molding." Polymer Composites, Vol. 15, No. 5 (October 1994): pp. 334-348.

[36] Loos, A.C., Hammond, V.H., Kranbuehl, D.E., Hasko, G.H. "Verification of a Multidimensional Flow Model for Resin Transfer Molding of Textile Preforms." Fourth NASA/DoD Advanced Composites Technology Conference, NASA-CP-3229, (1993): pp. 299-325.

[37] Loos, A.C., Weideman, M.H., Long, E.R., Kranbuehl, D.E., Kinsley, P.J., Hart, S.M. "Infiltration/Cure Modeling of Resin Transfer Molded Composite Materials Using

Advanced Fiber Architectures" First NASA Advanced Composites Technology Conference, NASA-CP-3104, (1990): pp. 425-442.

# Appendix A   Virginia Tech Fixture C Drawings

Included are the prints used to manufacture the in-plane steady-state/advancing front permeability fixture labelled Virginia Tech Fixture C.
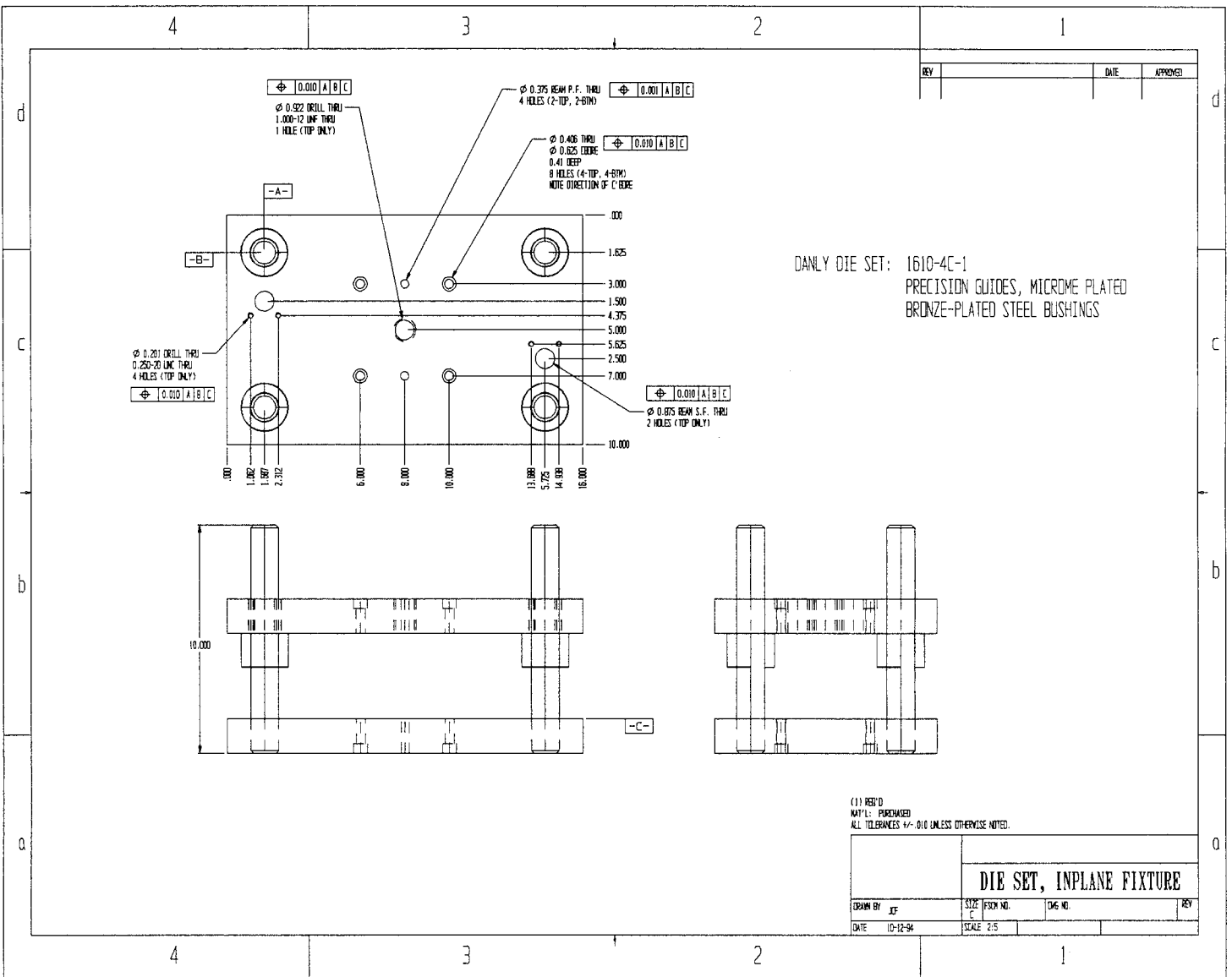
Figure A-1    Danly die set modification, Virginia Tech Fixture C.

Ø 0.375 REAM P.F. THRU
4 HOLES (2-TOP, 2-BTM)

⌖ 0.001 A B C

Ø 0.922 DRILL THRU
1.000-12 UNF THRU
1 HOLE (TOP ONLY)

⌖ 0.010 A B C

Ø 0.406 THRU
Ø 0.625 CBORE
0.41 DEEP
8 HOLES (4-TOP, 4-BTM)
NOTE DIRECTION OF C'BORE

⌖ 0.010 A B C

-A-

-B-

DANLY DIE SET: 1610-4C-1
PRECISION GUIDES, MICROME PLATED
BRONZE-PLATED STEEL BUSHINGS

Ø 0.201 DRILL THRU
0.250-20 UNC THRU
4 HOLES (TOP ONLY)

⌖ 0.010 A B C

⌖ 0.010 A B C

Ø 0.875 REAM S.F. THRU
2 HOLES (TOP ONLY)

.000
1.625
3.000
1.500
4.375
5.000
5.625
2.500
7.000
10.000

.000
1.062
1.687
2.312
6.000
8.000
10.000
13.088
5.725
14.938
16.000

10.000

-C-

(1) REQ'D
MAT'L: PURCHASED
ALL TOLERANCES +/- .010 UNLESS OTHERWISE NOTED.

DIE SET, INPLANE FIXTURE

DRAWN BY   JCF
DATE   10-12-94
SIZE   C   FSCM NO.
SCALE   2:5
DWG NO.
REV

REV          DATE   APPROVED

Figure A-2    Piston, Virginia Tech Fixture C.

143
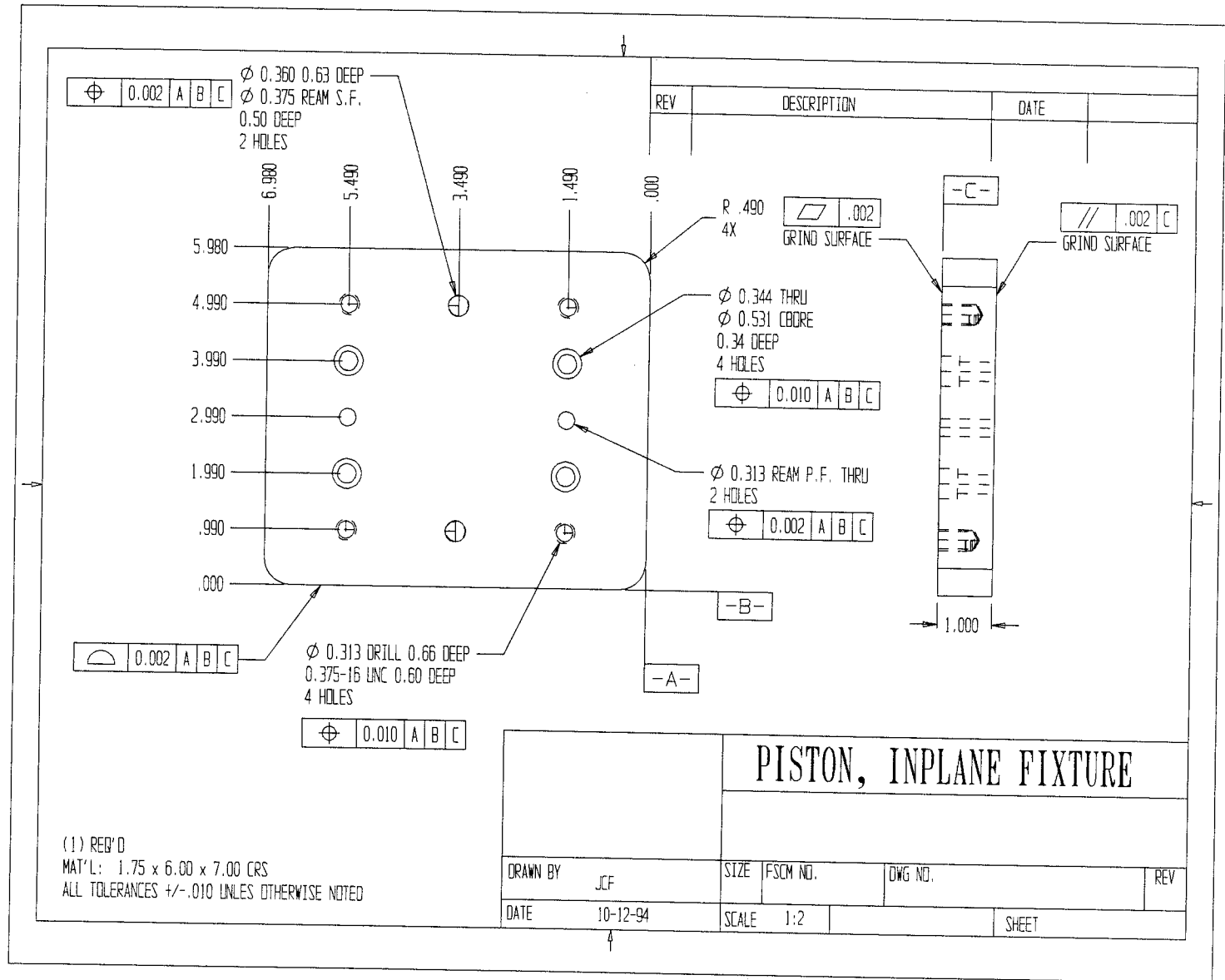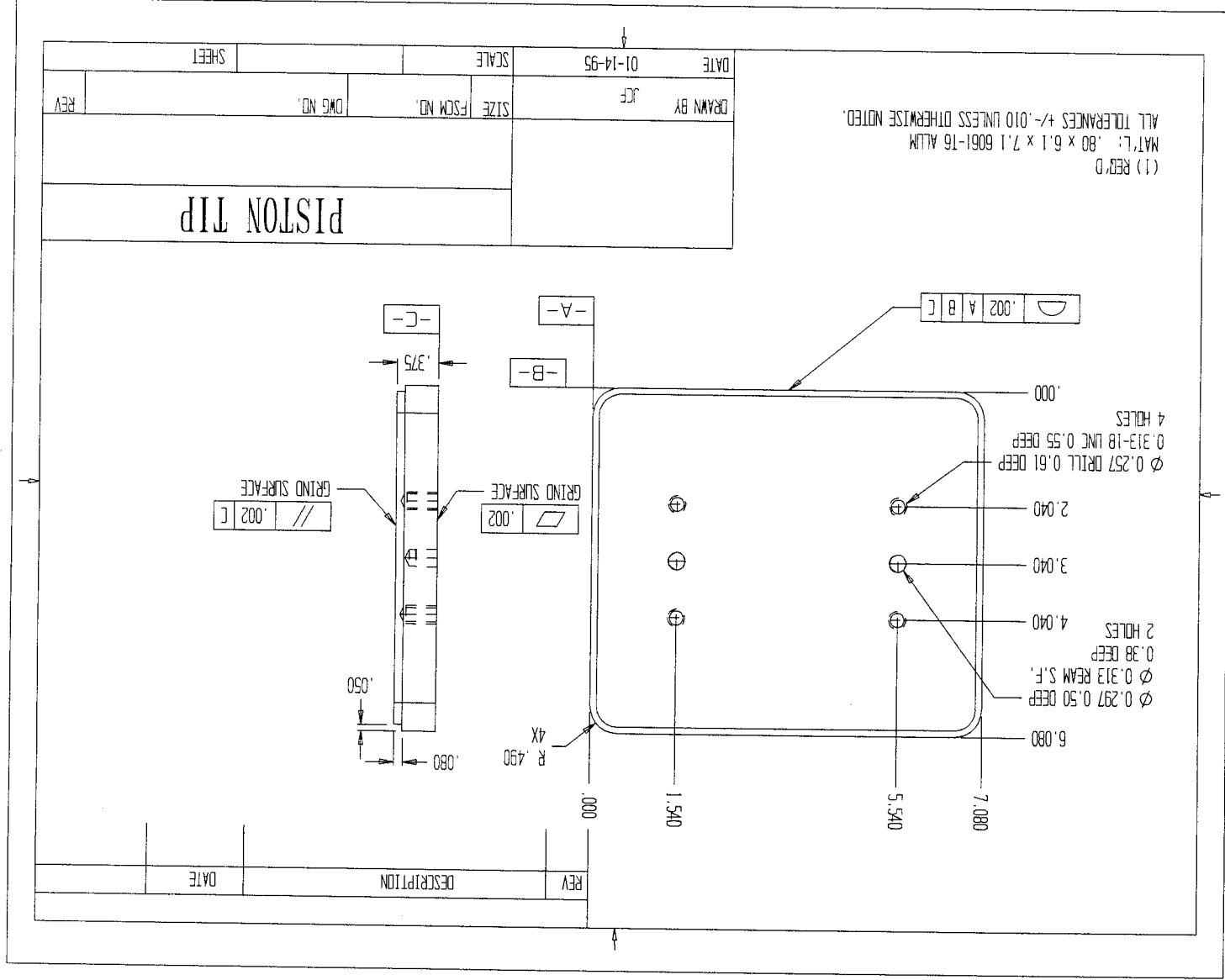
Figure A-3    Piston tip, Virginia Tech Fixture C.

144
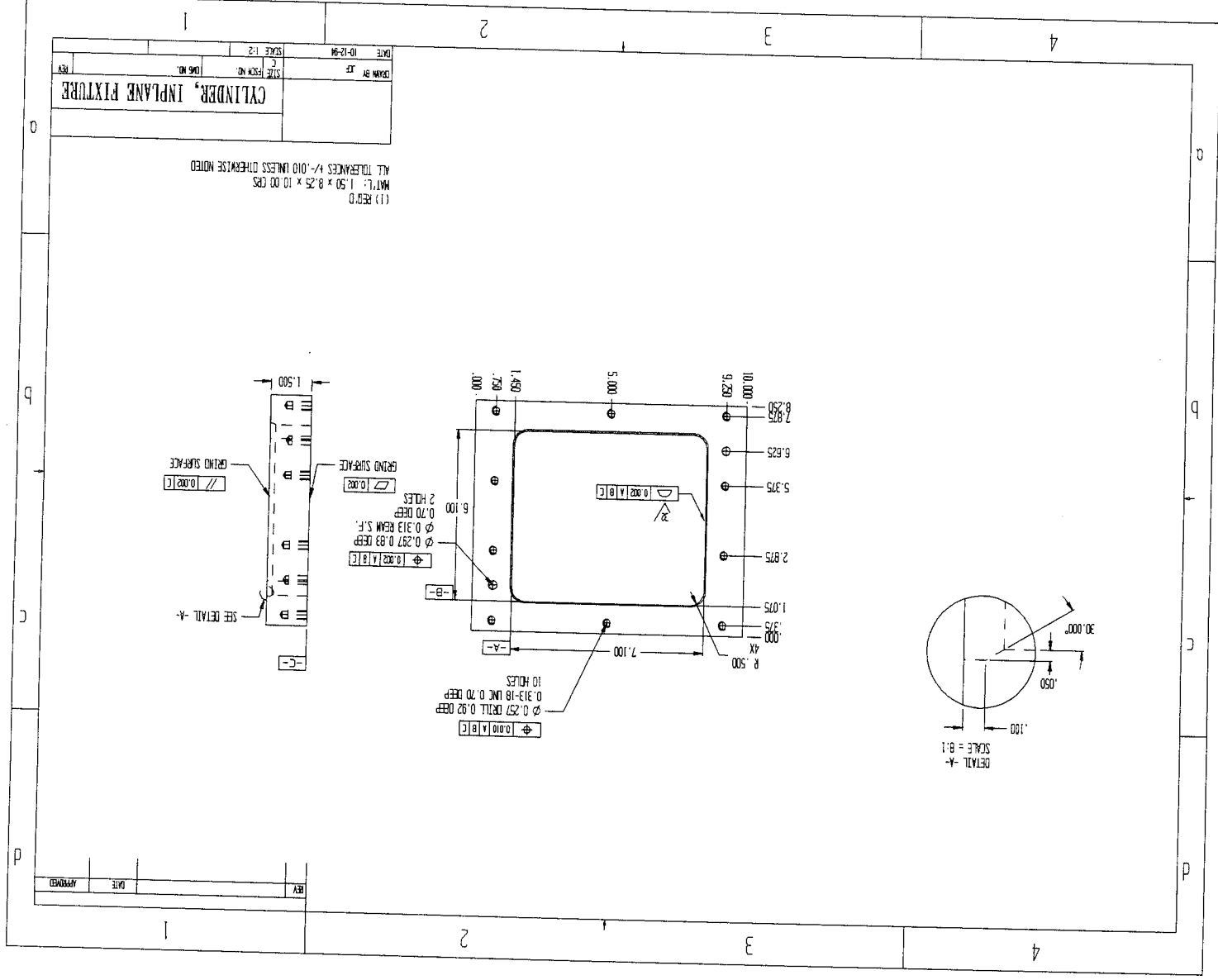
Figure A-4    Cylinder, Virginia Tech Fixture C.

145

Figure A-5    Base, Virginia Tech Fixture C.

Figure A-6    Guide post pin, Virginia Tech Fixture C.

147

| REV | DESCRIPTION | DATE | |
|-----|-------------|------|--|
| | | | |

Ø 1.250

.000
.700
1.750
2.750

Ø .500

1.000-12 UNF

(1) REQ'D
MAT'L:  1.25 DIA. X 2.75 L'G CRS
ALL TOLERANCES +/-.010 UNLESS OTHERWISE NOTED

## GUIDE POST PIN

| DRAWN BY | JCF | SIZE | FSCM NO. | | DWG NO. | | REV |
|----------|-----|------|----------|--|---------|--|-----|
| DATE | 10-12-94 | SCALE | 1:1 | | | SHEET | |
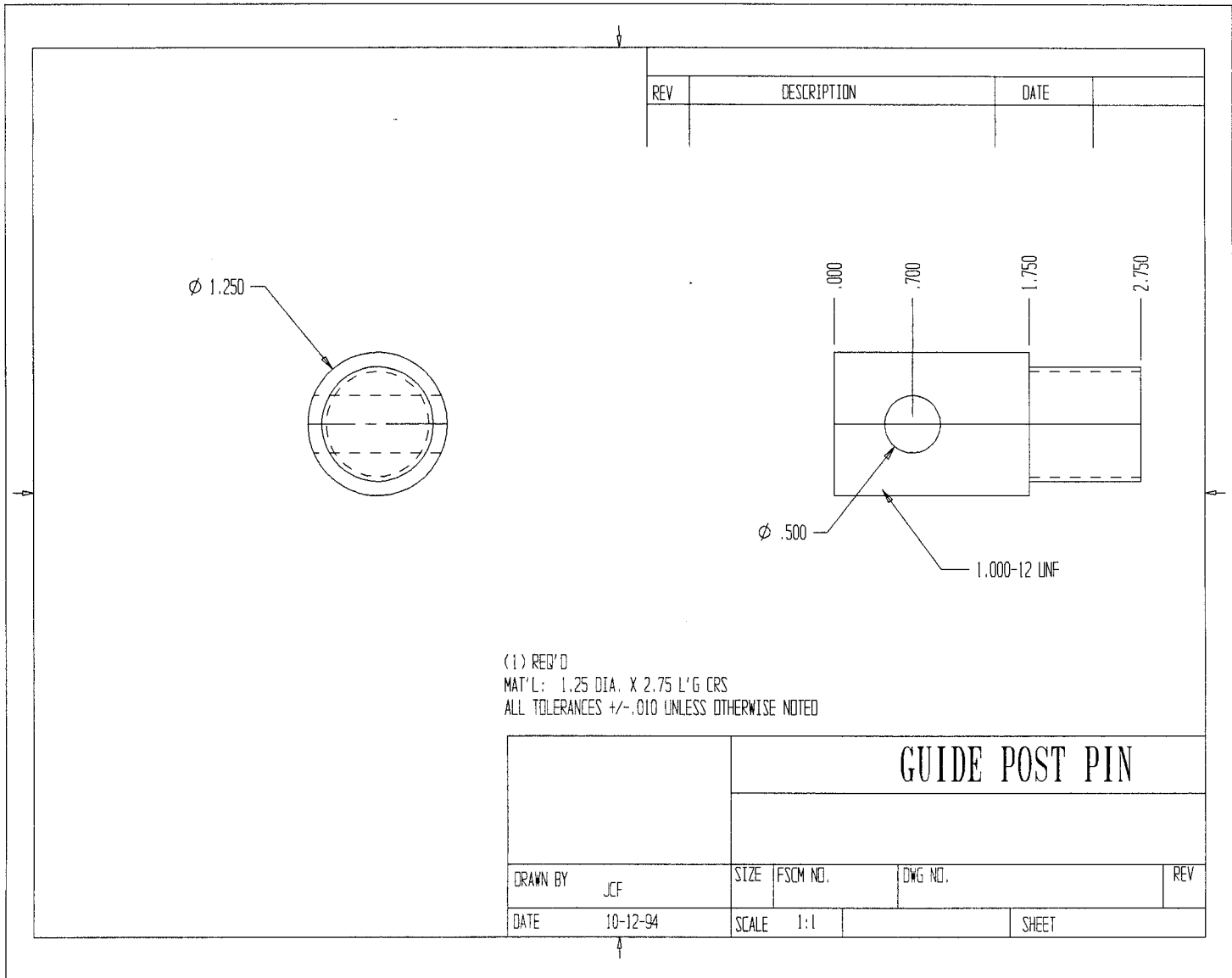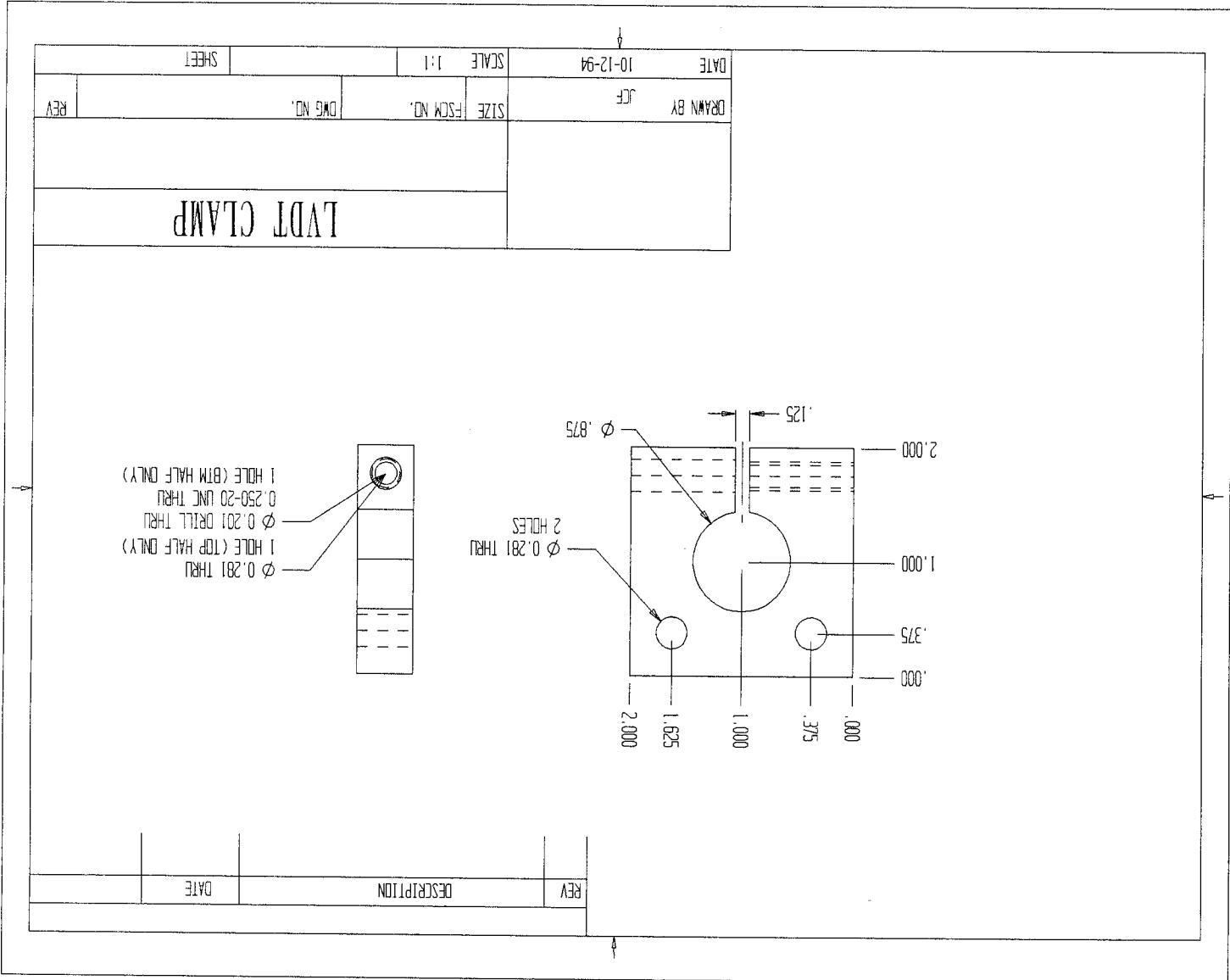
Figure A-7    LVDT clamp, Virginia Tech Fixture C.

The following text appears within the drawing:

LVDT CLAMP

| | | | | | REV |
|---|---|---|---|---|---|
| | | FSCM NO. | DWG NO. | | |
| DRAWN BY | JCF | | | | |
| DATE | 10-12-94 | SCALE | 1:1 | SHEET | |
| | | | SIZE | | |

| REV | DESCRIPTION | DATE |
|---|---|---|

Ø 0.281 THRU
1 HOLE (TOP HALF ONLY)

Ø 0.201 DRILL THRU
0.250-20 UNC THRU
1 HOLE (BTM HALF ONLY)

Ø .875

Ø 0.281 THRU
2 HOLES

.125

2.000
1.000
.375
.000

2.000
1.625
1.000
.375
.000

# Appendix B     **Blade-Stiffened Preform Flow Fixture Drawings**

Included are the prints used to manufacture the blade-stiffened preform flow fixture.

150

Figure B-1    Lower mold plate, blade-stiffened preform flow fixture.

Figure B-2    Upper left mold plate, blade-stiffened preform flow fixture.

151
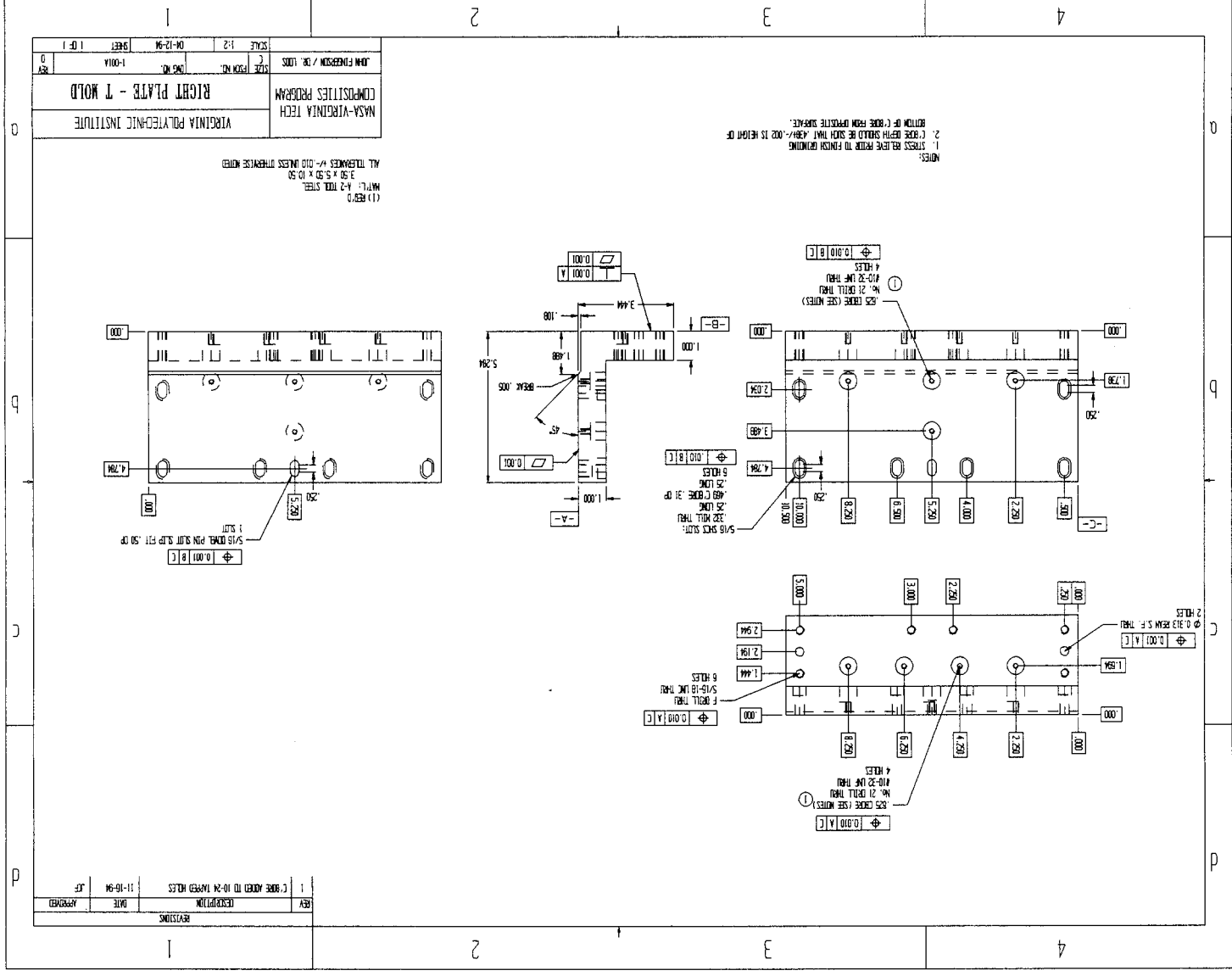
Figure B-3    Upper right mold plate, blade-stiffened preform flow fixture.

Figure B-4    Legs, blade-stiffened preform flow fixture.

Ø 0.344 THRU
Ø 0.531 CBORE
0.34 DEEP
1 HOLE

Ø 1.000

2.000

(4) REQ'D
MAT'L: 6061 ALUM
ALL TOLERANCES +/-.010 UNLESS OTHERWISE NOTED

| REV | DESCRIPTION | DATE | |
|-----|-------------|------|--|
|     |             |      |  |

| NASA-VIRGINIA TECH COMPOSITES PROGRAM | LEGS, T MOLD | |
|---|---|---|
| | JOHN FINGERSON / DR. LOOS | |
| DRAWN BY    JCF | SIZE | FSCM NO. | DWG NO.  1-004A | REV 0 |
| DATE    04-13-94 | SCALE    2:1 | | SHEET |

153

Figure B-5    Skin spacers, blade-stiffened preform flow fixture.

154

Figure B-6    Blade spacers, blade-stiffened preform flow fixture.

155

# Appendix C    Preperation of Preform Sample - Application of Polyurethane

**Materials Needed:**

Hexcel Uralite 3138 Part A

Hexcel Uralite 3138 Part B

Hexcel PartingKote 8302 Mold Preparation Agent

Hexcel BURP 8440 Air Displacement Spray

Two (2) 0.5" x 1.5" x 10.0" steel plates

Blade-stiffened wing panel flow fixture

Shim stock, .020" thick

**Preparation Method:**

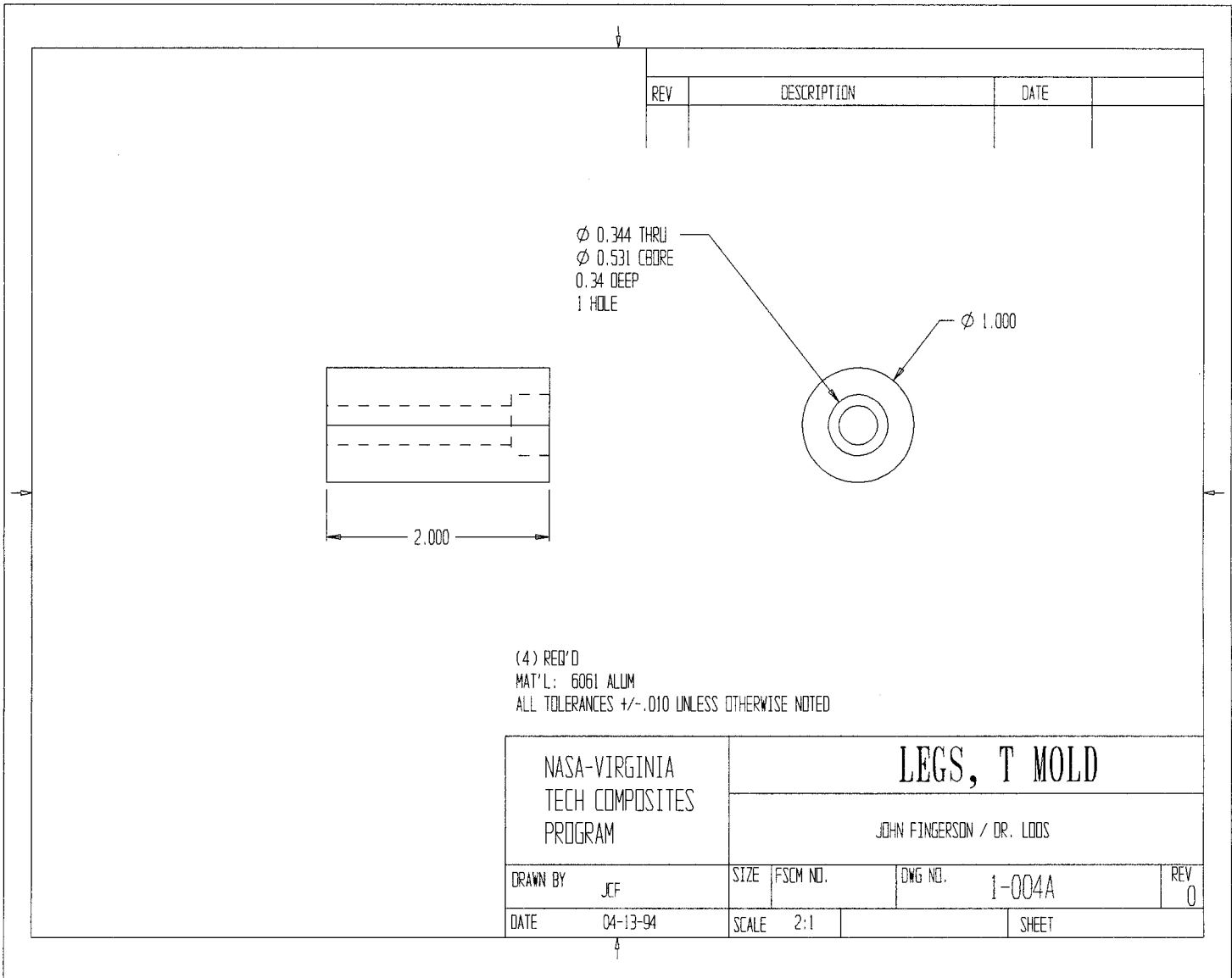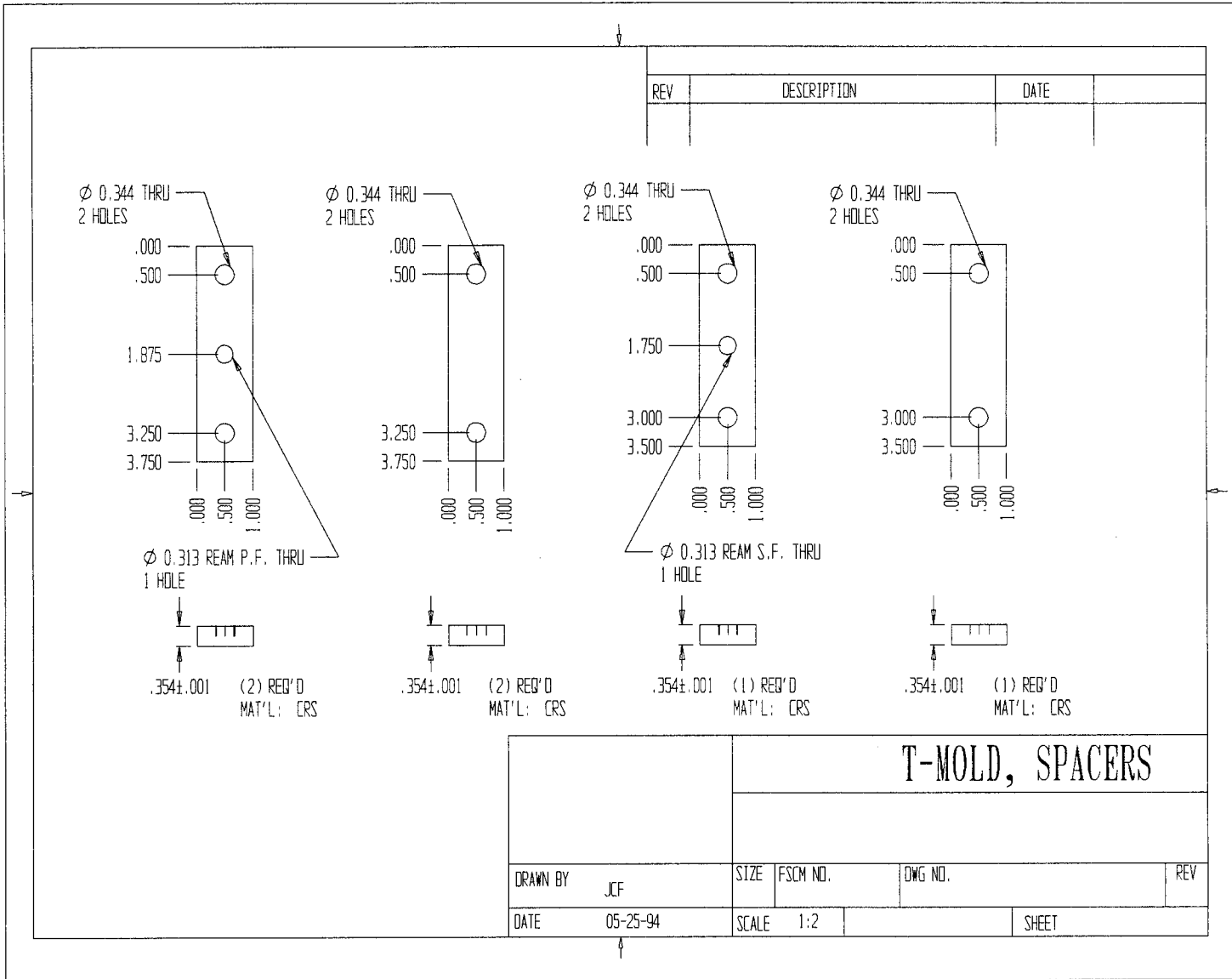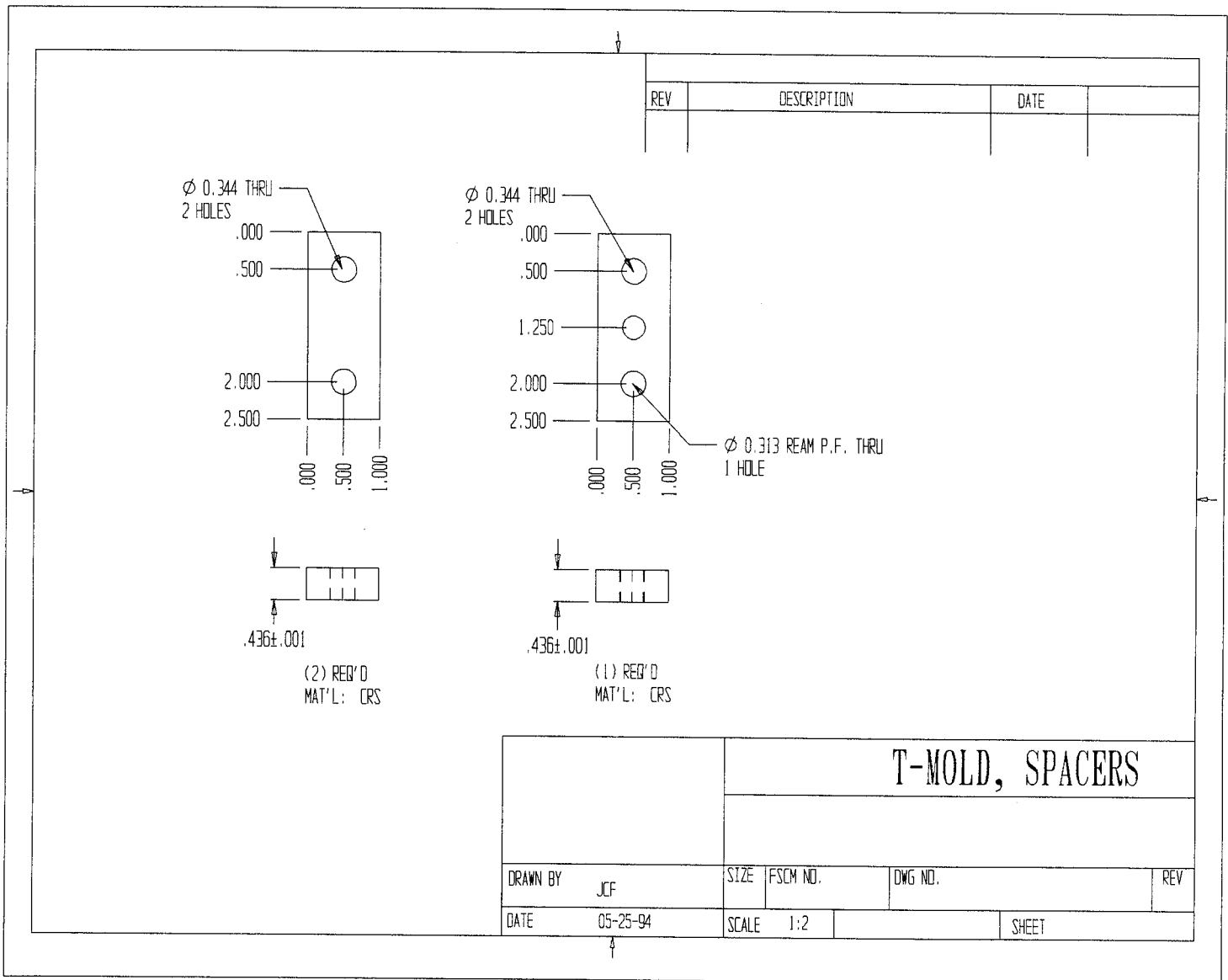1.  Premix a small quantity of PU according to mix ratio advised by manufacturer. Wait until the viscosity has risen sufficiently to prevent the PU from permeating the preform.

2.  Apply a light coat of PU to the edges of the preform where a closed boundary condition is desired. This creates a seal to prevent the next coat from permeating into the preform. Cure at 175°F for 2-3 hours.

3.  If PU is to be applied to T-shaped edge, follow step 4. If PU is to be applied to flat edge, follow step 5.

4.  T-shaped edge:

    4.1.  Apply a light film of Partingkote to the unassembled fixture and place the preform in the mold, approximately 3/16" away from the edge of the mold where PU is to be applied. The bolt holes near the edge of the mold should be covered by the preform.

    4.2.  Bolt the mold together using .020" shims under spacers. This ensures that the urethane will be under compression during the flow test. Do not install the spacers at the edge where the polyurethane is to be applied.

4.3. Place the mold in a flat dish which has been sprayed with PartingKote. The walls of the dish need to be at least 1/2" tall and the dish should be approximately 1" larger than the T-shaped face of the mold.

5. Flat edge:

5.1. Apply a light film of Partingkote to the two (2) 0.5" x 1.5" x 10.0" steel plates. Place the preform bewteen the steel plates, with a 3/16" gap between the edge of the preform and the edge of the steel plates.

5.2. Bolt the steel plates together using .020" shims and spacers from the flow fixture between the plates at each end near the bolts. This ensures that the urethane will be under compression during the flow test.

5.3. Place the preform/plates in a flat dish which has been sprayed with PartingKote. The walls of the dish need to be at least 1/2" tall and the dish should be approximately 1" larger than the outer edge of the steel plates.

6. Mix polyurethane parts A and B according to mix ratio recommended by manufacturer.

7. Cure in oven at 175°F for 2-3 hours.

# Appendix D   Example Patran session file

GO
1
1
2
SET, TOLERANC, .0000001
GRID, 1,,//
GRID, 2,,.0614426//
GRID, 3,,.0992378//
GRID, 4,,.1009483//
GRID, 5,,.1086017//
GRID, 6,,.1103122//
GRID, 7,,.1481074//
GRID, 8,,.2095500//
GRID, 9,,/.0089916/
GRID, 10,,.0614426/.0089916/
GRID, 11,,.0992378/.0089916/
GRID, 12,,.1009483/.0089916/
GRID, 13,,.1086017/.0089916/
GRID, 14,,.1103122/.0089916/
GRID, 15,,.1481074/.0089916/
GRID, 16,,.2095500/.0089916/
GRID, 17,,.0641858/.0117348/
GRID, 18,,.0992378/.0117348/
GRID, 19,,.1009483/.0117348/
GRID, 20,,.1086017/.0117348/
GRID, 21,,.1103122/.0117348/
GRID, 22,,.1453642/.0117348/
GRID, 23,,.0992378/.0647192/
GRID, 24,,.1009483/.0647192/
GRID, 25,,.1086017/.0647192/
GRID, 26,,.1103122/.0647192/
PATCH, 1, QUAD,,1/9/10/2
PATCH, 2, QUAD,,7/15/16/8
PATCH, 3, QUAD,,2/10/11/3
PATCH, 4, QUAD,,6/14/15/7
PATCH, 5, QUAD,,3/11/12/4
PATCH, 6, QUAD,,5/13/14/6
PATCH, 7, QUAD,,4/12/13/5
PATCH, 8, QUAD,,10/17/18/11

PATCH, 9, QUAD,,14/21/22/15
PATCH, 10, QUAD,,11/18/19/12
PATCH, 11, QUAD,,13/20/21/14
PATCH, 12, QUAD,,12/19/20/13
PATCH, 13, QUAD,,18/23/24/19
PATCH, 14, QUAD,,20/25/26/21
PATCH, 15, QUAD,,19/24/25/20
PATCH, 16T30, TRANSLATE, //.0716379, 1T15
PATCH, 31T45, TRANSLATE, //.0945983, 1T15
PATCH, 46T60, TRANSLATE, //.1022517, 1T15
PATCH, 61T75, TRANSLATE, //.1252121, 1T15
HPAT, 1T15, EXTRUDE, //.0716379, 1T15
HPAT, 16T30, EXTRUDE, //.0229604, 16T30
HPAT, 31T45, EXTRUDE, //.0076534, 31T45
HPAT, 46T60, EXTRUDE, //.0229604, 46T60
HPAT, 61T75, EXTRUDE, //.0716379, 61T75
GFEG, H1T4/H16T19/H46T49/H61T64,,5/6/4
GFEG, H5T7/H20T22/H50T52/H65T67,,2/6/4
GFEG, H8T9/H23T24/H53T54/H68T69,,5/2/4
GFEG, H10T12/H25T27/H55T57/H70T72,,2/2/4
GFEG, H13T15/H28T30/H58T60/H73T75,,2/6/4
GFEG, H31T34,,5/6/2
GFEG, H35T37,,2/6/2
GFEG, H38T39,,5/2/2
GFEG, H40T42,,2/2/2
GFEG, H43T45,,2/6/2
CFEG, H1T7/H16T22/H31T37/H46T52/H61T67, HEX,,1
CFEG, H8T9/H23T24/H38T39/H53T54/H68T69, HEX,,2
CFEG, H10T12/H25T27/H40T42/H55T57/H70T72, HEX,,3
CFEG, H13T15/H28T30/H43T45/H58T60/H73T75, HEX,,4
VIEW
1
34,-22,1
SET, ACTIVE, ELEMENT
SET, LABE, OFF
PLOT
PMAT, 1, TAN, 1.085E-09,0,0,4.582E-11,0,1.450E-09,0,0
PMAT, 2, TAN, 1.000E-09,0,0,4.000E-11,0,1.000E-09,0,0
PMAT, 3, TAN, 1.000E-09,0,0,4.000E-11,0,1.000E-09,0,0
PMAT, 4, TAN, 4.000E-11,0,0,1.000E-09,0,1.000E-09,0,0
END
2
2
N

2
1
Y
3
DFEG, H37, HEAT/E, 1.7785E-05,,F3
DFEG, H1T75, NSRC, 0
DFEG, H37, NSRC, D,, N2072/N2119/N2127/N2080/N2210/N2257/N2265/N2218
DFEG, H37, NSRC, 1.0,, N2072/N2119/N2127/N2080/N2210/N2257/N2265/N2218
DFEG, H1T75, TEMP/N, 0
DFEG, H37, TEMP/N, D,, N2072/N2119/N2127/N2080/N2210/N2257/N2265/N2218
DFEG, H2/17/32/47/62, TEMP/N, D,, F2
DFEG, H1/16/32/47/62, TEMP/N, D,, F1
DFEG, H2/17/32/47/62, TEMP/N, -1.0,, F2
DFEG, H1/16/32/47/62, TEMP/N, -1.0,, F1
END
7
2
6
3
2
2
7
5
1
1
1
3DMODEL11
N
9
6

| BIBLIOGRAPHIC DATA SHEET | 1. Report No. CCMS-95-10, VPI-E-95-04 | 2. | | 3. Recipient's Accession No. |
|---|---|---|---|---|
| 4. Title and Subtitle Verification of a Three-Dimensional Resin Transfer Molding Process Simulation Model | | | | 5. Report Date September 1995 |
| | | | | 6. |
| 7. Author(s) John C. Fingerson, Alfred C. Loos, and H. Benson Dexter | | | | 8. Performing Organization Rept. No. VPI-E-95-04, CCMS-95-10 |
| 9. Performing Organization Name and Address Virginia Polytechnic Institute and State University Department of Engineering Science and Mechanics Blacksburg, VA 24061-0219 | | | | 10. Project/Task/Work Unit No. |
| | | | | 11. Contract/Grant No. NAG-1-343 |
| 12. Sponsoring Organization Name and Address Mechanics of Materials Branch National Aeronautics and Space Administration Langley Research Center Hampton, VA 23681-0001 | | | | 13. Type of Report & Period Covered Interim Report -101 August 1993 - September 1995 |
| | | | | 14. |

15. Supplementary Notes
This report constitutes the Master's thesis in Engineering Mechanics of the first author.

16. Abstract
Experimental evidence was obtained to complete the verification of the parameters needed for input to a three-dimensional finite element model simulating the resin flow and cure through an orthotropic fabric preform. The material characterizations completed include resin kinetics and viscosity models, as well as preform permeability and compaction models.

The steady-state and advancing front permeability measurement methods are compared. The results indicate that both methods yield similar permeabilities for a plain weave, bi-axial fiberglass fabric. Also, a method to determine principal directions and permeabilities is discussed and results are shown for a multi-axial knot preform.

The flow of resin through a blade-stiffened preform was modeled and experiments were completed to verify the results. The predicted inlet pressure was approximately 65% of the measured value. A parametric study was performed to explain differences in measured and predicted flow front advancement and inlet pressures.

Furthermore, PR-500 epoxy resin/IM7 8HS carbon fabric flat panels were fabricated by the Resin Transfer Molding process. Tests were completed utilizing both perimeter injection and center-port injection as resin inlet boundary conditions. The mold was instrumented with FDEMS sensors, pressure transducers, and thermocouples to monitor the process conditions. Results include a comparison of predicted and measured inlet pressures and flow front position. For the perimeter injection case, the measured inlet pressure and flow front results compared well to the predicted results. The results of the center-port injection case showed that the predicted inlet pressure was approximately 50% of the measured inlet pressure. Also, measured flow front position data did not agree well with the predicted results. Possible reasons for error include fiber deformation at the resin inlet and a lag in FDEMS sensor wet-out due to low mold pressures.

17. Key Words and Document Analysis.     17a. Descriptors
resin transfer molding, permeability

17b. Identifiers/Open-Ended Terms

17c. COSATI Field/Group

| 18. Availability Statement | 19. Security Class (This Report) UNCLASSIFIED | 21. No. of Pages 174 |
|---|---|---|
| | 20. Security Class (This Page) UNCLASSIFIED | 22. Price |

The Center for Composite Materials and Structures (CCMS) is a supporting and coordinating organization for composite materials research and educational programs at Virginia Tech. The Center is designed to encourage and promote continued advances in the science and technology of composite materials and structures and to enhance the transfer and utilization of these new developments in industries and government organizations in Virginia, the nation, and the world.

The CCMS functions through an annually elected Administrative Board and a Director who is elected for a three-year term. Members of the Center include 46 faculty members in 12 academic departments in the College of Engineering and College of Arts and Sciences; 15 associate members; four technical staff members; approximately 100 graduate students; four Industrial Affiliates representing a variety of composite materials interests at the national level; and government and industrial Research Sponsors currently supporting more than 50 research grants and contracts exceeding $4 million annually on composite materials and structures.

Specific objectives of the CCMS under this program include:
* providing a formal, interdisciplinary partnership between faculty, technical staff, and students who have active and complementary interests in composite materials and structures;
* providing leadership and coordination to enhance development and promote general success of research and educational activities in composite materials by shared responsibility, cooperative action, interdisciplinary support, and unified service;
* providing a means for the Virginia Tech composite materials and structures program to interact with university, state, national and international agencies, organizations, and industries; and
* promoting continued national and international recognition of the excellence in educational and research programs in composite materials and structures at Virginia Tech.

The CCMS has developed and operates a Fabrication and Instrumentation Laboratory to provide composite material fabrication capabilities. This facility is also available for conducting basic and applied research in composite processing and manufacturing. The Laboratory supports the educational and research programs of its membership. It also provides technical assistance to various research programs.

The educational mission of the CCMS is conducted by its members, in concert with the academic departments, at the undergraduate and graduate levels. This mission prepares students for careers in composites research, development, and application. More than 350 graduates of the Virginia Tech composites program have joined industries, government agencies, and universities. These individuals have provided significant advances to the science and technology of composite materials, and have attained positions of national leadership in the field.

The comprehensive research programs of the CCMS members cover the full range of composites science and technology. This includes the development and fabrication of new, improved constituents and material systems to the design and analysis of optimized composite components and structures. The most recent composites research accomplishments are reported in CCMS member's authored refereed papers and technical reports.

In addition to the CCMS Report Series, the CCMS administers:
* a vigorous Seminar Series featuring prominent speakers from leading laboratories and companies around the world, as well as CCMS students and faculty members;
* a sesquiannual Technical Review with the Center for Adhesive and Sealant Science; and
* the CCMS Bulletin, a quarterly newsletter of current events, notices, research opportunity announcements, and technical interest articles.

## MEMBERS OF THE CENTER

**Aerospace and Ocean Engineering**

Raphael T. Haftka
Eric R. Johnson
Rakesh K. Kapania

**Chemical Engineering**

Donald G. Baird
Richey M. Davis
Garth L. Wilkes

**Chemistry**

John G. Dillard
James E. McGrath
Thomas C. Ward
James P. Wightman

**Civil Engineering**

Richard M. Barker
W. Samuel Easterling
Richard E. Weyers

**Computer Science**

Layne T. Watson

**Electrical Engineering**

Ioannis M. Besieris
Richard O. Claus
Douglas K. Lindner

**Engineering Fundamentals**

Deidre A. Hirschfeld

**Engineering Science and Mechanics**

David A. Dillard
Norman E. Dowling

**Engineering Science and Mechanics (continued)**

Daniel Frederick
O. Hayden Griffin, Jr.
Zafer Gürdal
Robert A. Heller
Edmund G. Henneke, II
Michael W. Hyer
Robert M. Jones
Ronald D. Kriz
Liviu Librescu
Alfred C. Loos
Don H. Morris
Ali H. Nayfeh
Kenneth L. Reifsnider
C. W. Smith
Surot Thangjitham

**Industrial and Systems Engineering**

Joel A. Nachlas

**Materials Science & Engineering**

Seshu B. Desu
D. P. H. Hasselman
Stephen L. Kampe
Ronald G. Kander
Brian J. Love

**Mathematics**

Werner E. Kohler

**Mechanical Engineering**

Charles J. Hurst
Charles E. Knight
Craig A. Rogers
Curtis H. Stern